AN ABSTRACT OF THE THESIS OF

RICHARD HENRY BOSSI for the degree of DOCTOR OF PHILOSOPHY

in Nuclear Engineering (Major Department) presented on December 3, 1976 (Date of Examination)

Title: HIGH SPEED MOTION NEUTRON RADIOGRAPHY

Abstract approved: Redacted for Privacy

Alan H. Robinson

A system to perform neutron radiographic analysis of dynamic events taking place over the order of several milliseconds has been developed at Oregon State University. The design consists of a TRIGA reactor capable of pulsing to 3000 MW peak power, a neutron beam collimator with an L/D of about 30:1, a lithium fluoride-zinc sulphide (LiF-ZnS) neutron scintillator screen, an image intensifier and a 16 mm high speed movie camera. The TRIGA reactor pulse and beam port collimator combine to yield a peak thermal neutron flux of about 4.2×10^{11} n/cm^2-sec at the object with a pulse width (FWHM) of 9 milliseconds. During this pulse duration sequential neutron radiographs are taken by the imaging system which detail any movement occurring in the object.

The imaging system operates by converting the neutron signal to light, amplifying the light signal and recording the information on 16 mm Rapid Arts Recording film. LiF-ZnS neutron scintillator screens of 2/1 weight ratio of ZnS to LiF and 0.13 mm thickness constructed at OSU with sodium silicate binder are found to be very successful.

The construction of the scintillators plus both an analytical model and experimental study of their performance is described. These screens have good light yield, good resolution and sufficiently rapid light decay characteristics to allow individual framing at over 5000 frames/second. The image intensifier is a two stage, 40 mm diameter tube. An S-20 photocathode and a P-11 output phosphor are employed in the intensifier for their rapid decay characteristics and spectral response. The tube has a fiber optics input faceplate onto which the scintillator screen is pressure held for radiography. Actual imaging through the intensifier is superior to the conventional scintillator screen in contact with film method, apparently due to the non acceptance of wide angle light by the fine fiber optics. The high speed movie camera focuses on the intensifier output screen.

Modulation transfer function analysis of the system indicates that the scintillator screen and the collimator L/D ratio are the two weakest areas of image quality in the system. The intensifier and high speed camera exhibit much better quality. Image quality can also be subject to statistical limitations due to the very short exposure times (about 80 μsec at 5000 frames/second) per frame in the imaging system. Experimental studies indicate that the image quality becomes statistically limited for general detail below about 10^7 n/cm^2 fluence incident on the object. Subject to the object thickness and level of detail desired, the OSU system may be operated at up to 10,000 frames/second without experiencing this problem. For fine detail though it is necessary to enhance the object contrast by appropriate doping with a high contrast material such as gadolinium.

This high speed motion neutron radiography technique may be applied to the interrogation of rapid dynamic events that have imaging characteristics suitable for neutron radiography inspection. High speed motion neutron radiographs have been taken of the ballistic cycle of both live and blank 7.62 mm munition rounds and of two phase flow as represented by air bubbles passing through water.

High Speed Motion Neutron Radiography

by

Richard Henry Bossi

A THESIS

submitted to

Oregon State University

in partial fulfillment of
the requirements for the
degree of

Doctor of Philosophy

Completed December 3, 1976

Commencement June 1977

APPROVED:

Redacted for Privacy

Professor of Nuclear Engineering

Redacted for Privacy

Head of Department of Nuclear Engineering

Redacted for Privacy

Dean of Graduate School

Date thesis is presented December 3, 1976

ACKNOWLEDGEMENT

With the completion of this thesis and my degree I wish to acknowlege a few of the many who helped to make it possible. My thanks to Frankford Arsenal for their support in part of the work on "High Speed Motion Neutron Radiography". Also my thanks and appreciation to Dr. C.H. Wang, Director of the Oregon State University Radiation Center and Chairman of the Department of Nuclear Engineering, for his support of the work and to his staff, in particular Terry Anderson and Bill Carpenter of Reactor Operations, for their willing assistance.

To the members of my graduate committee I would like to express special thanks. Foremost, to Dr. Alan Robinson, as my major professor, I am most appreciative of his direction of my thesis investigation and guidance of my degree programs. To Dr. Bernard Spinrad, from whom I received the major part of my nuclear engineering instruction, I am very grateful for the opportunity to have studied under him. Similarly to Dr. William McMullen, I am appreciative of his instruction of the majority of my metallurgical engineering studies. Special thanks go to Dr. John Barton for his friendship, assistance and support of my career in neutron radiography and nondestructive testing.

Among the many others who have helped to shape my career I wish to especially thank my parents and relatives for their support, moral and financial, of my numerous years of education. And finally, to Peg; thanks so very much for waiting, sweatheart.

TABLE OF CONTENTS

LIST OF TABLES

LIST OF FIGURES

HIGH SPEED MOTION NEUTRON RADIOGRAPHY

I. INTRODUCTION

1.1 Historical Background

Neutron radiography has been experimentally performed since the early work of Kallman and Kuhn in 1935 (1,2). Thewlis (3) renewed this work in the 1950's; however, significant application and development did not occur until the 1960's. Berger (4) suggests the reason for the thirty year delay between discovery and practical application of neutron radiography lay in the lack of suitable neutron sources and the more pressing problems of neutron physics. The last ten years have seen widespread growth in the use of neutron radiography. A number of publications on the general principles and applications have been written (4-9), plus an ever growing volume of material on the special techniques for neutron radiography. Today neutron radiography is routinely used for nondestructive examination of suitable objects with appropriate standard practises and certification under the American Society for Testing and Materials and the American Society for Nondestructive Testing.

1.2 General Neutron Radiography Technique

In its simplest form, neutron radiography consists of passing a collimated beam of thermal neutrons through an object and imaging the spatially modulated transmitted beam by a suitable neutron imaging technique. Figure 1-1 presents this radiography system. The

Figure 1-1

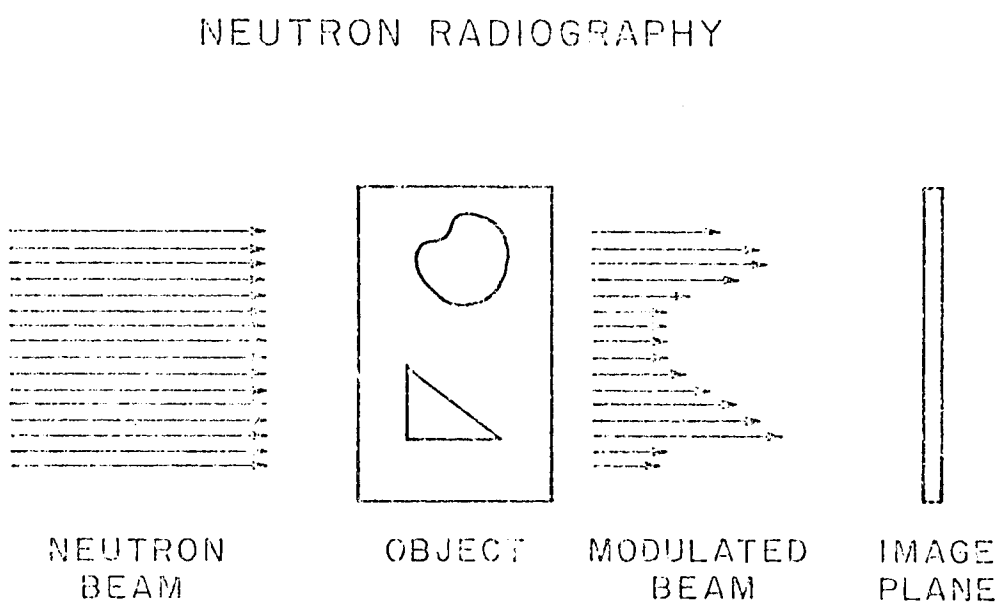
NEUTRON RADIOGRAPHY
NEUTRON BEAM
OBJECT
MODULATED BEAM
IMAGE PLANE

similarity of neutron radiography to x radiography is readily apparent. The essential difference between these two methods for inspection of an object's internal features lies in the attenuation coefficients of materials to the respective type of penetrating radiation. This distinction is presented in figure 1-2. Whereas x-ray attenuation is due to electron cloud interaction and therefore increases with increasing atomic number, neutron attenuation may vary significantly with atomic number and may even do so between isotopes of the same element. For inspection puposes, this difference has made neutron and x-ray radiography complementary techniques.

In addition to the differences in attenuation between neutrons and x rays, the imaging technique also varies; presently no neutron imaging film exists. Instead, converters are used to change the neutron radiation into ionizing radiation or light which will expose radiographic or photographic film. High neutron cross section thin foils such as gadolinium may be placed in a cassette with x-ray film and then in the path of the neutron beam (figure 1-3A). Neutrons absorbed in the foil generate beta radiation (internal conversion electrons in the gadolinium case) which directly exposes the film. This technique using very thin gadolinium foil or a vapor deposited gadolinium layer and fine grain film presently provides the highest quality neutron radiographs. Alternately, foils of materials that become activated under neutron bombardment such as indium, dysprosium or europium may be used. Once the foil has become suitably activated, it is removed from the beam and placed in contact with a film in a light tight cassette. The radioactivity of the foil exposes the film,

Figure 1-2

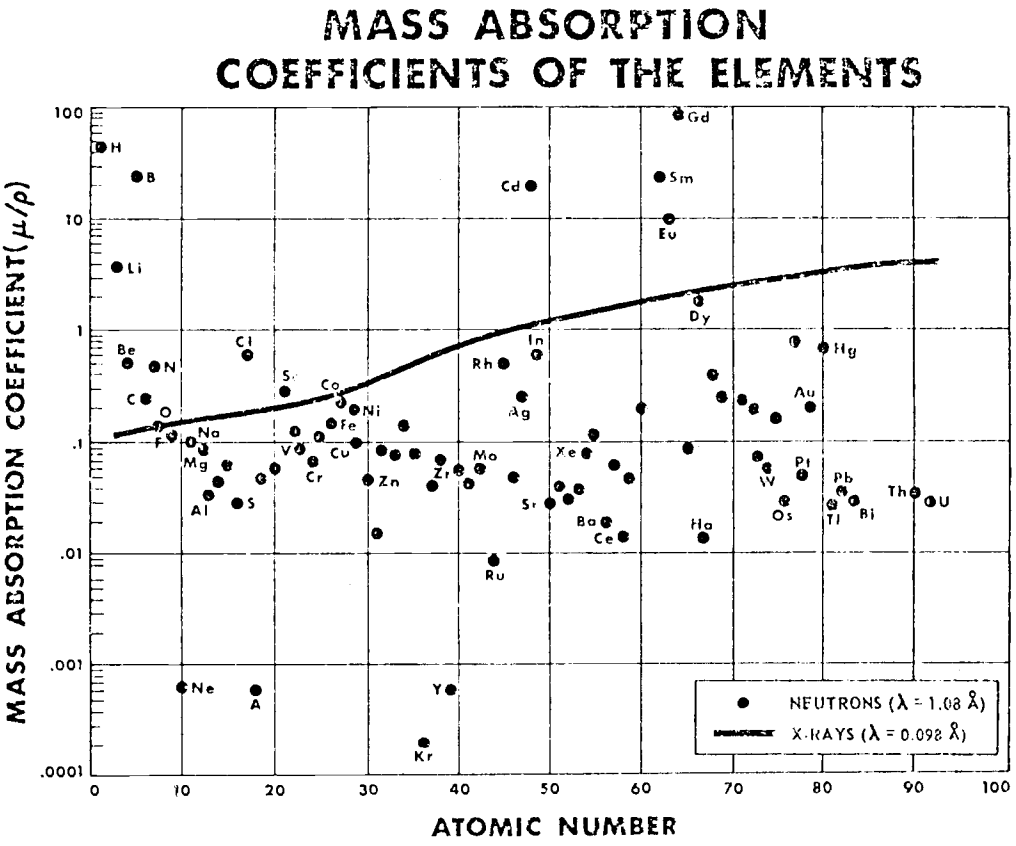
MASS ABSORPTION
COEFFICIENTS OF THE ELEMENTS
MASS ABSORPTION COEFFICIENT(μ/ρ)
ATOMIC NUMBER
100
10
1
.1
.01
.001
.0001
0
10
20
30
40
50
60
70
80
90
100
H
B
Li
Be
N
C
O
F
Na
Mg
Al
S
Cl
A
Ne
K
Ca
Sc
Ti
V
Cr
Mn
Fe
Co
Ni
Cu
Zn
Ga
Ge
As
Se
Br
Kr
Rb
Sr
Y
Zr
Nb
Mo
Ru
Rh
Pd
Ag
Cd
In
Sn
Sb
Te
I
Xe
Cs
Ba
La
Ce
Pr
Nd
Sm
Eu
Gd
Tb
Dy
Ho
Er
Tm
Yb
Lu
Hf
Ta
W
Re
Os
Ir
Pt
Au
Hg
Tl
Pb
Bi
Th
U
NEUTRONS (λ = 1.08 Å)
X-RAYS (λ = 0.098 Å)

Figure 1-3

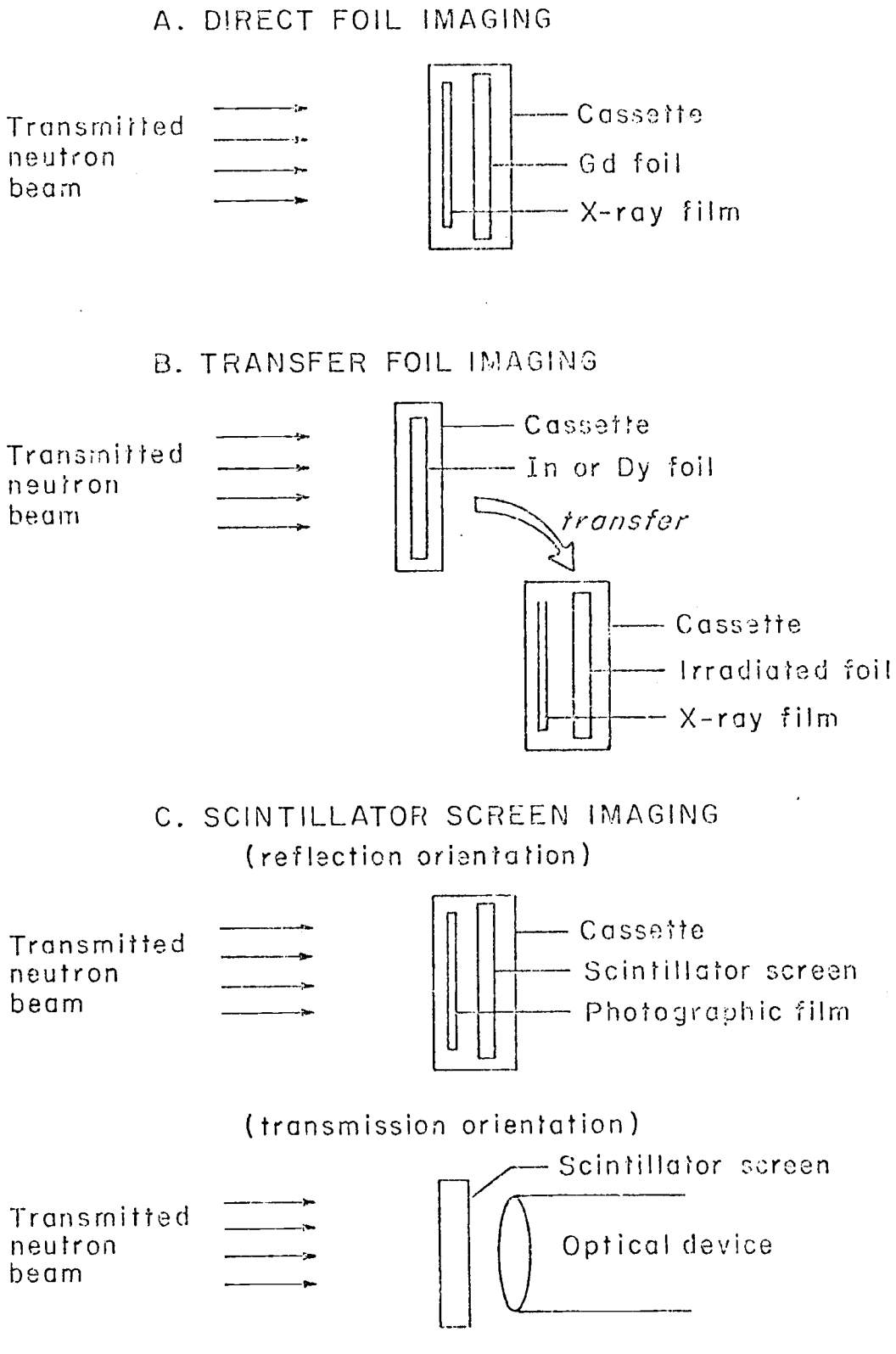
A. DIRECT FOIL IMAGING
Transmitted neutron beam
Cassette
Gd foil
X-ray film
B. TRANSFER FOIL IMAGING
Transmitted neutron beam
Cassette
In or Dy foil
transfer
Cassette
Irradiated foil
X-ray film
C. SCINTILLATOR SCREEN IMAGING
(reflection orientation)
Transmitted neutron beam
Cassette
Scintillator screen
Photographic film
(transmission orientation)
Transmitted neutron beam
Scintillator screen
Optical device

transfering the imaged information (figure 1-3B). This technique allows radiographs to be taken independently of any high levels of undesirable radiation from the object or neutron source that might fog the x-ray film if it were in the path of the beam during exposure. Scintillator screens may also be employed for neutron radiography. These screens contain a high neutron absorption cross section material such as Li-7, B-10 or Gd plus a scintillation material. Following neutron absorption, the scintillation material, such as zinc-sulphide, is stimulated by ionizing radiation from the neutron interaction and light is emitted. The light may be used to expose light sensitive film or input into other optical devices (figure 1-3C). This last technique is the most rapid method for taking neutron radiographs; that is, it requires the fewest number of input neutrons in order to generate a suitable radiograph.

1.3 Review of Neutron Radiography Applications and Special Techniques

Very extensive research and development have been performed with neutron radiography systems and techniques for stationary objects. These are not reviewed here in detail but numerous citations to the appropriate literature may be found in the bibliography. The predominate areas of neutron radiography application have been in the inspection of hydrogenous material and heavy elements. Ordnance devices, consisting of a hydrocarbon encased in a metal container, are relatively insensitive to x-ray interrogation requiring neutron radiography inspection (10). Nuclear fuel of uranium or plutonium cannot be adequately inspected with x rays for other than gross

surface flaws behind the cladding due to the limited penetration of the beam. Neutron radiography however provides total inspection of fuel elements with sensitivity to the enrichment, segregation and internal flaws both before and after irradiation (11-15). Neutron radiography has also been applied in specific instances to the detection of hydriding in titanium and zirconium (16,14). Although progress has not been rapid, medicine and biology applications do exist for neutron radiography for which some successful work has been accomplished (17-20). Supplementing these applications, there has been a continual development of special techniques; such as the use of very low energy, epithermal or fast neutrons in neutron radiography to gain increased contrast sensitivity or penetration in objects (21-26). Nonreactor sources have been employed for economics or transportability (27-30). And new imaging methods have also been developed such as electronic techniques and track-etch (31-33).

The application of neutron radiography to dynamic events has been minimal. Berger (34) developed a real time imaging system for neutron radiography which employed a scintillator-image intensifier detection device and a television viewing screen. This system provided immediate observation of the object for stationary inspection and also the capability to observe motion. Dynamic sensitivity allowed objects moving as fast a 5 m/second to be followed. The thermal expansion of irradiated reactor fuel in cladding could be observed with the system. For very rapid dynamic events requiring neutron radiography, flash techniques have been used to stop the event at one stage of movement. Robinson and Porter (35) used the pulsing mode of the TRIGA reactor

at Oregon State University to demonstrate this technique on a swinging bottle. Mullender and Hart (36) have used the VIPER reactor to perform the same work on the feasibility of observing two phase flow. Aseltine and Strich (37) used a fast pulse reactor having pulses of 50 μsec full width at half maximum to radiograph objects moving at speeds up to 76 m/sec. At speeds of 40 m/sec however the 50 μsec exposure showed appreciable blur. Using this burst reactor and activation transfer detecting foils of varying resonance absorption energies they have suggested a pseudo-motion picture system whereby the time of flight difference for the different energy neutrons would expose the detectors in sequential time intervals. The time delays would be in the range of ten to several hundred μseconds.

It is possible though to advance a system that will neutron radiograph rapidly occuring dynamic events, on the order of milliseconds, yielding a motion picture result. Originally initiated by A.H. Robinson and C.R. Porter and later completed by J.P. Barton, R.H. Bossi and A.H. Robinson (38,39) this technique is called "High Speed Motion Neutron Radiography". Unlike the flash techniques, the high speed motion system uses a broad enough neutron pulse to allow many frames to be imaged rather than a single exposure during the reactor transient. Similar to the television system, a scintillator screen and image intensifier are used but the final image record is on motion picture film. Based on this work at Oregon State University, development of similar systems have been investigated at Sandia Laboratories and also by Aseltine at the U.S. Army Ballistic Research Laboratory.

Application of high speed motion neutron radiography is, of course, specialized for objects that cannot be inspected in any other reasonable manner. The ballistic cycle of an ordnance device is well suited in that it consists of a hydrocarbon propellant inside a metal container which upon firing burns over a several millisecond period. No other technique now known can produce such a radiographic interrogation of the firing event. This technology may also be applied to some cases of two phase flow. A gaseous phase moving through a liquid can be imaged as a function of time provided a good contrast to neutrons is present. Water or other hydrogenous materials might be studied inside solid piping or complex valving during a particularly rapid phase change. Similarly, nuclear fuel undergoing rapid transient tests possibly could be radiographed to study the shifting of fuel location as melting takes place.

1.4 Scope of this Study

The scope of this study covers the design, assembly and evaluation of a system for obtaining high speed motion neutron radiographs approaching 10,000 frames/second. The system design considers the capability of standard neutron radiographic procedure and the adjustments necessary for the high speed work. The appropriate assembly of suitably chosen components to achieve the desired results is detailed. The operation of the TRIGA reactor is reviewed as the neutron source is central to the system design. Scintillation screens are analyzed and optimized for operation in high speed motion work. Both analytical and experimental results on lithium fluoride-zinc

sulphide neutron scintillator screen performance are given. A quantitative evaluation of the performance of the high speed motion system in terms of image quality is provided by modulation transfer function (MTF) analysis. The modulation transfer functions of the total system as well as the individual components are presented. The technique for obtaining the MTF is also described. The effects of statistical limitations of the neutron signal on the radiographic image are considered and experimentally evaluated. Finally, high speed motion neutron radiographs of the ballistic cycle of both blank and live 7.62 mm munition rounds and of two phase flow are included.

II. SYSTEM DESIGN

2.1 Radiography Requirements

Standard high quality neutron radiography using gadolinium foil and fine grain film requires a neutron fluence of approximately 10^9 neutrons/cm^2 for suitable exposure. Using a high flux reactor having a thermal neutron flux of 10^{13} n/cm^2-sec, fine collimation with an L/D ratio of 300:1 (L/D is the length to diameter ratio which is a measure of beam divergence) and an object transmission of 10%, the exposure time is about 20 minutes (1200 seconds) for the foil film combination. This is quite acceptable for stationary radiography; however, for dynamic events the exposure time required for a 10,000 frame/second movie is approximately 40 microseconds (4×10^{-5}) or a factor of 3×10^7 shorter. To reconcile this problem and maintain sufficient neutrons for a suitable radiographic image, a high speed motion neutron radiographic system is designed which incorporates a pulsing reactor neutron source, a beam collimator with limited loss of neutron intensity and a scintillator screen imaging system. The light from the scintillator screen is input to an image intensifier to boost the light intensity, and the information is recorded by a high speed photographic camera focused on the intensifier output. This system is diagrammed in figure 2-1. Each component must be selected to perform its function without overly degrading the ultimate image and likewise not forcing excessive reliability on the other components for maintaining the high speed capability.

Figure 2-1

HIGH SPEED MOTION NEUTRON RADIOGRAPHY SYSTEM

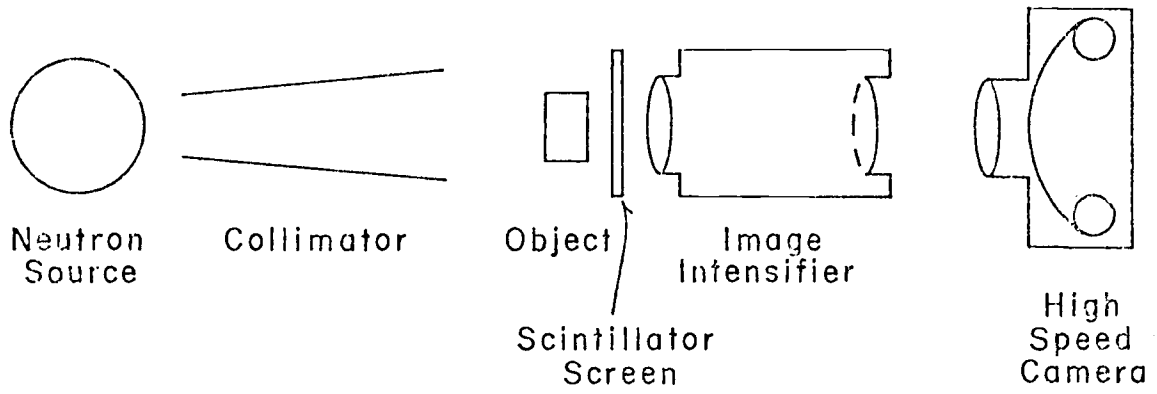

2.2 Neutron Source

The neutron source necessarily should be of the greatest intensity available. Typical research reactors operate at a peak steady state flux level of 10^{12} to 10^{13} n/cm^2-sec. While this is acceptable for stationary radiography or very slow dynamic movements (perhaps frame rates on the order of 3/second), a much higher flux is desired for very high speed results. A few high flux reactors, such as the ATR at Idaho Falls and the HFIR at Oak Ridge, have peak fluxes on the order of 10^{15} n/cm^2-sec. These reactors would allow some limited high speed work to be performed. Even higher fluxes may be attained however by the use of a pulsing reactor. In this instance, the reactor undergoes a rapid positive reactivity insertion driving it to very high power levels lasting only a short time after which the chain reaction is shut down automatically. Examples are the TRIGA, Pulstar and TREAT reactors (40-42). The peak flux and pulse duration are design parameters of the reactor type. While some reactors have extremely short pulse widths (on the order of tens or hundreds of microseconds, essentially bursts) for high speed motion neutron radiography the duration of the pulse must be sufficient to cover the actual event time. The intensity of the neutron flux of course is not constant over a pulse so that frame to frame images experience a variation of exposure according to the pulse shape.

At Oregon State University the 1 MW steady state TRIGA Mark II reactor is licensed for a peak pulsing power capability of 4000 MW. The reactor core configuration, with optimal location of standard

fuel elements provides an actual maximum pulsing power of approximately 3000 MW. This 3000 MW pulse has a half width of approximately 9 milliseconds and a peak core thermal flux on the order of 8×10^{16} n/cm^2-sec. The 9 millisecond pulse width allows events of short duration to be radiographed in a beam having a moderate intensity change over the cycle. The next chapter discusses in greater detail the pulsing operation of the Oregon State TRIGA Reactor (OSTR).

2.3 Collimation

Thermal neutrons emitted from the source must be collimated for neutron radiography. The collimation refines the diverging neutrons and determines the geometric unsharpness effects of the radiography facility. Collimators may be of several types: for example, solar slit, divergent and convergent-divergent (43-45). The essential defining factor for the collimator is the length to diameter ratio (L/D) which is a measure of the beam diverging angle at the collimator face. The diameter is the smallest opening along the entire length. Allowing for problems with neutron scattering by the collimator walls, the L/D ratio provides a measure of the geometric unsharpness that may be expected from the neutron radiography facility by

$$U_g = \frac{d}{(L/D)} \qquad (2\text{-}1)$$

where U_g is the geometric unsharpness and d is separation between the object and the imaging plane. Additionally, the L/D ratio may be applied to calculate the anticipated flux at the object position. The neutron flux at the end of the collimator (ϕ) is given by

$$\phi = \frac{\phi_o}{4\pi (L/D)^2} \qquad (2\text{-}2)$$

where ϕ_o is the neutron flux at the collimator input. As the L/D ratio is increased to improve the resolution capability of the beam, the neutron flux at the object will be decreased, requiring longer exposure times.

A collimator L/D of approximately 30:1 is employed for the high speed work at Oregon State University. This provides acceptable resolution with only a factor of about 10^4 decrease in flux at the object position from the initial source strength. The high speed facility collimator is located on the tangential beam port of the OSTR. The collimator design is shown in figure 2-2. The input end of the collimator is located in a radial beam tube such that a graphite collar inserted into the radial port acts as a source block. The hole in the graphite source block and lead plug insert are designed for experiments on the radial port. Selection of the tangential beam port for neutron radiography is intended to increase the neutron to gamma ratio of the beam as opposed to the radial ports which look directly at the reactor core. Provided the source block is appropriate the flux in the tangential port should not be significantly reduced. Studies by others (46) indicate that the source block design can be optimized for a greater beam strength.

The collimator itself is somewhat of a convergent-divergent design with variable aperture selection. Normally it is operated the "wide open" position for the greatest flux at the object. The smallest rectangular aperture in this instance measures 11.4 by

Figure 2-2

BEAM PORT #3 COLLIMATOR

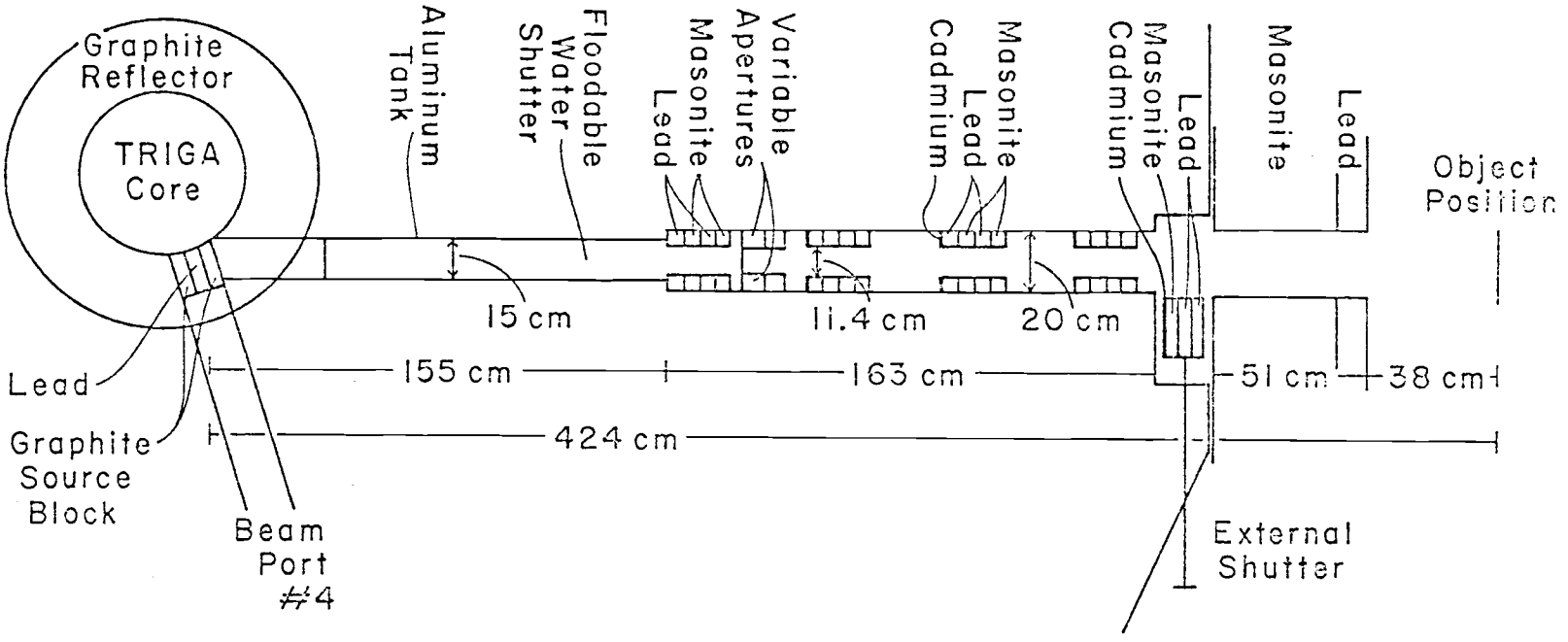

8.9 cm. Spaced cadmium, lead and masonite rings along the collimator remove from the beam neutrons that may scatter on the collimator walls. The collimator is designed with two separate shutters. Water which fills a large aluminum tank in the beam port acts as the first shutter. The water is pumped out of the tank when a series of radiographs are to be taken and then reflooded at the end of the day's exposures. A second shutter of cadmium, masonite and lead located near the end of the collimator is opened just prior to the reactor pulse and closed following. Beyond this shutter the collimator forms a rectangular tube 51 cm in length, 20 cm in width and 10 cm high.

The object location is about 38 cm beyond the collimator face. At this position the L/D ratio from unsharpness measurements is 30 in the horizontal direction and 41 in the vertical. The neutron flux at the object location measured by gold foil activation is 1.4×10^5 n/cm^2-sec/KW. At 3000 MW, peak pulsing power, this would be 4.2×10^{11} n/cm^2-sec. The gold cadmium ratio is 2.24 while the beam has an ASTM rating of N75-10. Table 2-1 shows the beam characteristics as measured with the ASTM Beam Purity Indicator (47). The beam is not very uniform as shown by the radiographic density contours of figure 2-3. A small object, however, may be satisfactorily radiographed in the center since the nonuniformity of the intensity pattern is not too significant over about sixty square centimeters.

Scattered neutrons from the object or the surrounding material of the beam port can cause imaging and contrast problems. For this reason it has been found to be advantageous to place a very fine collimator of exactly the size of the desired information field in

Table 2-1

ASTM BEAM PURITY INDICATOR

Location	Film Densities*
D1	.35
D2	.29
D3	1.45
D4	.32
D5	1.56

$\frac{D3-D1}{D3}$ (thermal neutron content) = .76

$\frac{D5-D3}{D3}$ (scattered neutron content) = .08

$\frac{D1-D2}{D3}$ (epithermal neutron content) = .04

$\frac{D1-D4}{D3}$ (low energy gamma content) = .02

* Exposure on gadolinium foil - SR film

Figure 2-3

RADIOGRAPHIC DENSITY

CONTOURS OF BEAM PORT #3

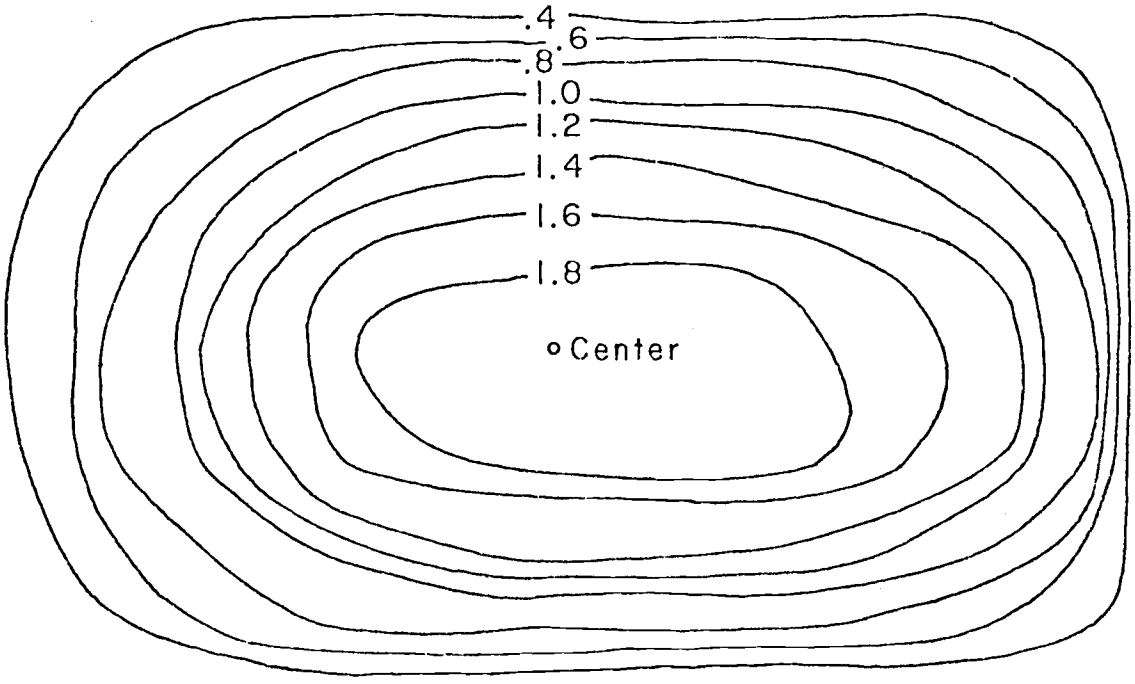

Scale: ⊢—⊣ = 1 cm

front of the object. In this manner, all neutrons that are not directly in line with the area of interest will be removed from the beam and are unable to scatter into the area of interest, fogging the radiograph.

2.4 Objects

The neutron beam leaves the collimator and passes through the object to be radiographed. Not all objects are suitable subjects. The object must have good contrast to neutron inspection. Ordnance devices have been radiographed at Oregon State University under the ballistic cycle which is a rapid dynamic event involving the burning of a hydrocarbon inside a heavy metal containment. The neutrons are very sensitive to hydrogenous material and thus, in this case, determine the presence or absence of powder. Due to the limitations of the high speed motion system and also the scattering nature of hydrogen attenuation for neutrons, individual powder grains cannot be resolved. Superior contrast can be gained however by the addition of a few powder grains doped with a material possessing a very large neutron absorption cross section such as gadolinium. These doped grains are very definitely resolved in the image and may be observed for movement over the course of the firing event.

High speed motion neutron radiography of two phase flow has also been demonstrated at Oregon State. At high frame rates the action is essentially frozen, showing air bubbles injected in a small water tank as they are formed and rise. Radiography through water is difficult due to the very significant neutron scatter. An antiscatter

grid of laminated vapor deposited gadolinium or gadolinium paint on aluminum spacers is advisable for improving the resolution capability (48). The antiscatter grid is located between the object and the detector, allowing only neutrons emerging from the object at shallow angles to pass through the scintillator screen.

The object must also be such that it transmitts a sufficient beam intensity for imaging. A transmission of between 10% and 1% of the incident beam is acceptable depending on the neutron source strength. If the object is too opaque a problem of neutron intensity will result that may have ramifications that affect the entire high speed motion system design. The physical dimensions of the object may also be a limitation as the field of view is specified by the scintillator screen and image intensifier size. Small objects of less than 40 mm in diameter are capable of being radiographed at Oregon State with the high speed motion system described here.

2.5 Neutron Scintillator Screen

The neutron beam transmitted through the object strikes a neutron scintillator screen. This screen converts the spatially modulated neutron signal to light. If the object transmits 10% of the neutron beam, the screen will see about 4.2×10^{10} n/cm^2-sec. For a high speed motion radiograph at 10,000 frames/second, the screen must be capable of forming an image with a fluence of less than 4×10^6 n/cm^2. The scintillator must also have a rapid response in order that each frame of a high speed movie be a distinct image and not a blurring of several frames together. This requires a rapid decay of the light

yield from the scintillation process. The orientaion of the scintillator must also be in transmission for input to the intensifying device as indicated in figure 1-3C.

A variety of scintillators have been tested for use in the high speed motion system and are discussed more fully in Chapter IV. Lithium fluoride-zinc sulphide (LiF-ZnS) scintillators however have been found to be best suited for the high speed motion requirements. Results of analytical and experimental studies show scintillators of 2/1 weight ratio of ZnS to LiF in a thin layer (about 0.13 mm) to be among the finest. The LiF is enriched to over 90% of Li-6 content for greater neutron absorption in this nucleus. The neutron reaction in Li-6 releases an alpha particle and tritium nucleus plus kinetic energy to cause excitation of the ZnS phosphor. The ZnS emitts blue light at a peak wavelength of 450 nm with limited phosphorescence to allow individual framing at over 5000 frames/second.

2.6 Image Intensifier

The image created by the scintillation process must be recorded for later study. Although a high speed movie camera could be focused on the scintillator screen, the light yield of the scintillator is insufficient to expose the film in the camera. Therefore, an image intensifier is used to increase the light intensity. Image intensifiers are electo-optical devices which operate by photocathode conversion of the incident light to electrons, acceleration of the electrons across a voltage potential, and scintillation of an output phosphor by the more highly energetic electrons (49,50). At Oregon

State University a two stage 40 mm diameter ITT Image Intensifier (No. F4751) is employed. Overall dimensions are 25 cm in length and 9 cm in diameter. The radiant power gain measured by the manufacturer is a factor of 332 for the combined stages. Resolution of the intensifier is listed at 35 line pairs/mm. The image intensifier is coupled to the scintillator by pressure contact of the flat scintillator surface to a flat fiberoptic input surface of the intensifier. The 40 mm diameter size of the intensifier tube is a limiting feature on the size of the object that may be radiographed with the system.

Since the image intensifier operates with photocathodes and phosphors, it, just as the scintillator screen, is subject to image retention from frame to frame. Thus phosphors must be specified that have rapid decay characteristics. Additionally, phosphors possess spectral response characteristics which, if possible, should be chosen to provide the optimum response from the scintillator to the intensifier and from the intensifier to the recording film. The ITT image intensifier uses an S-20 photocathode which has a wide spectrum response with a maximum at about 425 nm wavelength. Figure 2-4 shows the S-20 sensitivity along with several other photocathodes. This spectral sensitivity matches quite well with the zinc sulphide phosphor of the scintillator. The efficiency of the S-20 (Sb-K-Na-Ca) is one of the highest for photocathodes and the persistance is on the order of 10^{-12} seconds. The output faceplate of the intensifier uses P-11 phosphor (ZnS:Ag(Ni)) which emits in the blue spectrum with a peak wavelength of about 474 nm. The persistance of P-11 is considered

Figure 2-4

PHOTOCATHODE SPECTRAL RESPONSE *

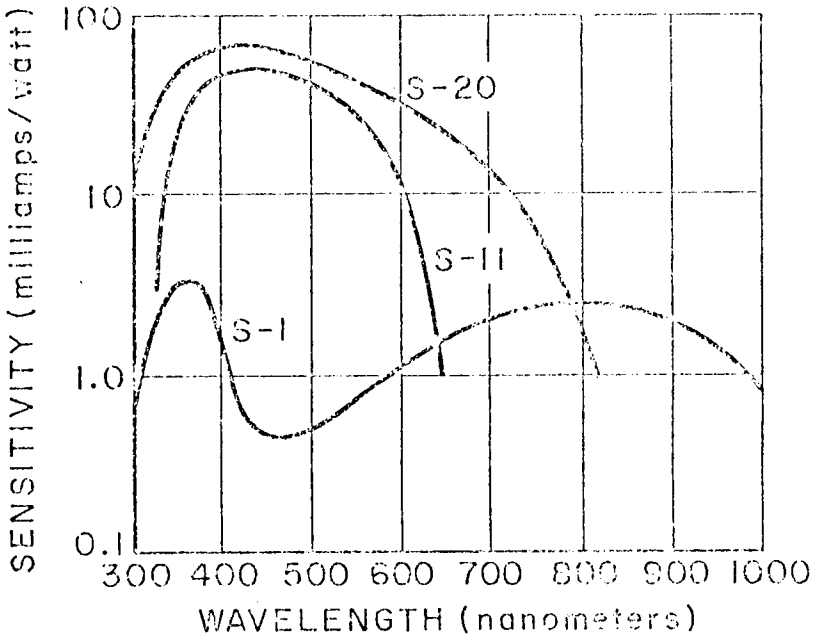

* B.H. Vine, "Electro-Optical Devices", Chapter 6, Applied Optics and Optical Engineering, R. Kingslake, Ed., Academic Press, New York, 1965, p. 231.

short, dying away in a hyperbolic order (51).

2.7 High Speed Camera and Film

High speed photography has been performed in engineering and science, and camera systems come in several different types (52,53). A Hycam model K20S 4E rotating prism camera is used at Oregon State University and focuses on the output faceplate of the intensifier. With 400 foot 16 mm film rolls this camera can operate at up to 11,000 frames/second, although it is normally run with 125 foot rolls which limit the fastest frame rate to about 8000 frames/second. The rotating prism system utilizes a camera shutter factor of 2.5 which means that at 5000 frames/second the exposure per frame is $\frac{1}{2.5 \times 5000}$ = 80 μsec. The optical coupling between the intensifier and camera is a focused lens. The standard camera lens is 25 mm, f 1.9. An improvement may be made by substituting a superior lens having a greater light collecting capacity. A 55 mm, f 1.2 lens is used at Oregon State University and provides improved film exposures over the original lens.

The last stage of the high speed motion operation is the film and film development. A variety of 16 mm films are available to be used. Fine grain rapid arts recording (RAR) films are found to be the best. Table 2-2 lists the characteristics of these films. The fine grain films, RAR 2496 and RAR 2498, are superior to the others for detail and contrast in the radiograph. Other 16 mm films such as TRI-X and cineradiographic film are also inferior to the RAR 2496 and 2498. Development of the film is accomplished with a Cramer

Table 2-2

CHARACTERISTICS OF RAPID ARTS RECORDING FILMS[1]

Kodak Film Number	Spectral Sensitivity	Exposure Index for P-11 (2)	Resolving Power Class (3)	Granularity Class (4)	Development
2485	Ext. Red Pan	800	L	C	857, 95°F 2½ min
2475	Ext. Red Pan	400	ML	C	DK-50, 68°F 8 min
2484	Pan	350	M	MC	D-19, 68°F 4 min
2479	Ext. Red Pan	200	M	MC	D-19, 68°F 8 min
2498	Pan	64	H H	VF M	Reversal D-19, 68°F 8 min
2476	Ext. Red Pan	50	H	M	D-19, 68°F 8 min
2496	Ext. Red Pan	40	VH	M	D-19, 68°F 8 min

[1] Eastman Kodak data, September 1971

[2] Reciprocal of exposure for density of 0.10

[3] Classifications: L-Low (below 55 lines/mm), ML-Moderately Low (56-68 lines/mm), M-Medium (69-95 lines/mm), H-High (96-135 lines/mm), VH-Very High (136-225 lines/mm)

[4] Classifications: C-Coarse, MC-Moderately Coarse, M-Medium, F-Fine, VF-Very Fine.

Mark IV automatic processor. Time and temperature are adjustable to good accuracy. Best results are found with low temperature (68°F - 20°C) development which keeps the film graininess to a minimum. Higher temperature development increases the contrast but granularity becomes a problem. Hand processing of the films can be done in a Morse G-3 Developer. The film in this case must roll through the solutions and back up on itself a number of times. A definite improvement in film quality is found with an automatic processor in which the emulsion layer of the film remains free of all surfaces throughout the entire development process.

2.8 Synchronization of Events

While the high speed system is relatively simple as presented, the working capability is dependent upon proper sequencing of events. For operation, the neutrons from the reactor pulse must pass through the object at the instant of the dynamic event while the high speed camera is running at the desired speed. Each of these parameters is time dependent and so they must be synchronized together. The camera has a necessary start up time from initiation to operating speed. The reactor pulse also has a time delay from initiation of the transient to the instant that the neutron burst reaches the object. The object dynamic event must then be timed to occur when these other two sequences are synchronized. For continuous events such as two phase flow in a system, the reactor pulse may be signaled to occur once the high speed camera has reached the proper frame rate. Events such as the firing of an ordnance device require more precise synchronization

since the firing must be simultaneously initiated.

The synchronization system used for ordnance device high speed motion neutron radiography is shown in figure 2-5. The reactor is taken to a low power level and prepared for the pulse initiation. The high speed camera is started and initiates the synchronization by closing an internal circuit when it reaches a desired length of film run after start up. This length is related to frame rate by the start up curves for the camera given in figure 2-6. The camera circuit is connected to a double pole-double throw relay which closes when the desired speed is reached. One circuit of the relay closes the firing circuit of the OSTR pulse, thus initiating the transient. As will be discussed in the next chapter, the OSTR pulse reaches a peak value approximately 188 milliseconds after initiation. Knowing this time delay from initiation to peak power allows synchronization of the firing event by the use of a timer. Thus the relay circuit also initiates a timing box which consists of two Nuclear Data Clock/Time Base Modules (ND 536) linked in series to provide three significant figures of timing accuracy. Each Clock/Time Base is capable of timing for $1. \times 10^{-5}$ to 99×10^{3} seconds. For the high speed motion neutron radiography of ordnance devices, one Clock/Time Base is set for 170 milliseconds and the second for 16 milliseconds. This totals 186 milliseconds at which time the reactor should be approaching peak power. The timer then trips the firing circuit for the device.

Successful operation is not always guaranteed. The sequence involves mechanical devices which may fluctuate in response, particularly in the reactor transient initiation and the dynamic event

Figure 2-5

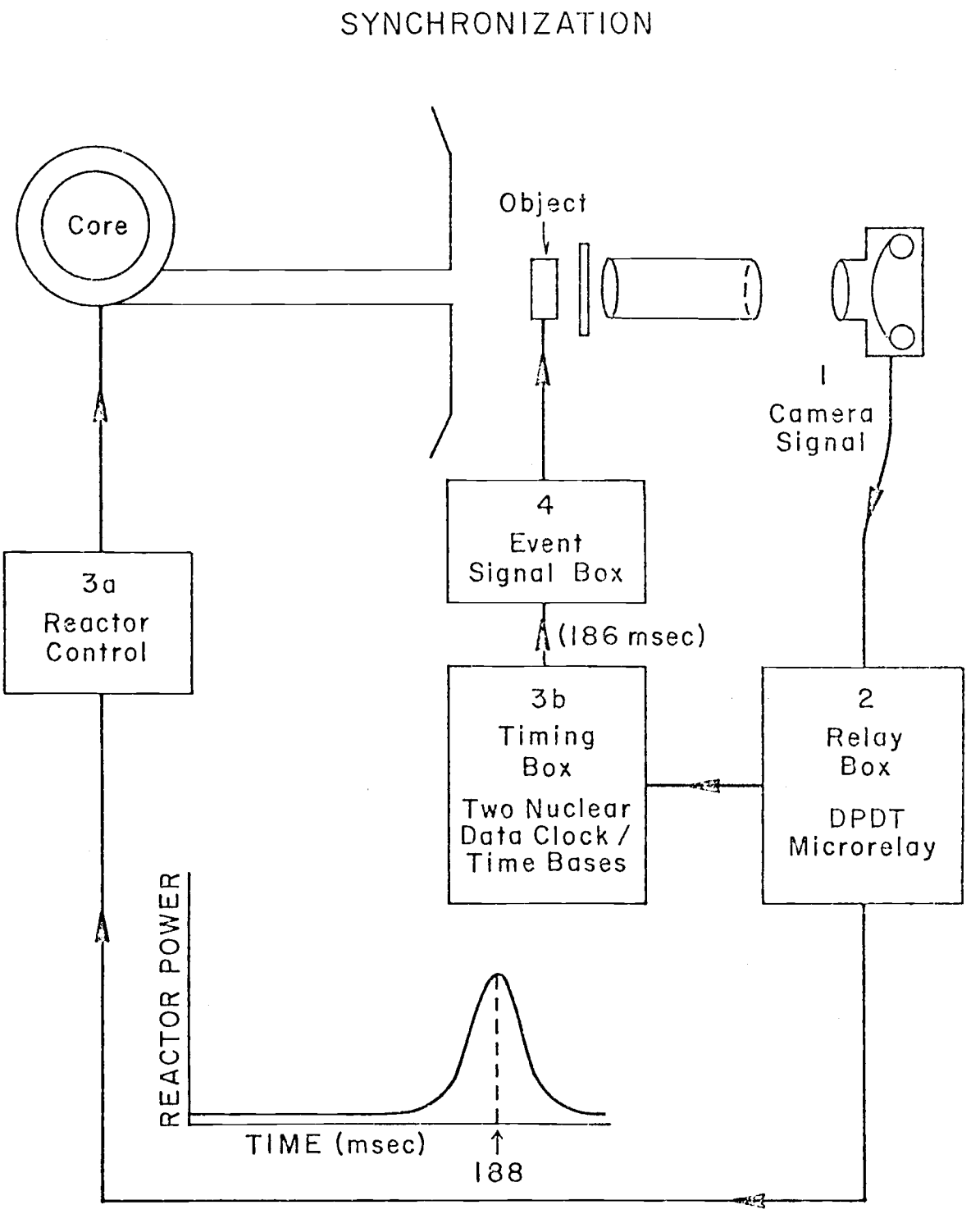
SYNCHRONIZATION
Core
Object
1
Camera
Signal
4
Event
Signal Box
(186 msec)
3a
Reactor
Control
3b
Timing
Box
Two Nuclear
Data Clock /
Time Bases
2
Relay
Box
DPDT
Microrelay
REACTOR POWER
TIME (msec)
188

Figure 2-6

START UP CURVES FOR HYCAM
HIGH SPEED MOTION PICTURE CAMERA

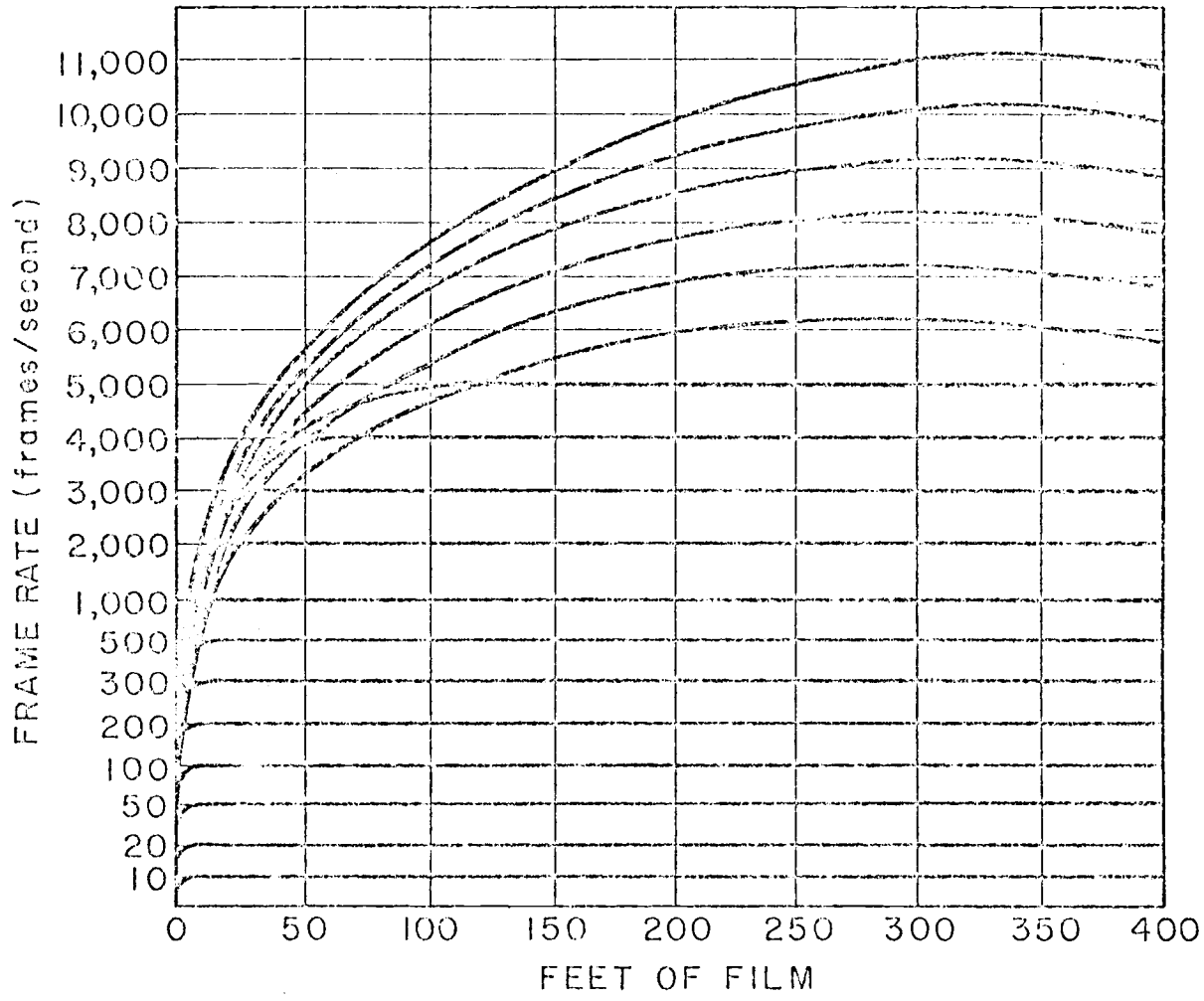

firing. The two millisecond interval from the firing of the device at 186 milliseconds to the peak at 188 milliseconds allows for some slack in the trigger mechanism. This is especially loose since thermal neutrons travelling at 2200 m/sec should need about 2 milliseconds to reach the object position from the reactor core. This causes the peak neutron flux at the object position to occur around 190 milliseconds after initiation. Although it is preferred that the event occur near the peak of the pulse, this is not essential as good results may be obtained when the event is on the leading or trailing edge of the pulse.

This system has been found to work satisfactorily providing proper synchronization about 50% of the time. This is acceptable if the event being radiographed is relatively easy to set up and repeat. For unrepeatable, one time events, a more reliable synchronization mechanism may be desired. In this case, sensitive detectors could trigger the event when the increasing signal of the pulse is sensed. The ease of construction of the timing circuitry system makes it preferable to this second system for the ordnance work. The actual synchronization component circuit diagrams are provided in Appendix D.

III. TRIGA PULSING CAPABILITY

3.1 OSTR Characteristics

The Oregon State TRIGA Reactor (OSTR) is a 1 MW steady state TRIGA Mark II reactor manufactured by General Atomic Corporation (54,55). The application of the OSTR as the neutron source for high speed motion neutron radiography stems from its capability of safely undergoing a pulse to very high power levels. This is due to the large prompt negative temperature coefficient in the fuel design. The pulse is initiated by a large step insertion of reactivity when the reactor has been critical at a low power level. The rapidly rising fuel temperature from the supercritical chain reaction causes the reactor reactivity to decrease, turning the power rise around and ultimately reducing the reactor to a subcritical state. The power traces shown in figure 3-1 are recorded from the reactor linear power channel by a high speed Honeywell Visicorder. A symmetric pulse is shown with the peak power and pulse width dependent on the magnitude of the initial reactivity step.

The essential element of the large prompt negative temperature coefficient for reactivity in TRIGA reactors is zirconium hydride in the fuel. The fuel elements consist of a homogeneous mixture of uranium-zirconium hydride alloy composed of 8.0 weight per cent U enriched to 20% U-235 in stainless steel cladding. The zirconium hydride (ZrH_n, where n = 1.7) acts as a moderator of neutrons with at least as good a moderating ability as free hydrogen when the

Figure 3-1

POWER TRACES FOR OSTR PULSES

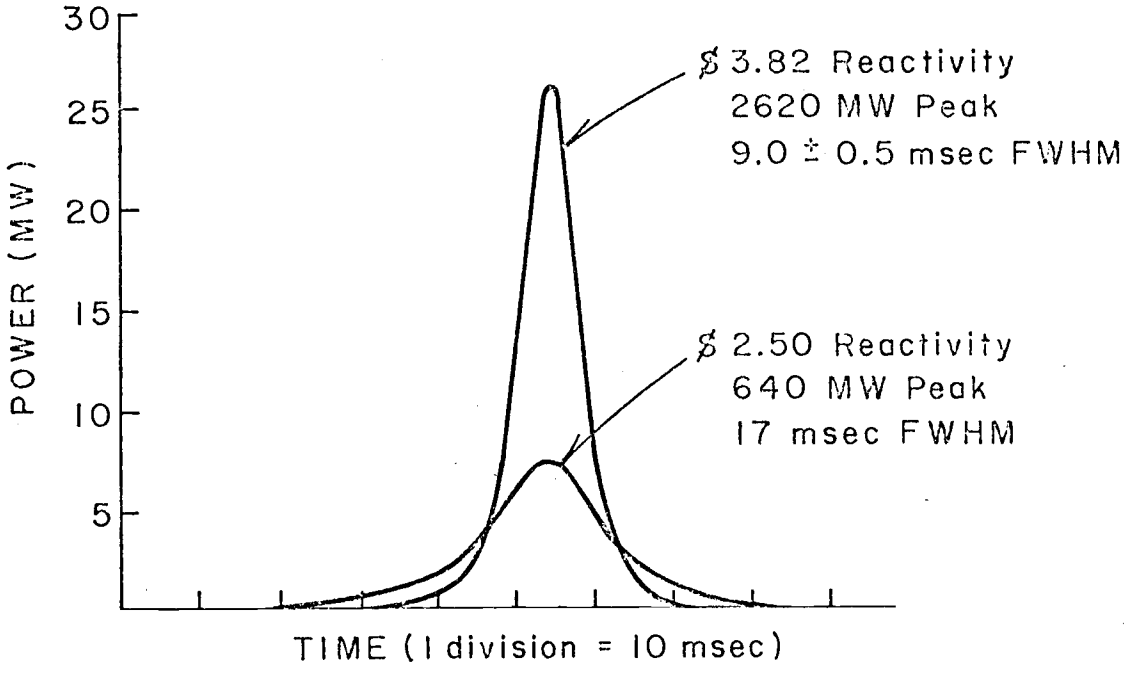

neutrons are above 0.14 eV. At the low neutron energies however the ZrH_n is quite ineffective for moderation. The hydrogen atoms in the ZrH_n lattice act as harmonic or Einstein oscillators with vibrational energy states of $h\nu$ = 0.14 eV. Neutrons can therefore gain or lose integral multiples of 0.14 eV in a scattering collision with the ZrH_n. In the case of neutron thermalization in the reactor the neutrons will only lose energy to the ZrH_n vibrational states as long as they are above $h\nu$. Once a neutron is below $h\nu$ it can continue to lose energy by conventional scattering with the bound hydrogen nuclei or may gain energy $h\nu$ by scattering with an excited Einstein oscillator. A neutron which slows down to thermal energy in the reactor water moderator may enter the fuel element and be "kicked up" in energy before interaction with a U-235 atom. At the higher energy level the neutron will have a lower probability of absorption in the fuel and may escape the fuel element without causing fission. As the zirconium hydride increases in temperature due to fission in the fuel, the number of Einstein oscillators increases, reducing the probability of fission in the fuel and thus resulting in a strong negative temperature coefficient for reactivity (56-58).

The overall prompt negative temperature coefficient is the combination of the cell effect, doppler effect and leakage. The cell effect is the previously described ZrH_n component of the fuel which at higher temperature increases the probability of a neutron escaping the fuel by hardening the neutron energy spectrum. This accounts for about 65% of the total prompt negative temperature coefficient. 15% of the prompt negative temperature coefficient is due to doppler

broadening of the U-238 capture resonance as the temperature increases. Increased core leakage at higher temperature accounts for the remaining 20%. The overall prompt negative temperature coefficient for the OSTR is 1.2×10^{-4} $(\Delta k/k)/°C$ (56).

3.2 Nordheim-Fuchs Model

The pulsing characteristics for the OSTR may be derived analytically from the Nordheim-Fuchs model equations (59). This model is verified yearly at Oregon State University by nuclear engineering class experiments and provides a fairly good estimate of the pulsing characteristics. An extension of the Nordheim-Fuchs model for variable heat capacity has been made and compared by numerical analysis to experimental results on the OSTR (60,61). However, the constant heat capacity model is sufficient for understanding the pulsing operation.

The Nordheim-Fuchs model assumes that the delayed neutron effects may be neglected and that the heat generated remains in the fuel over the short time period of the transient. Summarizing the results of the model, the peak power of a pulse is

$$P = \frac{C\beta^2(\$-1)^2}{2\alpha\ell} \qquad (3\text{-}1)$$

where P is the power, C is the heat capacity of the fuel, β is the delayed neutron fraction, \$ is the reactivity inserted in dollars, α is the negative temperature coefficient for reactivity and ℓ is the neutron generation time. The peak power then is proportional to the square of the reactivity insertion above prompt critical. Typical

values for the parameters on the OSTR are: $\beta = 0.007$, $C = 6.34 \times 10^4$ watt-sec/°C (838 watt-sec/°C/fuel element x 88 fuel elements), $\alpha = 1.2 \times 10^{-4}$/°C and $\ell = 43$ μsec. The average temperature rise under this model is given by

$$\Delta T = \frac{2\beta(\$-1)}{\alpha} \tag{3-2}$$

which is directly proportional to the reactivity insertion above prompt critical. Furthermore, the total energy release from the pulse is

$$E = C\Delta T = \frac{2C\beta(\$-1)}{\alpha} \tag{3-3}.$$

Finally, the width of the pulse at half maximum value is

$$\tau = \frac{3.524\ell}{\beta(\$-1)} \tag{3-4}$$

which is inversely proportional to the reactivity insertion above prompt critical.

3.3 Pulsing Operation

In order to generate a pulse it is necessary to insert the reactivity as rapidly as possible. In the OSTR this is accomplished with a transient control rod that is pneumatically operated. The reactor is taken to a low power level, usually between 5 and 100 watts, on the shim, safety and regulating control rods. When the reactor is stable, the transient rod is fired by injection of compressed air. The rod is rapidly ejected from the core, striking a spring shock absorber. The rod remains out for about 7 seconds and then falls back automatically. During this time, the reactor undergoes its excursion and returns to subcritical. The peak power

is determined from equation 3-1 based on the reactor design parameters and reactivity worth of the transient rod. The maximum achievable power is restricted by the maximum transient rod worth.

The limitation in pulsing is not solely a function of reactivity but involves a licensed limitation on peak fuel temperature. During the pulse, there is no time for heat transfer to take place requiring the fuel elements to sustain very large temperature increases. In fact, the temperature profile for the fuel elements shows a peak temperature near the surface of the element rather than the center due to greater interaction with no heat removal. Standard TRIGA fuel elements are designed to be operated below 1000°C. The OSTR is required not to exceed 800°C on the hottest fuel element to provide a safety margin. Since the average fuel temperature is about half the peak temperature value for the OSTR, the reactivity limit based on an 800°C peak would be around \$4.34. Normally TRIGA reactors are licensed for routine operation only up to 3.2% $\Delta k/k$ or \$4.60 prompt reactivity insertion. These reactivity limitations provide a considerable safety margin for the fuel as even the 1000°C peak fuel temperature limit is considered conservative (58).

Within these licensing restrictions, the maximum reactivity worth on the transient rod is obtained by orienting the OSTR core such that the transient rod is located near the peak core flux. Figure 3-2 is the core loading diagram for this configuration. The fuel elements are shifted from symmetrical locations about the geometric center of the core (the central thimble) toward beam port #4. The core center in this case is around fuel elements B-3 or C-4 such that the transient

Figure 3-2

OSTR CORE LOADING

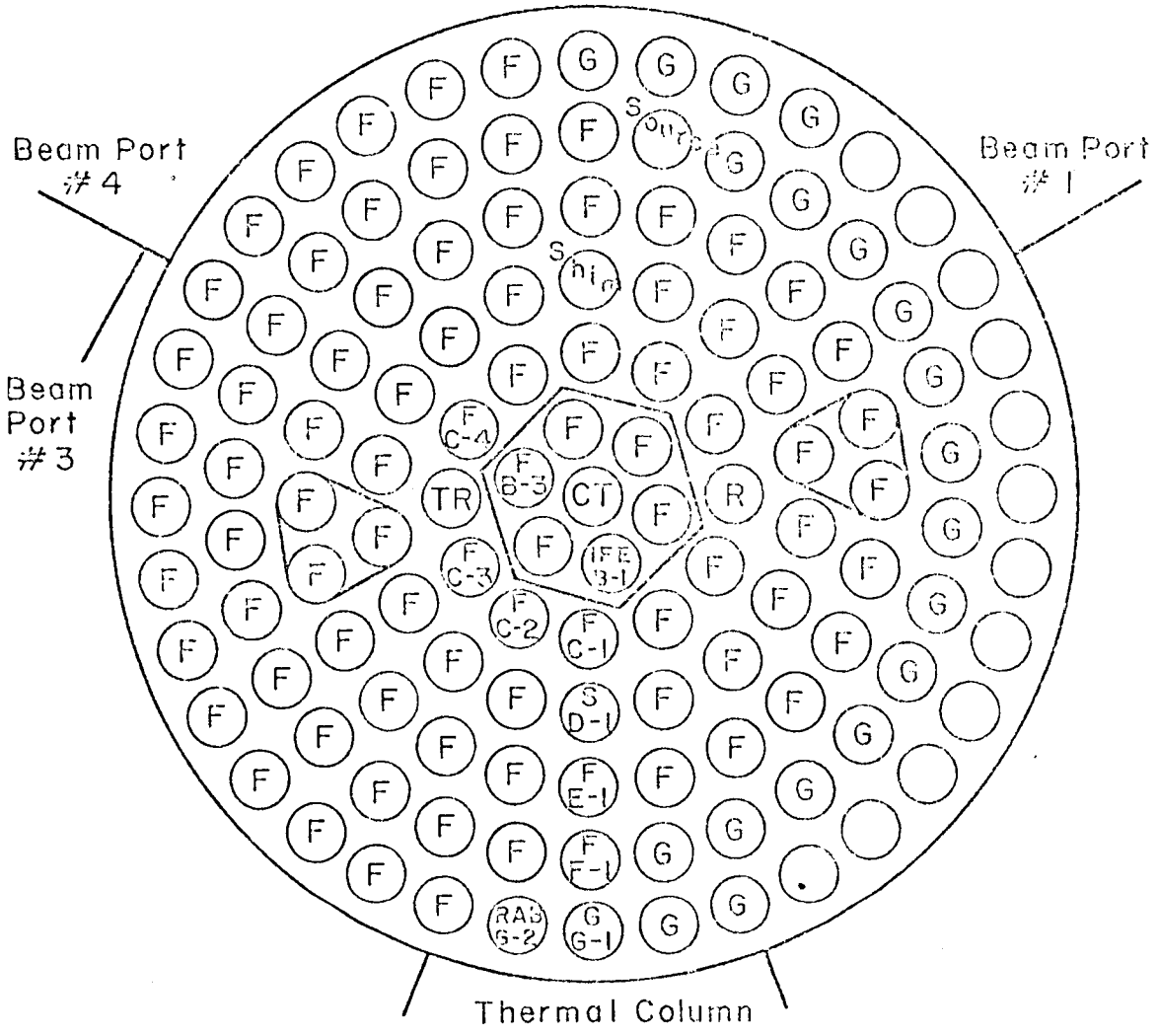

F Fuel Element
TR Transient Rod
R Regulating Rod
G Graphite
IFE Instrumented Fuel Element
S Safety Rod
Water
CT Central Thimble
RAB Rabbit

rod at location C-4 is very close to the peak flux. The reactivity worth of the transient rod for this configuration has been measured to be $3.82. Equation 3-1 then predicts a peak power from a pulse to be about 2750 MW.

Experimental values of peak power, temperature rise and pulse width for various reactivity insertions are given in table 3-1. Agreement between theoretical and experimental values is only fair. The pulsing response of the reactor is, of course, a function of core history and subject to changes in core reactivity excess from day to day operation. Also the instrumentation for such a rapid and severe event can only be expected to provide close to exact values. Thus peak power is not perfectly consistent between pulses, although, pulses can normally be generated about every 15 minutes with a consistency of within 100 MW peak power for the same reactivity insertion. The temperature values of table 3-1 are provided by an instrumented fuel element, B-1, in the core having a thermocouple located in the fuel just below the surface. B-1, however, is not located at the core center due to the core shift around the transient rod (see figure 3-2) and therefore gives only an approximate temperature reading for the hottest element. For the maximum pulse, this element registered 500°C. The Nordheim-Fuchs model equation predicts an average temperature rise of 329°C for such a pulse leading to the suspicion that the hottest element may have a peak temperature between 650 and 700°C.

By equation 3-4 the width of the $3.82 pulse should be 7.68 msec. Experimental values indicate slightly larger widths which is in

Table 3-1

TRIGA PULSE DATA*

Reactivity Inserted ($)	Peak Power (MW)	Instrumented Fuel Element Temp. (°C)	Pulse Width FWHM (m sec)
2.50	640	325	17
2.75	940	365	14.5
3.00	1300	400	11.5
3.25	1760	438	10.5
3.50	2160	465	9.5
3.82	2620	500	9

* Experiment, January 1974

agreement with the variable heat capacity Nordheim-Fuchs model. This pulse width allows very suitable radiography for events of a few milliseconds duration. Over the 7 to 9 millisecond width the neutron exposure may vary by 50%. Preferably over a shorter span of 2 to 4 milliseconds the exposure is uniform enough for quite good radiographic results. In fact, fluctuations of 50% in exposure can be sustained and retain adequate detail detection. For the case of slower events, the pulse may be adjusted to have greater width and allow a more integrated exposure at a slower frame rate. A pulse of $2.00 will have, according to equations 3-1 and 3-4, a peak power of 350 MW and a half width of 21.6 milliseconds. In dropping from 2750 MW to 350 MW peak pulse power, the pulse width has increased from 7.68 to 21.6 milliseconds. This indicates that the frame rate needs to be reduced by a factor of about nine to maintain the same neutron exposure per frame. Thus, with the lower pulsing operation the number of frames that may be taken over the width of the pulse is reduced.

3.4 Increasing Peak Power

Naturally, there is an interest in generating the largest pulse possible. At the OSTR, this is a function of the core loading around the transient rod to provide the greatest reactivity worth. It is possible however to generate larger pulses by using multiple transient rods. The Annular Core Pulse Reactor (ACPR) of Sandia Corporation is a TRIGA reactor which is capable of pulsing to 20,000 MW (62). This is attained by the precise timing of the ejection of 5 transient rods. The ACPR also is not under the $4.60 maximum prompt reactivity

insertion licensing restriction of the normal TRIGA cores.

The pulsing capability may also be altered by changing the values of the parameters of the Nordheim-Fuchs model. By loading more fuel into the OSTR core, the heat capacity will increase and allow for some increase in the peak power. Other changes that could increase the pulsing capability would be to decrease the neutron generation time (ℓ) or the negative temperature coefficient (α). This has been done by the development of Fuel Lifetime Improvement Program (FLIP) fuel elements by General Atomic. Table 3-2 lists the relative characteristics of the standard and FLIP TRIGA elements. The FLIP fuel with its higher enrichment and burnable poison has a reduced neutron generation time and a temperature dependent negative temperature coefficient. Experiments on the Torrey Pines Reactor have been performed to study some effects of adding FLIP fuel (18 elements) to a standard TRIGA core (63). Table 3-2 includes the parameters found for the mixed standard and FLIP fuel element core. Using the Torrey Pines figures, a \$3.82 reactivity pulse would generate a peak power of about 3437 MW or 25% higher than a standard core pulse. The width would be about 6.96 msec. Moving to a full FLIP core, the pulse height should increase considerably and the pulse width become narrow due to the much smaller value of ℓ. Actual calculation under the Nordheim-Fuchs model is difficult due to the variable negative temperature coefficient and heat capacity values.

Although FLIP fuel offers an increased pulse height due to its characteristics, it does not necessarily mean more neutron yield which is the important factor in radiography. The power in a reactor

Table 3-2

TRIGA FUEL CHARACTERISTICS

Parameter	OSTR (standard)	FLIP	Torrey Pines
composition	8 wt% $U\text{-}ZrH_{1.7}$ 20% enriched U-235 stainless steel clad	8.5 wt% $U\text{-}ZrH_{1.6}$ 70% enriched U-235 1.6 wt% Er stainless steel clad	18 FLIP elements 68 standard fuel elements
ℓ	43×10^{-6} sec	$16\text{-}20 \times 10^{-6}$ sec	39×10^{-6} sec
β	0.007	0.0071	0.007
α	fairly constant 1.2×10^{-4}/°C	variable 4×10^{-5}/°C @100° 1×10^{-4}/°C @500°	variable with an average value of 1.05×10^{-4}/°C
C	variable, but approximately 838 watt-sec/°C-fuel element with 88 fuel elements	825 + 161(T-25) watt-sec/°C-fuel element	variable, but approximately 840 watt-sec/°C-fuel element with 86 fuel elements

core is related to the flux by integration over the core of

$$P = \int K\Sigma_f \phi dV \tag{3-5}$$

where P is power in MW, K is energy yield per fission, Σ_f is the fission cross section, ϕ is the flux and dV is an infintesimal volume element. As Σ_f increases, the flux will decrease to maintain the same power. Since FLIP fuel is 70% enriched, it has a considerably higher Σ_f than standard TRIGA fuel. Σ_f in FLIP fuel is about 0.525 cm^{-1} and in standard fuel about 0.139 cm^{-1}. Thus the flux at the same power in FLIP fuel may be expected to be a factor of 3.76 lower than in the standard fuel, other factors remaining constant. This argument is simplistic since FLIP fuel has a much harder neutron energy spectrum. This can be utilized under flux trapping conditions such that the high energy neutrons leaving the core become thermalized in the flux trap enhancing the thermal neutron neutron flux. Results of studies on the OSTR with a FLIP fuel core demonstrate only an 11% reduction in thermal flux in the reflector region. For radiography it may be possible to obtain as good or better thermal fluxes in a beam port provided the collimator input is located in a reflector or flux trap region as opposed to the fuel region. Additionally the power certainly can be increased by increasing the core volume, such as adding more fuel, but the flux will not necessarily be enhanced. Conversely a decreased core volume could be made to generate a larger peak neutron flux.

3.5 Synchronziation with the High Speed System

The pulsing of the OSTR is a mechanically induced event which must coincide with the dynamic event to be radiographed. Chapter II

discussed the synchronization process used for ordnance work which operates with a timing mechanism to trigger the event at a preselected time after pulse initiation. A determination of the time from the transient rod firing signal to the peak of the pulse can be performed with a NaI detector and a multichannel analyzer. The analyzer is used in the Multichannel Scaling Mode (MCS). The pulse is detected on a NaI crystal due to the prompt fission gamma rays emitted from the core. With the MCS set for 1 millisecond per channel, a series of maximum reactivity insertion pulses are performed. The important questions are what effect does the starting power for the pulses have on the time to the peak of the pulse and how consistent is the timing.

Table 3-3 contains data on a series of pulses starting from power levels between 5 and 500 watts. A statistical analysis of the table 3-3 data shows a highly significant variation of the time to reach peak power and starting power. A 95% confidence interval for the time from a 100 watt initiation is 188 $\pm$ 4.77 milliseconds. Any change in the variation of the time to peak height as a function of starting power cannot be shown as there is insufficient data to confirm this. The results suggest that for a maximum pulse with a 9.5 millisecond pulse width, an event timed to occur 188 milliseconds after the pulse initiation would, on the average, miss taking place within the half width only once every twenty times. Experience has not been that good, as the dynamic event involves mechanical devices that do not respond instantaneously or consistently. This timing technique however has proved satisfactory for the type of work that has been performed.

Table 3-3

TEST OF TIME TO PEAK POWER

Starting Power (W)	Time to Peak (millisec)	Peak Power (MW)
500	176	2600
500	188	2420
100	186	2470
100	187	2480
100	192	2480
100	187	2500
20	193	2540
20	200	2540
20	192	2520
20	194	2550
5	203	2560
5	200	2560

IV. SCINTILLATORS

4.1 Introduction

In high speed motion neutron radiography, one of the most important single components is the scintillator screen for neutron signal detection. The scintillator incorporates a high cross section neutron absorbing material, which emits ionizing radiation following a neutron interaction, and a scintillation material. The secondary radiation excites the scintillation material, producing a light signal. Scintillator screens used for standard neutron radiography are capable of generating a radiograph with the least neutron exposure of all techniques. This quality is of course the major reason for their selection for use in the high speed application. The fact that the scintillation technique converts the neutron signal to light is also beneficial. The light may be manipulated optically for both intensification and recording.

Scintillation screens are not all the same. The variation involves both the type of materials and the performance. In high speed motion work the necessary characteristics are not only good image quality and speed, but use in transmission orientation, compatibility with other optical components and rapid light decay characteristics to avoid image retention (phosphorescence from frame to frame. Table 4-1 lists the most common neutron radiography scintillator screens.

Table 4-1

NEUTRON RADIOGRAPHY SCINTILLATORS

Type	Neutron Reaction	Light
lithium fluoride-zinc sulphide	$^{6}Li(n,\alpha)^{3}H$	blue (450 nm)
B-10 - zinc sulphide	$^{10}B(n,\alpha)^{7}Li$	blue (450 nm)
gadolinium oxybromide (GdOBr:Er)	Gd(n,γ)-IC	bluegreen (540 nm)
gadolinium oxysulphide (Gd_2O_2S:Tb)	Gd(n,γ)-IC	bluegreen (540 nm)
cerium activated glass	$^{6}Li(n,\alpha)^{3}H$ or $^{10}B(n,\alpha)^{7}Li$	blue (395 nm)

4.2 Lithium Fluoride-Zinc Sulphide Scintillators

The lithium fluoride-zinc sulphide screens are most widely used for their high yield, ease of manufacture and durability. They consist of a mixture of lithium fluoride (LiF) powder, zinc sulphide (ZnS) powder and a binder material. These scintillators have been studied for both scintillation neutron counters and radiography screens (64-70). The lithium fluoride component is enriched in its content of Li-6, normally to 95% or more. Li-6 has a neutron absorption cross section of 953 barns. Upon neutron interaction, the following reaction occurs;

$$^{6}Li + n \rightarrow \alpha + {}^{3}H + 4.78\ MeV \qquad (4\text{-}1)$$

such that an alpha particle and tritium nucleus are released back to back with 4.78 MeV of energy. The α will carry away 2.05 MeV and the triton 2.73 MeV. These two ionizing particles will travel through the scintillator, losing their energy by excitation and ionization. Should the particles excite the zinc sulphide crystals, light scintillation at about 450 nm wavelength will occur as the lattice returns to the ground state. A binder of polyethylene, plastic, lucite, epoxy, sodium silicate or other appropriate material is required to hold the LiF and ZnS powders together in the mixture and usually, though not necessarily, to an aluminum substrate.

4.3 Boron-10 - Zinc Sulphide Scintillators

A very similar scintillator is the B-10 loaded ZnS scintillator. The boron component is often boric acid (H_3BO_3) enriched in B-10 but

may be in other forms. The B-10 has a neutron absorption cross section of 3837 barns yielding an alpha particle and 2.78 MeV following a neutron interaction.

$$^{10}B + n \rightarrow \alpha + {}^{7}Li + \begin{cases} \gamma + 2.3 \text{ MeV} & (93\%) \\ 2.78 \text{ MeV} & (7\%) \end{cases} \qquad (4\text{-}2)$$

Ninety-three percent of the time, the α carries away 1.47 MeV of kinetic energy which may be converted to light by excitation of the ZnS scintillator component. A binder material holds the zinc-sulphide and boron components in mixture and onto a substrate. Boron-10 scintillators have been made for both detectors and neutron radiography screens (71,68). The boron-10 loaded scintillator has four times as great a cross section as ^{6}Li loaded scintillators with half the energy release of the $^{6}Li(n,\alpha)^{3}H$ reaction. Although it may be expected that B-10 would offer a superior scintillator, the results have been mixed (4,68,72-74). The B-10 scintillators do not necessarily yield as much light as the LiF type and more significantly they suffer from hydroscopic problems and lack durability.

4.4 Rare Earth Scintillators

X-ray technology has developed rare earth phosphors of gadolinium oxybromide and gadolinium oxysulphide for use as intensifying screens (75,76). The gadolinium component has a high thermal neutron absorption cross section of 46,000 barns which makes these phosphor screens also applicable to neutron detection. The gadolinium oxybromide (GdOBr:Er) screens are quite good neutron scintillator screens, having excellent resolution capability for scintillators. These screens emit a blue-

green light of around 540 nm wavelength. Green sensitive films are being developed to enhance the film response for medical x-ray applications. However, for neutron radiography the screens are not nearly as fast as the LiF-ZnS type. The gadolinium oxysulphide screens are very similar in characteristics to the gadolinium oxybromide. There have been developments to increase the light yield such that they are as fast as the slower LiF screens provided a panchromatic or orthochromatic film is used.

4.5 Glass Scintillators

Glass scintillators used for neutron detection are also applicable to neutron radiography. These consist of cerium activated glass which contains boron or lithium. The B-10 or Li-6 reaction to neutrons initiates the scintillation so that enrichment of these isotopes is preferred. Development of the glass scintillators has been for counting equipment (77,78), but further work on thin slices of the glass has resulted in suitable scintillators for neutron radiography (67). The advantage of these scintillators is in their transparency, allowing light generated deeper in the screens to be transmitted out than can take place in opaque granular scintillators. Also the completely homogeneous structure eliminates the mottle problem found in granular screens. Unfortunately, for radiography, this advantage can be a handicap as light generated too deep in a scintillator will actually deteriorate the resolution. The thicker the scintillator the more absorption efficiency but the poorer the resolution. The lithium doped cerium activated glass appears to have a greater light yield than the

boron (78). Thus an optimized glass scintillator for neutron radiography is about 1 mm thick containing 7% LiF enriched in Li-6 with the back surface blackened to avoid internal reflections (67). These scintillators emit blue light of around 395 nm wavelength but are not nearly as fast as the LiF-ZnS screens.

4.6 Scintillator Selection

The scintillator screen to be selected for the high speed motion system must operate in the transmission orientation for input to the optical system rather than the typical standard reflection orientation as indicated in figure 1-3C. A number of specific neutron scintillator screens have been tested for their performance in this transmission orientation and recorded on Kodak Contrast Process Ortho film. Table 4-2 lists the type of scintillator, manufacturer, relative light yield and image quality factor. The relative light yield is proportional to the reciprocal of the neutron exposure necessary to cause a film density of 0.95. The image quality factor is based on the VISQI test object using sensitivity counting (79). The greater the number of elements detected the superior the scintillator quality. VISQI sensitivity comparison is subject to observer interpretation and film density effects making a quantitative comparison between two screens only valid for fairly large differences. Results of the test though fall into the four groups of scintillator types. The LiF-ZnS screens all have image quality values in the high 40's to low 50's and are the fastest type of scintillator screen. The B-10 - zinc sulphide screens are slower and have markedly poorer image quality. The gadolinium

Table 4-2

COMPARISON OF SCINTILLATOR SCREENS

Type	Manufacturer	Relative Yield	Image Quality (sensitivity)
LiF-ZnS	Nuclear Enterprises NE 425 (0.18 mm)	45	50
LiF-ZnS	Nuclear Enterprises NE 425 (0.31 mm)	30	48½
LiF-ZnS	Nuclear Enterprises Scintillator A (0.1 mm)	20	45½
LiF-ZnS	R.H. Bossi #51 (0.1 mm)	20	50½
LiF-ZnS	R.H. Bossi #56 (0.24 mm)	50	51½
LiF-ZnS	C.E.N. Grenoble (0.24 mm)	40	49½
LiF-ZnS	A.R. Spowart	100	47½
^{10}B-ZnS	Nuclear Enterprises NE 402	12.5	45
^{10}B-ZnS	R.H. Bossi #30	12.5	32½
GdOBr:Er	General Electric (0.11 mm)	10	60½
Gd_2O_2S:Tb	Lockheed (0.064 mm)	10	59½
Gd_2O_2S	Apex Research	25	64½
Glass	Nuclear Enterprises NE 905 (1 mm)	10	51½

rare earth screens definitely demonstrate the best image quality but do not have as great a light yield. The glass scintillator has image quality comparable to the LiF-ZnS screens but one of the poorest light yields.

Limited image retention from frame to frame is an essential characteristic for high speed motion neutron radiography. The number of light photons emitted after the excitation of a scintillator follows an exponential law to a first approximation such that

$$n = n_o (1-e^{-t/\tau}) \qquad (4-3)$$

where n is the number of photons emitted, n_o is the total that will be emitted at infinite time after the event, t is time and τ is the decay constant. In the period of one decay constant, 63% of the total light is emitted. Glass scintillators have the smallest decay constants, on the order of 40-60 nanoseconds. This could conceivably allow frame rates as high as 8 million frames/second. The low light yield of the glass scintillators can present a problem at the very high frame rates requiring significantly increased light amplification.

Gadolinium containing screens have constants on the order of 400 μsec. While this may allow individual framing at low frame rates, at high frame rates there is a problem with overlapping of the image from frame to frame. This problem was tested on the high speed motion system using a high speed motor (2780 rpm) with eight cadmium spokes in front of an object. At full speed a spoke crossed the neutron beam every 2.6 milliseconds, chopping off the signal. For frame rates of 2000 and 5000 frames/second, the spinning wheel is only modestly

detected by either type of gadolinium screen. Apparently at these frame rates the image decay is sufficiently long to produce some image overlap from frame to frame which reduces the visibility of a true change. Since the gadolinium screens have a significantly better resolution capability they would be the preferred scintillator if the long time phosphorescence could be reduced, perhaps by a change in the activator. At low frame rates, below 1000 frames/second, they of course offer the best potential. The lower yield of these screens is not necessarily a limitation if sufficient amplification is present from the intensifier or low frame rates are used.

The ZnS(Ag) scintillators have decay characteristics composed of two components: a fast component having a decay constant on the order of 40-100 nanoseconds and a slower component on the order of 40-100 microseconds (80,81). The LiF-ZnS scintillators are capable of clearly detecting the spinning cadmium spokes discussed above at both 2000 and 5000 frames/second. Apparently, the fast component of the scintillation process carries sufficient information to allow independent imaging at these frame rates. Thus, the LiF-ZnS scintillators are the ones selected for development of the high speed motion neutron radiography system. They have high light yield, good resolution capability and sufficiently rapid decay characteristics to be useful in the range of 2000 to 10,000 frames/second.

4.7 Scintillator Construction

Although LiF-ZnS scintillators may be purchased commercially, they may be made without a great deal of difficulty in the laboratory.

The construction requires lithium fluoride powder enriched in Li-6, zinc sulphide powder and a suitable binder. The variables of construction are the ratio of the components, size of the particles and total thickness of the scintillator. Experimenters have constructed the LiF-ZnS scintillators using lucite, epoxy, polyethylene and even a radiation induced polymerization of plastic as the binder and have tried to optimize the design for the greatest light yield while retaining resolution capability. At Oregon State University, the author has constructed LiF-ZnS scintillators for the high speed motion neutron radiography system using a technique suggested by Chuck Hurlbut of Nuclear Enterprises. Lithium fluoride powder enriched in Li-6, zinc sulphide of nominal 10 micron grain size, sodium silicate and water are stirred together in a beaker. The LiF and ZnS are measured in the appropriate weight ratio of these components that are to make up the scintillator before mixing. Whereas in using lucite, epoxy and polyethylene, the amount of binder is specified, with the sodium silicate solution this is not feasible or necessary. The scintillator solution is poured into a dish which has an aluminum plate in the bottom. The LiF and ZnS powders which were in suspension settle to the surface of the plate. The remaining liquid is removed down to the surface of the powders. The scintillator will harden due to the sodium silicate binder and will have a smooth surface. Figure 4-1 demonstrates the construction technique.

The relative ease of the above process makes it especially interesting. No heating or special presses are required. Thickness control is difficult however, for any exacting requirement, as it

Figure 4-1

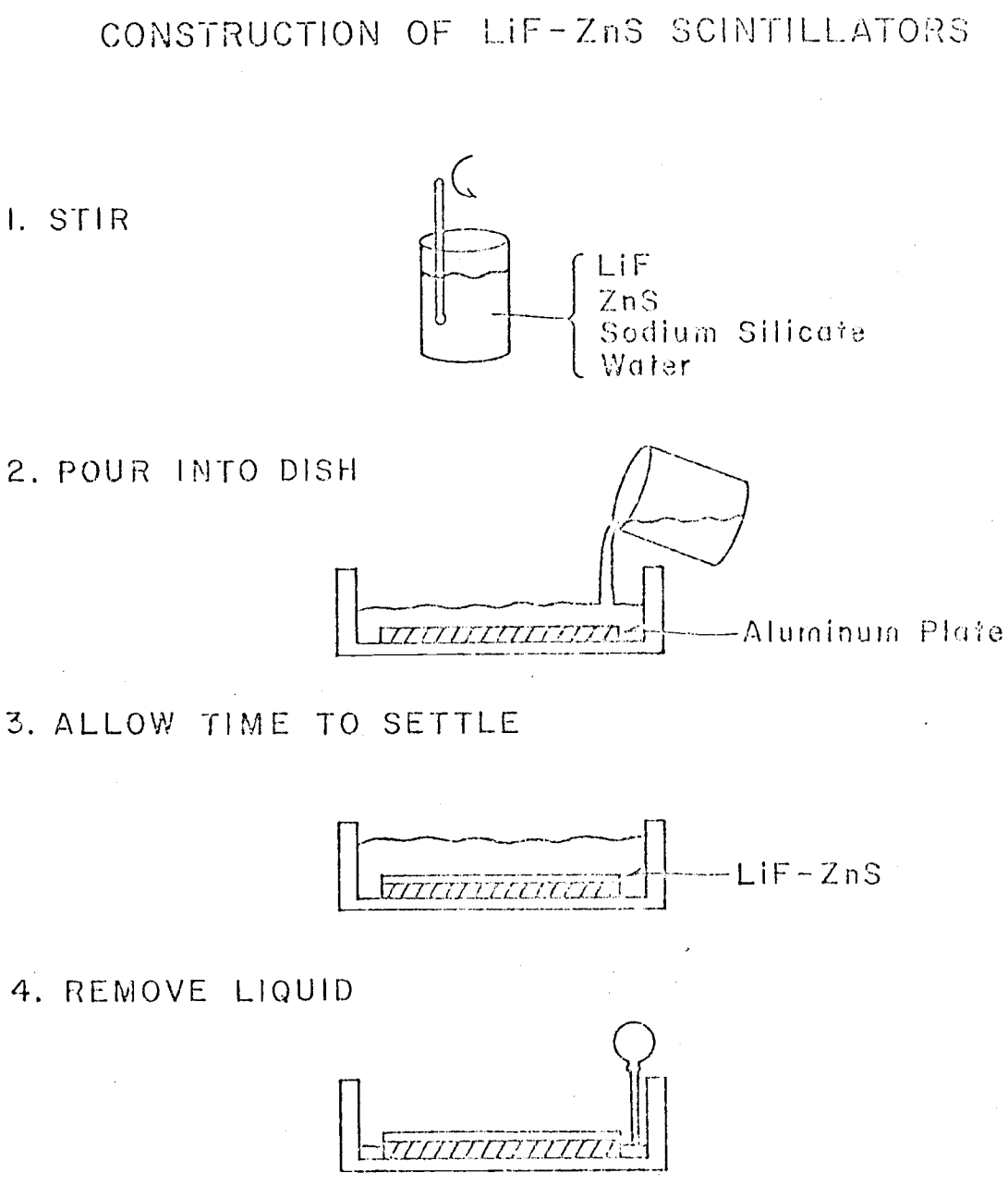
CONSTRUCTION OF LiF-ZnS SCINTILLATORS
1. STIR
LiF
ZnS
Sodium Silicate
Water
2. POUR INTO DISH
Aluminum Plate
3. ALLOW TIME TO SETTLE
LiF-ZnS
4. REMOVE LIQUID

is based on the amount of material in solution and the area of the dish. Care should be taken in mixing the materials as mechanical damage to the ZnS(Ag) scintillator powder can cause a loss in light yield (82). At the same time, insufficient mixing will result in a somewhat heterogeneous scintillator which does not perform as well as homogeneous mixtures (65). These difficulties plus any changes in purity of the materials hinders consistant results from batch to batch in scintillator construction. The binder content in the sodium silicate construction process is not known, but should be minimal.

The reason for establishing this "in house" capability for constructing scintillators stems not only from the desire to make the best scintillator but also from the loss of quality that occurs with use and the batch to batch changes present even in commercially purchased LiF-ZnS screens. The surface of a scintillator may easily become dirty or marred, reducing the light yield and resolution. In fact, two of the very best scintillators used at OSU have shown this deterioration with time. Scintillator A and scintillator #51 of table 4-2 were originally considered the finest but today are not as good as some of the others as a result of their considerable use. The batch effect is not specifically shown in table 4-2 but has been found to be present in both commercially purchased and laboratory constructed scintillators. In some instances the light yield will change considerably between apparently identical scintillators. Thus, it is of value to be able to contruct more scintillators in order to duplicate the best performance when many runs are expected.

Table 4-3 indicates the relative performance of a number of scintillators constructed at OSU. Both the ZnS to LiF weight ratio and scintillator thickness were varied. The percentage of the neutron beam attenuated by the scintillators was measured using a narrow beam technique to estimate the relative absorption efficiency. The relative light yield is the same as in table 4-2. Image quality is again measured by the VISQI test object and is therefore only a good indicator of relative merit for significant changes. The total sensitivity is divided into the resolution and contrast sensitivity factors of the VISQI object.

4.8 Scintillator Computer Model

The experimental construction of scintillators is somewhat limited in the number that can be investigated and by the expense. Therefore a study was performed to make a relatively simple computer model for the scintillator. As discussed earlier, the scintillator operates by the absorption of a neutron in a Li-6 nucleus causing the back to back release of a 2.73 MeV tritium nucleus and a 2.05 MeV alpha particle. These particles track through the scintillator screen, losing energy by ionization and excitation (see figure 4-2). Excitation of ZnS by the energetic particles will generate light in the scintillator which escapes to expose the imaging film. It may be expected that the greater the amount of energy that can be deposited in ZnS from a neutron beam striking the scintillator, the greater the scintillator light yield. The more LiF present in the scintillator the more neutrons will be absorbed, but they will not be as likely to cause

Table 4-3

OSU CONSTRUCTED LiF-ZnS SCINTILLATORS

Identity	Wt. Ratio (ZnS/LiF)	Thickness (mm)	Absorption (%)	Relative Yield	Image Quality Res.	Con.	Total
#55	1/2	.13	13.5	15	21½	25½	47
#53	1/1	.13	10.5	20	25½	26½	52
#58	2/1	.08	4.3	7.5	17½	15½	33
#52	2/1	.10	7.3	20	25	27	52
#51	2/1	.10	8.8	20	25	25½	50½
#59	2/1	.15	11.3	35	24½	27½	52
#57	2/1	.19	13.8	43	24½	27	51½
#56	2/1	.24	18.2	50	24½	27	51½
#54	4/1	.13	6.2	20	23	21½	44½
#63	2/1	.13	-	25	22½	22½	45
#61	3/1	.12	-	15	21½	21	42½
#62	4/1	.13	-	15	21	19½	40½

Figure 4-2

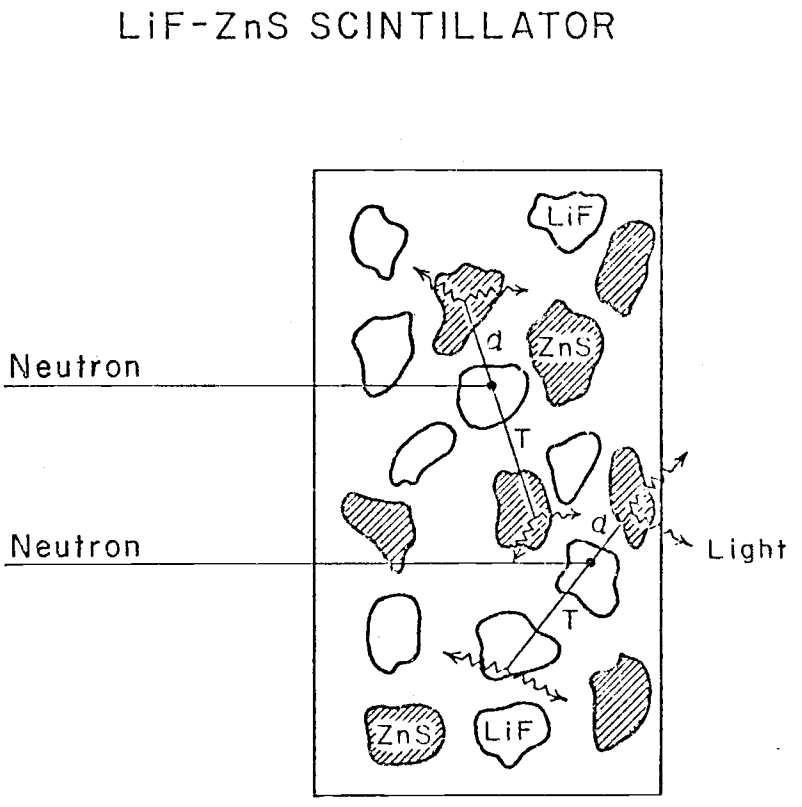
LiF-ZnS SCINTILLATOR
Neutron
Neutron
LiF
ZnS
α
T
α
T
Light
ZnS
LiF

ZnS scintillation. The more ZnS present, the more likely a scintillation will occur following neutron absorption but the less likely that the initial absorption will take place. Thus, some optimum ratio of the two components should exist.

This problem may be analyzed in the computer by a slab model of the scintillator as shown in figure 4-3. The materials are considered half thicknesses with reflecting boundaries. The distance A is equivalent to one half the ZnS grain size and thickness B-A is determined from the volume ratio of ZnS to LiF based on the weight ratio and densities of the materials. Neutron interactions are initiated randomly in the LiF component of the scintillator. The alpha and triton depart back to back at a random angle. If the ranges of the alpha and triton particles are known, then the track length for each particle in the ZnS section of the scintillator may be computed and equated to energy deposited. Normalization of this value with respect to the neutron absorption efficiency due to the LiF content completes the analysis. The slab model for the scintillator may be altered to simulate the scintillator as spherical grains of ZnS surrounded by LiF. This is accomplished by using the average chord method (83). The average chord length through a spherical grain is equated to the average chord length through a slab. This comparison suggests that a spherical model of the ZnS grain would look the same in the computer as the slab model when the ZnS layer is taken to be one sixth of the grain size. Figure 4-4 indicates this adjustment. Either the slab or spherical model may be tested with the same computer program by properly assigning the ZnS thickness.

Figure 4-3

SLAB GEOMETRY SCINTILLATOR MODEL

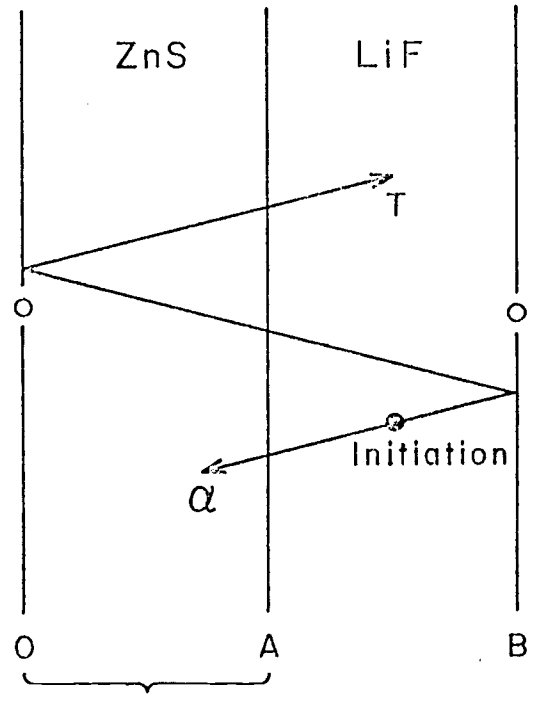

Figure 4-4

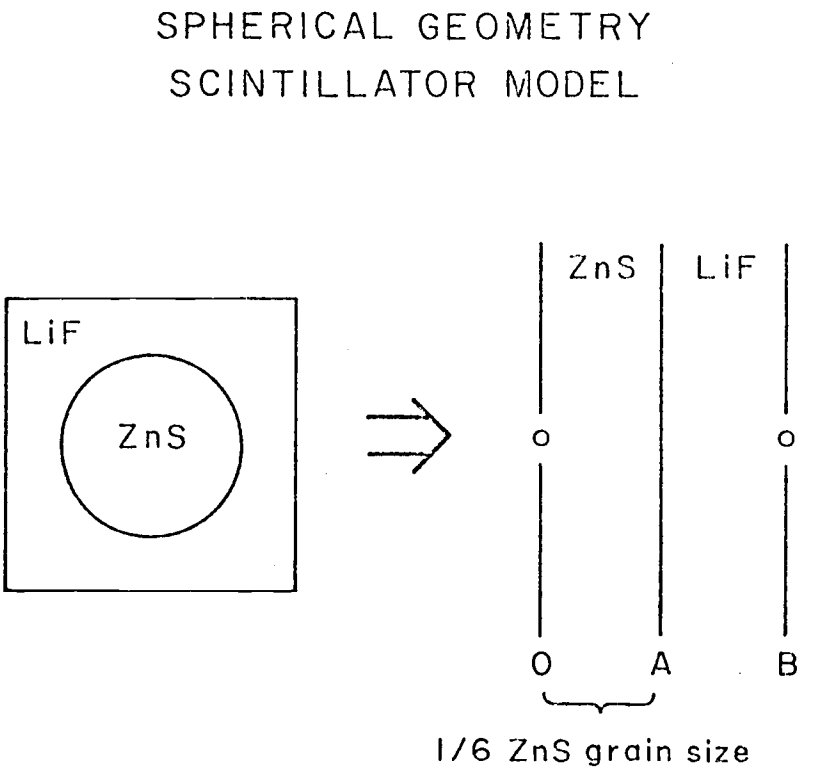
SPHERICAL GEOMETRY
SCINTILLATOR MODEL
LiF
ZnS
ZnS
LiF
O
A
B
1/6 ZnS grain size

The slowing down of heavy particles in matter follows a Bragg curve, shown in figure 4-5, and has a fairly constant range value. This allows a single computation of the range of the triton and alpha. Knowing these values the scintillator model may be run, tracking the alpha and triton particles along their respective ranges and equating the distance traversed in either LiF or ZnS to energy deposited in the respective materials. Estimates for the ranges of the particles are given in table 4-4 as calculated from a semiempirical formula for ranges of heavy particles (84). The alpha has twice the charge, greater mass and less initial energy, and therefore, a much shorter range than the triton. The stopping power of a material for particles in the Mev energy range is a function of electron cloud density. The ZnS material has a greater electron cloud density than LiF, and the particles should show a shorter range. The semiempirical formula demonstrates this only slightly. The estimated ranges are very close in value for either ZnS or LiF which allows a simplification of the calculations by using an average range in the scintillator of 27.6 microns for the T and 4.94 microns for the α. The energy loss along the particle track will not be constant as noted earlier by the Bragg curve. This curve of energy loss may be included in the computer model as two pieces with the particles yielding 69% of their initial energy over the first 85% of their range and then yielding the remaining 31% of their energy over the last 15% of their range.

The program for performing this analysis is called "SCINTLR" and is listed in Appendix A. It uses a random number generator to select the location of neutron absorption in the LiF region of the model.

Figure 4-5

TYPICAL BRAGG CURVE FOR SLOWING DOWN OF HEAVY PARTICLES

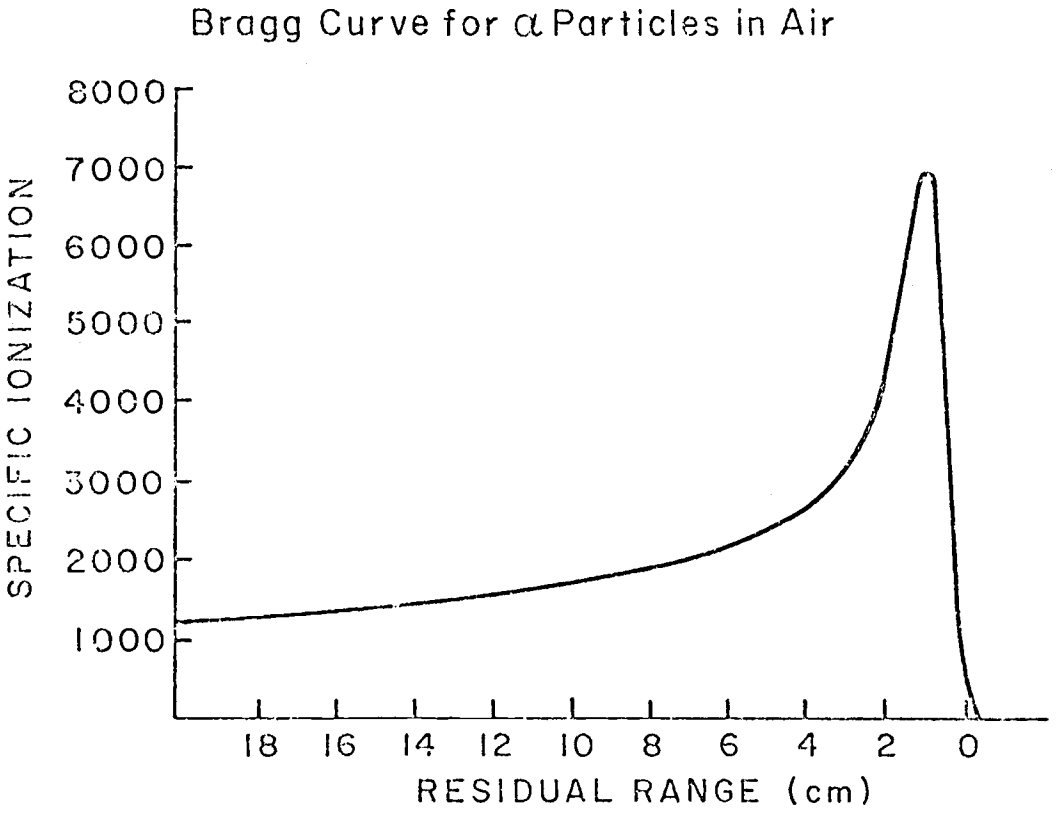

Table 4-4

PARTICLE RANGES

	Triton	Alpha
Energy	2.73 MeV	2.05 MeV
Charge	+1	+2
Mass	3	4
Range in LiF	28.1 microns	5.08 microns
Range in ZnS	27.2 microns	4.79 microns
Average Range in Scintillator	27.6 microns	4.94 microns

Although attenuation through the total scintillator is exponential, over the very thin section considered it may be taken as linear. A random number is also used to select the angle of release of the triton particle. In slab geometry the cosine of the angle has an equal probability distribution and thus the random number selects a cosine value from -1 to 1. The program tracks the triton particle determining the energy deposited in ZnS. This continues for the number of histories to be run, summing the energy in ZnS. The program then repeats through the same random number sequence for the alpha particle using the negative of the cosine of the angle of release for the back to back reaction. The grand total of the energy deposited for the number of histories run is the sum of the results for each particle. This value must be normalized for the number of histories and also for the absorption efficiency of the scintillator calculated from the LiF content and thickness.

4.9 Computer Optimized LiF-ZnS Scintillator

SCINTLR has been run for various weight ratios of ZnS to LiF at a scintillator thickness of 0.127 mm. The relative light yield based on the energy deposited in ZnS grains from a neutron beam are shown in figure 4-6. Experimental results of 0.127 mm thick scintillators constructed at Oregon State University are also shown. The maximum yield appears to occur at 2 to 1 ZnS to LiF for the spherical model and experimental scintillators. The slab model shows a peak around 3 to 1 ZnS to LiF. The computer model results do not show a very significant change from the maximum with the higher weight ratios.

Figure 4-6

RELATIVE LIGHT YIELD VERSUS WEIGHT RATIO FOR LiF-ZnS SCINTILLATORS

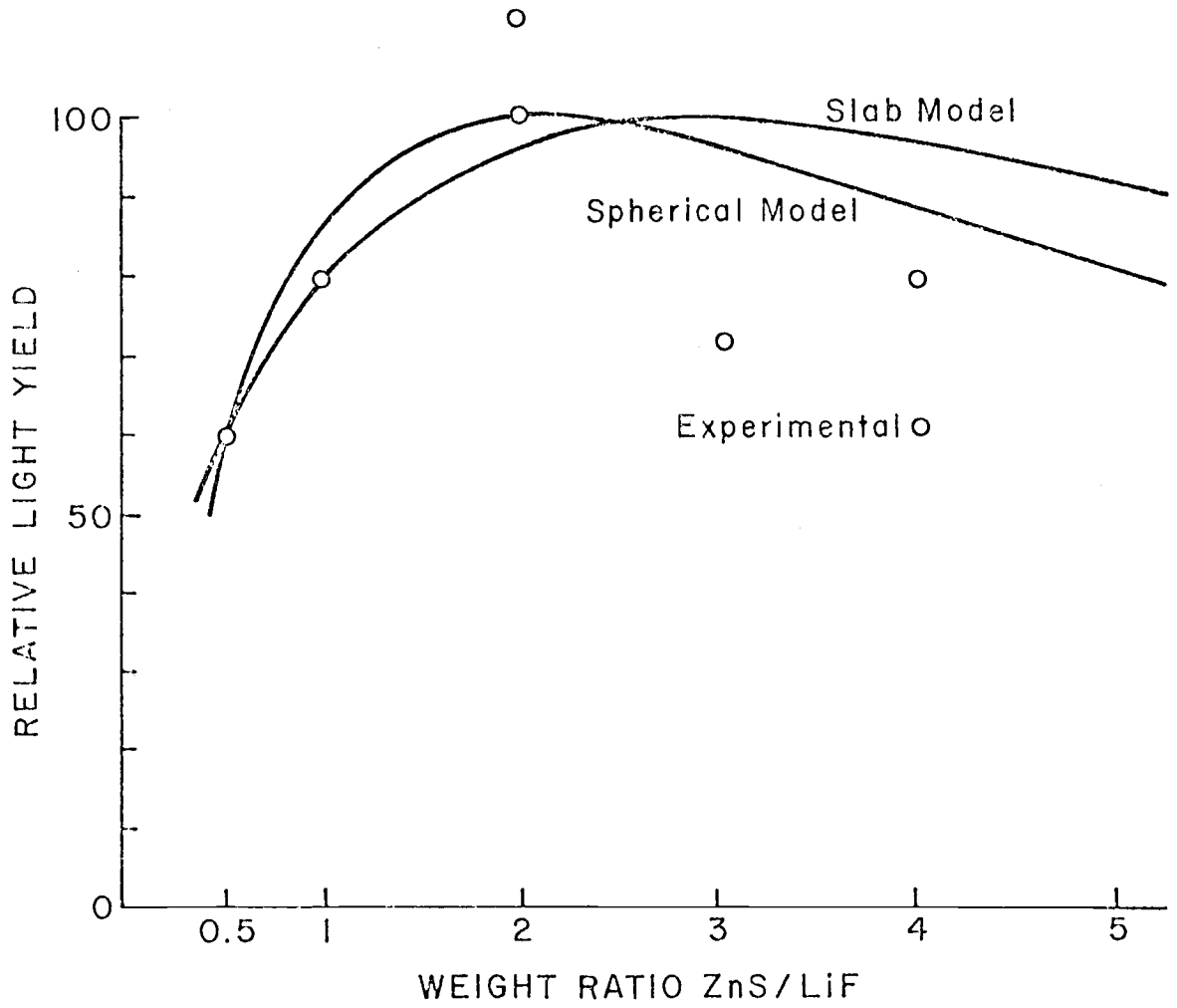

The maximum yield at a ratio of 2 to 1, ZnS to LiF found experimentally and in the computer model agrees with Stedman (64) but not with Spowart and Wang (67,65) who found higher ratios near 4 to 1 to yield the greatest light. Their actual experimental values, however, indicate that the change in film density for a change in weight ratio over the range of 2 to 1 to 5 to 1 is less than 10%, similar to the model.

The scintillator model predicts that at a constant weight ratio as the ZnS grain size is increased, the light yield decreases. This means that the optimum would be a homogeneous mixture of LiF and ZnS of infinitely small grains. In this case, the light yield would be proportional to the volume fraction of ZnS times the scintillator efficiency:

$$Y = \frac{W}{1.6 + W} \left(1 - e^{-\Sigma t/(1 + .62W)}\right) \qquad (4\text{-}4)$$

where Y is the yield, W is the weight ratio of ZnS to LiF, Σ is the macroscopic absorption cross section and t is the thickness. Differentiating and setting the value equal to zero allows computation of the weight ratio for maximum light yield which is found to be 1.86.

Although it would be expected that particle grain size should affect the scintillator light yield, experiments on grain size effects are not easily performed as grain size specifications are rarely exact. Spowart (67) actually found 10 μm ZnS to generate more light than the 7 μm in his scintillators. He worked primarily with 20 μm grains though and indicates that these results were poorer so that the 10 μm size is advocated as the optimum. Wang (65) found 25 μm ZnS grains, which he considered small, to have the best resolution and that

smaller grains decreased the sensitivity slightly. Stedman (64), in comparing 5, 12 and 18 μm ZnS, concluded that the choice of grain size was of no significance and, therefore, used 12 μm. At Oregon State University, nominal 10 μm ZnS grains are employed for scintillator construction.

The effect of grain size, however, does influence the scintillator computer model in that as the grain size increases, the optimum weight ratio for light yield increases. This is shown in figure 4-7. In fact, the difference between the slab model and spherical model is a factor of 3 in the grain size where the ZnS region is grain size/2 for the slab and grain size/6 for the spherical case. For the spherical model of grains 10, 60, 130 and 200 microns, the optimum ZnS to LiF weight ratios are calculated to be 2, 3, 4 and 6 to 1, respectively. This may be significant in that construction of scintillators using larger grains or a technique that does not homogeneously distribute the grains but allows clumping would demonstrate an optimum at a higher weight ratio.

The computer model, of course, has been idealistic in that it assumes the scintillator consists of a completely solid mass of LiF and ZnS material. In fact, the scintillator must have a binder material to hold it together, and the particles of ZnS and LiF that go into the construction will not be packed to the crystalline density but in settling out in the construction process will form some percentage of completely packed. The binder may be added to the model by keeping the ZnS grain size constant and considering the binder with the LiF. For simplicity, the range of the alpha and triton

Figure 4-7

RELATIVE LIGHT YIELD VERSUS WEIGHT RATIO
AS A FUNCTION OF GRAIN SIZE
(SPHERICAL MODEL)

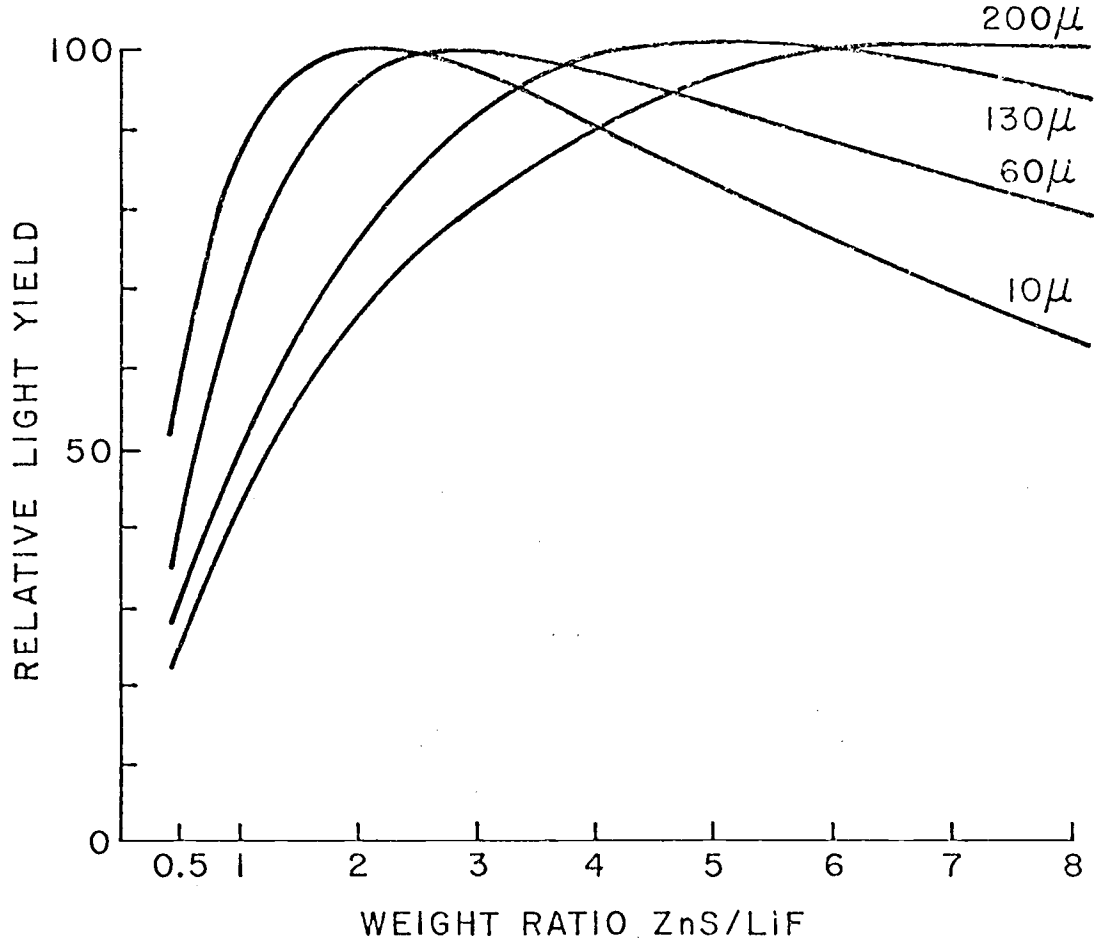

in the binder is taken to be the same as the average value used for LiF and ZnS. The packing effect may be accounted for by adjustment of the absorption efficiency of the scintillator.

Due to the construction technique of the scintillators, the binder content and packing effect are very difficult to determine. However, the absorption efficiency may be used to estimate these values. Figure 4-8 shows the calculated scintillator efficiency at various binder content and packing density combinations. A scintillator having 40% binder at 50% packing has a calculated efficiency as a function of weight ratio similar to the experimental scintillators. Recalculation of the light yield as a function of weight ratio using the 40% binder, 50% packing in the computer model results in the curve of figure 4-9, which is not significantly different from the previous curves showing an optimum at a weight ratio of 2 to 1, ZnS to LiF. Thus the computer model predicts the greatest light yield from a LiF-ZnS scintillator of nominal 10 μm ZnS grains to be obtained with a 2 to 1 weight ratio of ZnS to LiF.

4.10 Image Quality in LiF-ZnS Scintillators

While the scintillator model is helpful in understanding the operation of the scintillator screens, it does not answer all the questions that should be asked. For high speed motion neutron radiography, the light yield, provided it is sufficient, is not necessarily of prime importance since an image intensifier is used. The resolution of the scintillator however is very important and should not necessarily be sacrificed for greater light. The experi-

Figure 4-8

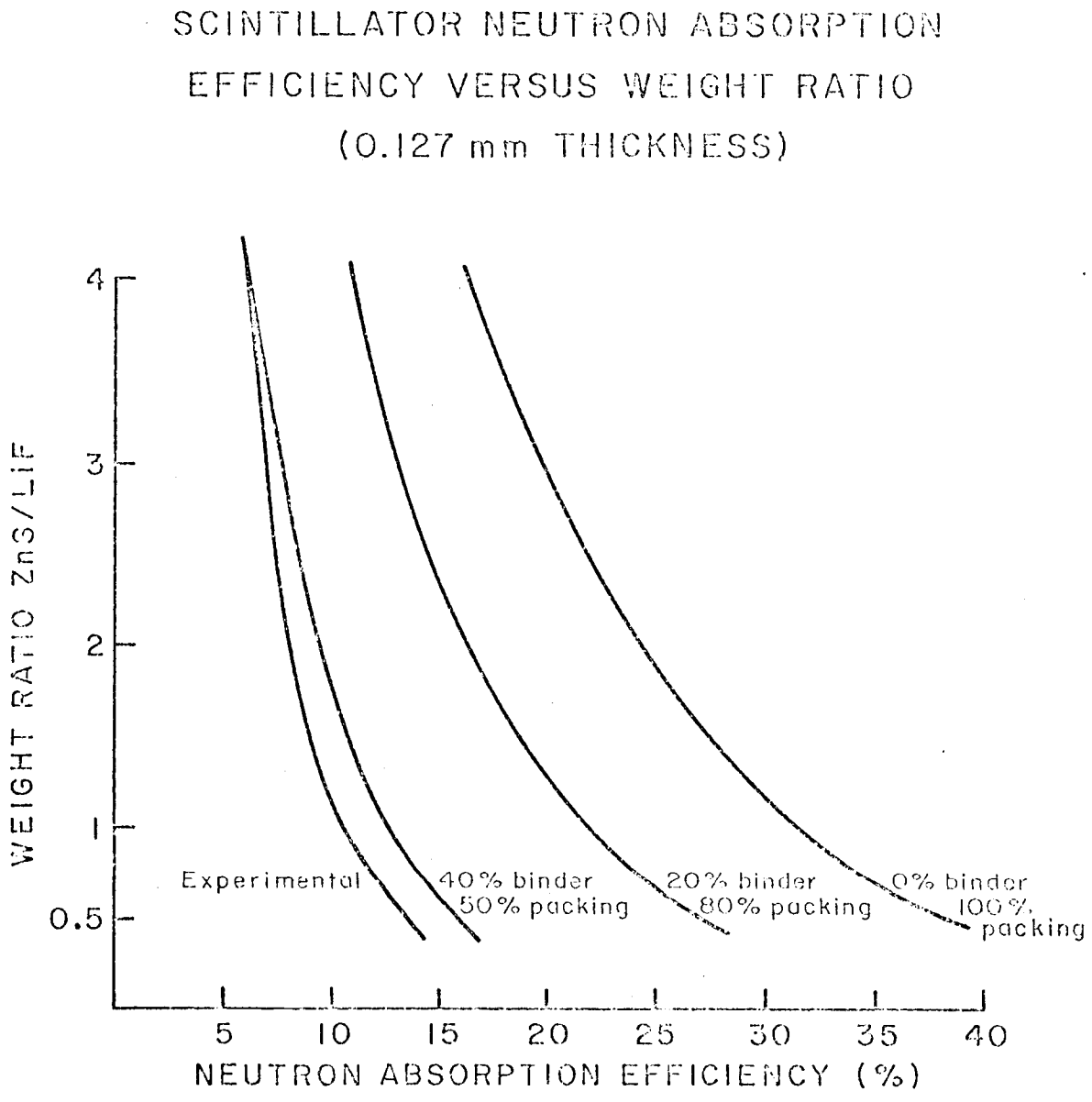
SCINTILLATOR NEUTRON ABSORPTION
EFFICIENCY VERSUS WEIGHT RATIO
(0.127 mm THICKNESS)
WEIGHT RATIO ZnS/LiF
4
3
2
1
0.5
Experimental
40% binder
50% packing
20% binder
80% packing
0% binder
100%
packing
5
10
15
20
25
30
35
40
NEUTRON ABSORPTION EFFICIENCY (%)

Figure 4-9

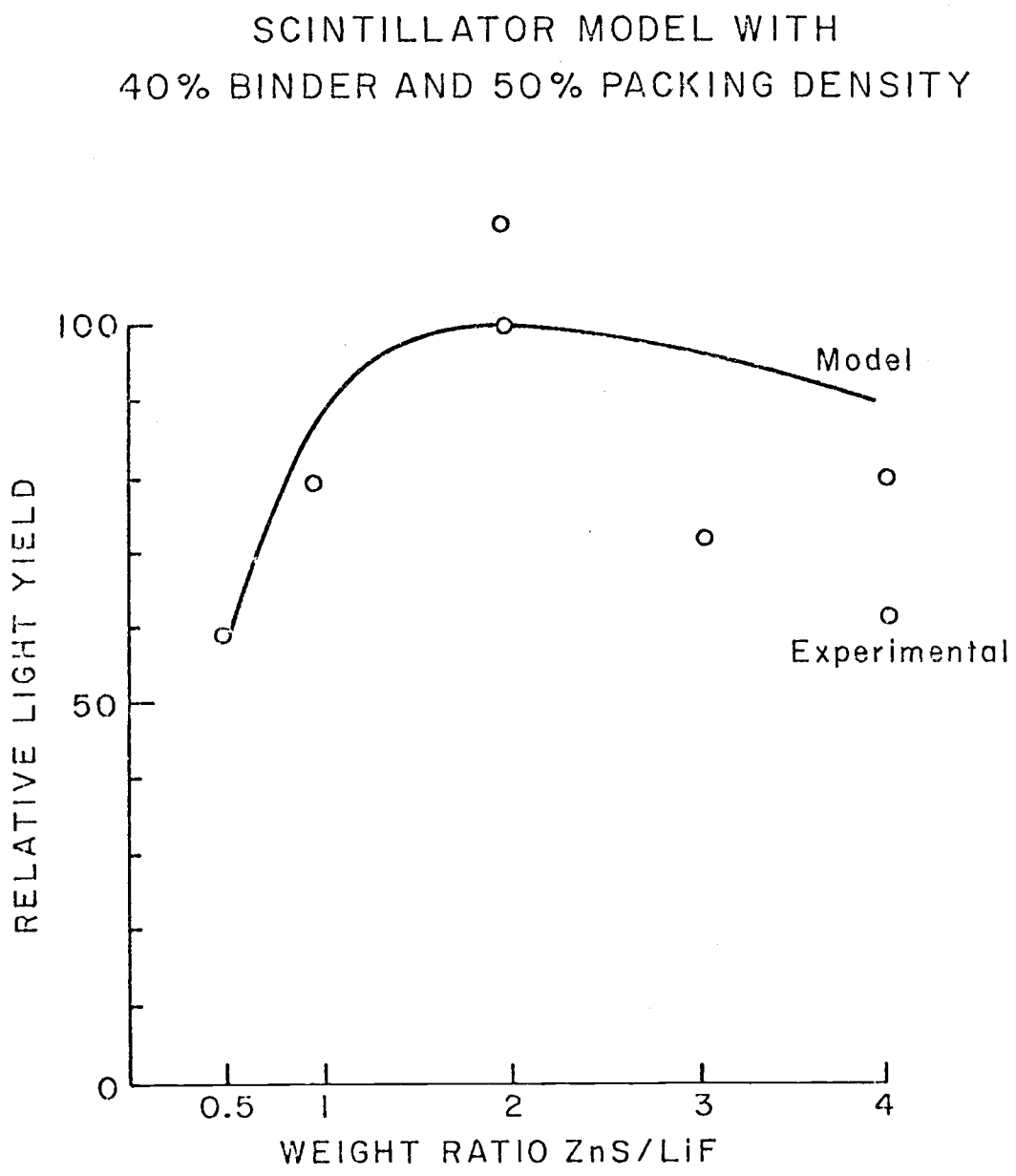
SCINTILLATOR MODEL WITH
40% BINDER AND 50% PACKING DENSITY
RELATIVE LIGHT YIELD
100
50
0
0.5
1
2
3
4
WEIGHT RATIO ZnS/LiF
Model
Experimental

mental scintillators of table 4-3 do not clearly distinguish significant changes in image quality dependent on weight ratio although some evidence is present. The fine differences in VISQI readings may be more a function of film exposure or subjective analysis. The larger differences (greater than 6 sensitivity values) begin to indicate that the 0.5 to 1 and 4 to 1 weight ratio scintillators may not be quite as good as the 1 to 1 and 2 to 1 scintillators for VISQI image quality.

The resolution capability of the scintillator should be a function of thickness and ZnS grain size. Spowart and Wang (67,65) have noted improved resolution with the smaller grains. Thickness effects of a transmission oriented scintillator are somewhat complicated. The light generated at a ZnS grain must escape the scintillator to be registered on film. Since both ZnS and LiF are white powders, they make the scintillator opaque resulting in a limited depth from which light that is generated may escape. Spowart (67) considers the optimum thickness to be 0.25 mm. Thinner samples suffer from inhomogenity of spreading while thick samples (1 mm) give poorer image quality. At OSU, inhomogeneities of construction do not appear until about 0.08 mm thickness such that 0.1 to 0.15 mm scintillators are used routinely. This should allow some resolution improvement although neutron absorption efficiency is sacrificed.

4.11 Light Transmission through LiF-ZnS Scintillators

The loss of resolution with increasing thickness is apparently due to the light generated within the scintillator escaping at large angles

relative to the event location. The transmittance of this blue light through a scintillator is a function of the transmittance through ZnS and LiF grains. The binder material is nearly always clear. Samples of ZnS and sodium silicate and LiF and sodium silicate were constructed on glass slides. The transmittance for various sample thicknesses were measured and the results are plotted in figure 4-10. The data have been fitted to exponential curves such that the light intensity transmitted through ZnS is

$$I = I_o e^{-114t} \qquad (4\text{-}5)$$

where I_o is the initial intensity and t is the thickness in cm. In LiF the exponential fit is not so good but yields

$$I = I_o e^{-61t} \qquad (4\text{-}6).$$

The values of light attenuation coefficients of 114 and 61 cm^{-1}, of course, apply to thicknesses of material mixed with sodium silicate. A scintillator composed of ZnS, LiF and sodium silicate binder should, however, have an attenuation coefficient equal to the sum of the volume ratio of the ZnS and LiF components times their respective coefficients. As a function of weight ratio, the light attenuation coefficients for scintillators of ratios 0.5, 1, 2 and 4 ZnS to LiF are 73.6, 81.4, 90.4 and 98 cm^{-1} respectively. The higher the attenuation coefficient, the less likely that light emitted in all directions will escape at severe angles to cause a loss of resolution.

A computer program "LIGHT", listed in Appendix B, uses a Monte Carlo selection of a neutron interaction in the scintillator to demonstrate this. Light is considered to be emitted in all directions

Figure 4-10

BLUE LIGHT TRANSMISSION IN LiF AND ZnS

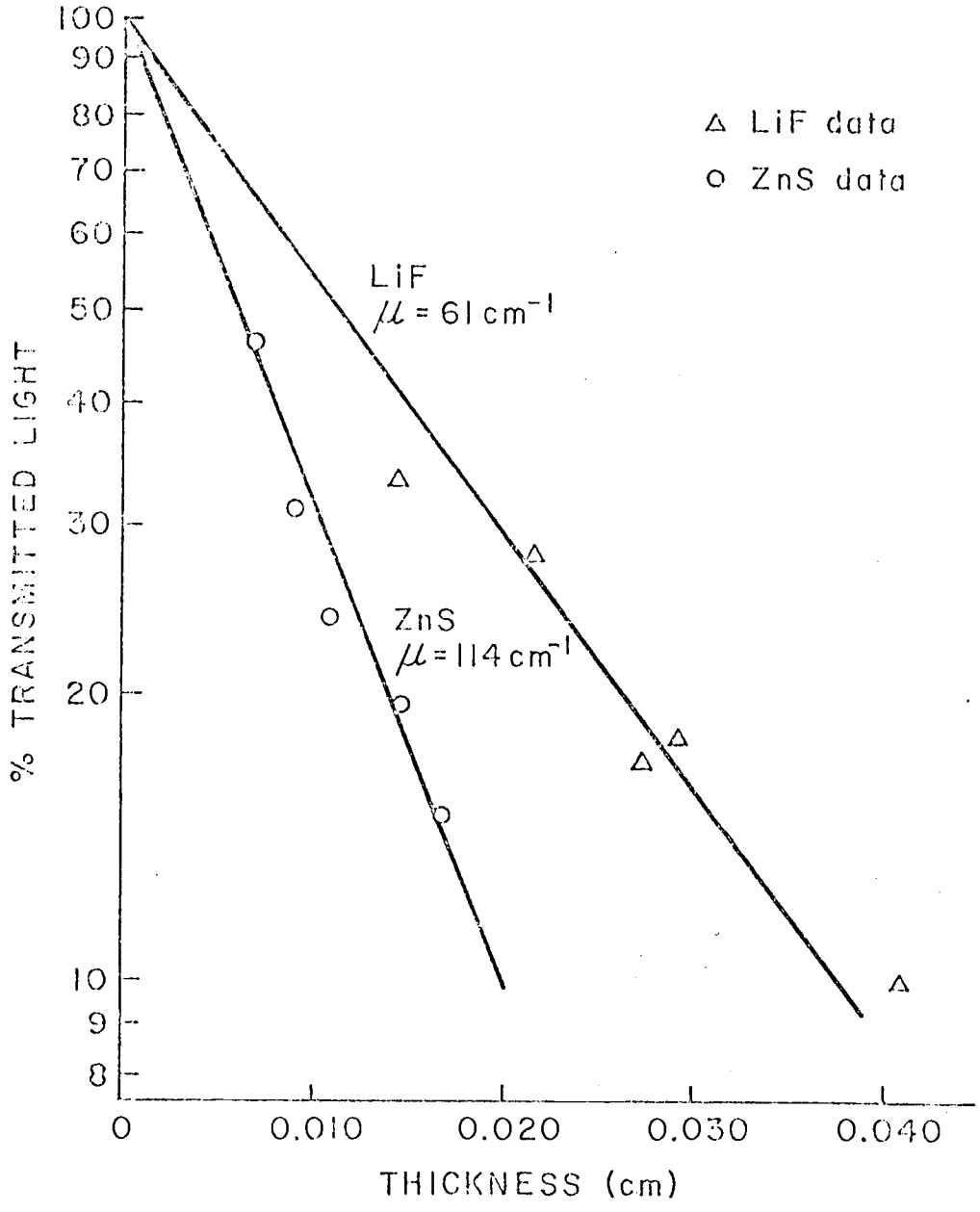

from the point of interaction. This is a simplification as the alpha and triton will spread out this light generation over their combined path lengths of around 30 microns. However, from this simple case in transmission orientation, light transmitted in the forward direction, directly to the scintillator surface and to off axis locations is calculated by $e^{-\mu p}$, where μ is the light attenuation coefficient and p is the path distance to the point on the scintillator surface. Figure 4-11 contains the results showing how the light intensity drops off at the surface with perpendicular distance from the interaction point. The graph is symmetric although curves for 0.127 mm thick scintillators of 0.5, 1, 2 and 4 weight ratios are shown on the right while 0.254 mm and 0.127 mm thick scintillators of 0.5 and 2 weight ratios are shown on the left. The 4 to 1 weight ratio case shows the best resolution characteristics in terms of light intensity distribution as one would obviously expect based on the light transmission coefficient. The 2 to 1 weight ratio case is not severely reduced; however, the 0.5 to 1 case is definitely inferior. The effect of scintillator thickness is indicated by the 0.5 to 1 and 2 to 1 weight ratio cases where a 0.254 mm scintillator is notably inferior to a 0.127 mm scintillator. The 0.254 mm, 2/1 weight ratio scintillator is shown to have slightly better resolution capability than the 0.5/1, 0.127 mm scintillator. Comparing these results with experimental data in table 4-3 from the VISQI some similar trends are present with the notable exception of the experimental 4 to 1 weight ratio scintillators. These OSU constructed 4/1 scintillators clearly do not appear to exhibit this predicted superior resolution capability.

Figure 4-11

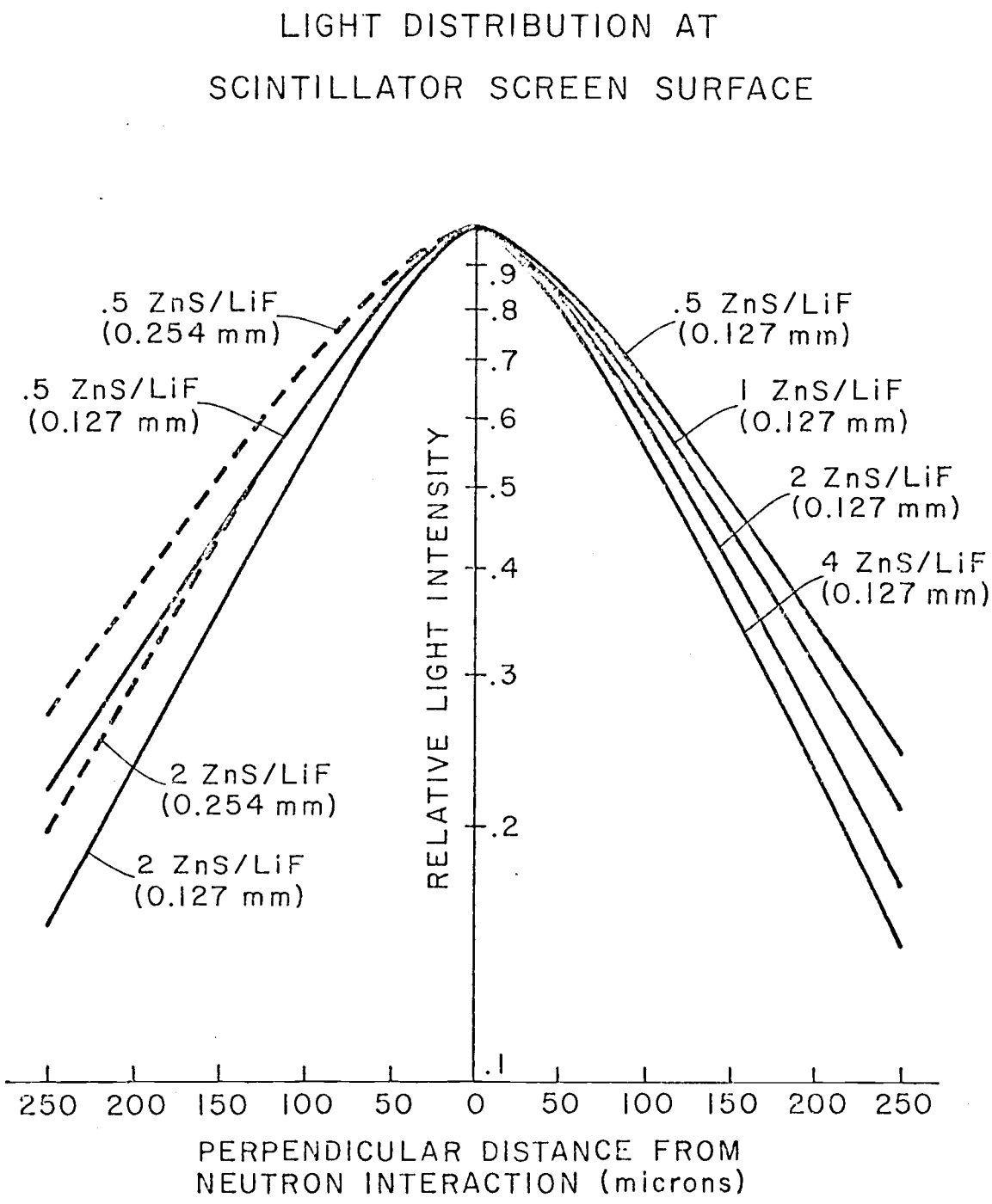
LIGHT DISTRIBUTION AT
SCINTILLATOR SCREEN SURFACE
.5 ZnS/LiF
(0.254 mm)
.5 ZnS/LiF
(0.127 mm)
2 ZnS/LiF
(0.254 mm)
2 ZnS/LiF
(0.127 mm)
.5 ZnS/LiF
(0.127 mm)
1 ZnS/LiF
(0.127 mm)
2 ZnS/LiF
(0.127 mm)
4 ZnS/LiF
(0.127 mm)
RELATIVE LIGHT INTENSITY
.9
.8
.7
.6
.5
.4
.3
.2
.1
250 200 150 100 50 0 50 100 150 200 250
PERPENDICULAR DISTANCE FROM
NEUTRON INTERACTION (microns)

4.12 Statistical Effects

Returning to the scintillator computer model, an additional bit of information may be extracted. When the neutron initiates the reaction, energy is given to the triton and alpha and the particles generate light along their paths, the total light signal is not necessarily of the same magnitude each time. This means that some neutrons will yield more light than others. As a result, the scintillator light signal will have noise induced on it due to the statistical effect of whether the neutrons generate a large or small signal. The scintillator model computes the amount of energy each random neutron event deposits in ZnS. Over many histories, the distribution of the fraction of the 4.78 MeV released per neutron in the Li-6 interaction may be determined. Figure 4-12 contains the results for several weight ratios of ZnS to LiF in the scintillator model with 0.127 mm thickness, 40% binder and 50% packing. The energy deposited in ZnS for each event has been blocked into fractional portions of the 4.78 MeV of 0 to 10%, 10% to 20%, 20% to 30%, etc., and the number of histories falling into the appropriate blocks summed. The histogram indicates that at higher weight ratios there is greater spread in the amount of light any one neutron may generate. The smaller weight ratio scintillators have a lower amount of energy deposited but are more consistant about the magnitude of the signal that a neutron generates. This indicates that if neutron statistics are at all in question in imaging, a lower weight ratio scintillator would be preferred to reduce noise in the image. The subject of neutron statistics in imaging is discussed in Chapter VI.

Figure 4-12

HISTOGRAM OF THE NUMBER OF HISTORIES VERSUS ENERGY IN ZnS GRAINS AS A FUNCTION OF WEIGHT RATIO

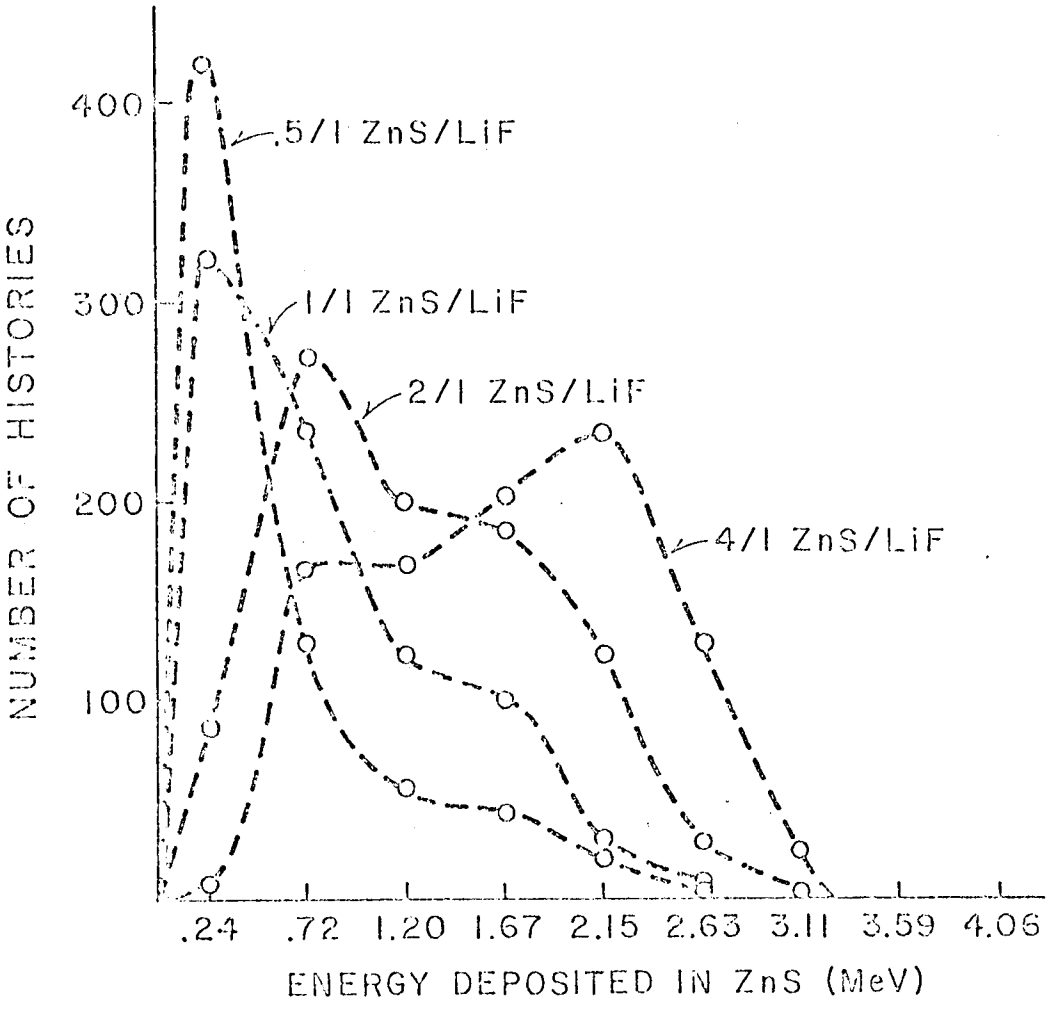

4.12 Conclusions

The scintillator analysis shows that the LiF-ZnS scintillator is presently the type of scintillator best suited for high speed motion neutron radiography work in the range of 2000 to 10,000 frames/second. At lower frame rates rare earth scintillators may be better for their superior image quality. At higher frame rates glass scintillators are necessary for their rapid light decay characteristics but require much greater light amplification.

Studies of the optimum construction for the LiF-ZnS scintillators generate some interesting observations. A scintillator of 2/1, ZnS to LiF weight ratio, 0.127 mm thickness, constructed at OSU has been found to be one of the very best scintillators available. This is in agreement with the optimum light yield prediction for such a weight ratio scintillator by a computer simulation of the scintillator operation. Other authors have found slightly higher weight ratios to be optimum using their construction methods and binders. The thin scintillator (0.127 mm) is preferred for resolution capability. Calculations appear to indicate a slight advantage of higher ZnS to LiF weight ratios for improving the resolution; however the higher weight ratios also appear to increase the statistical fluctuation of the light yield per neutron event. Thus, trade offs exist in the selection of the ZnS to LiF ratio for the scintillator. Further, in practice the construction technique involves some measure of art, as batch to batch variation can be significant.

Although 2/1, ZnS to LiF scintillators, constructed at OSU using sodium silicate binder and the settling particle technique, are superior it would be improper to say this is always the best. Other construction techniques or binders may very well influence the scintillator operation in such away as to offset the results slightly. The relative quality of the scintillator remains to some degree subjective and a scintillator should be chosen for a specific operation by a comparison of the effectiveness of the available scintillator screens to provide the most desirable result.

V. SYSTEM ANALYSIS

5.1 Introduction

Considering that the high speed motion neutron radiography system consists of a number of linked imaging components it is desirable to determine the individual effects of each component on the final image. Conventional image quality analysis using test objects (such as the previously introduced VISQI) do not allow a useful break down of the contribution of each imaging component. Even if each component could be individually examined with the object, the figure of merit provided by these test objects is of relative value and cannot be applied in any mathematical sense for determining the effects of various combinations of components. Further, the comparison of test objects in radiographs is a function of the observer's visual acuity and possibly the film exposure. To overcome these disadvantages, modulation transfer function analysis may be performed. This involves the Fourier transformation of the imaging system's one dimensional line spread function into spatial frequencies and allows evaluation of individual as well as combined effects of components by the commutative properties.

5.2 Modulation Transfer Function

The modulation transfer function (MTF) is a well known technique for image quality analysis in optics and photography (85-88). It is routinely used for characterizing lenses and is becoming more and more standard for photographic film (89-91). Application to radiography

has been relatively slow due in part to the difficulty of a suitable method of measurement. However, MTF measurements have been performed for x-radiographic systems (92-96). Neutron radiography has also seen some experimental application of the MTF in recent years (97-100).

The modulation transfer function stems from the relation of the output signal to the input signal of a system. If the input object signal has a sinusoidal distribution, then the output image will also have a sinusoidal distribution and the "modulation" or sine wave response of the transferred information is the ratio of the amplitude in the image to the amplitude in the object (87,96). As the frequency of the sinusoidal pattern changes, the modulation will change such that

$$M(\omega) = \frac{|I(\omega)|}{|O(\omega)|} \qquad (5\text{-}1)$$

where $M(\omega)$ is the modulation as a function of frequency ω, $I(\omega)$ is the image amplitude and $O(\omega)$ is the object amplitude. A plot of $M(\omega)$ versus frequency is the MTF. The MTF may thus be measured directly with an appropriate test object which provides a sinusoidal variation of the signal. For radiography this has been prohibitive. To overcome the sine wave test object problem a square wave pattern (bar pattern) followed by conversion of the square wave response to sine wave response could be used (101). This technique has been applied to neutron radiography and while useful, still involves limitations due to the test object construction (93). Another approach to determining the MTF of radiographic systems involves the construction of special apparatus which will intersect the signal and vary the intensity in a sinusoidal manner (96). Although workable, this technique does possess

certain drawbacks with the physical size and operation of the equipment. To avoid these problems a more mathematically based approach may be taken for finding the MTF.

When a geometric point of radiation is imaged the result is no longer a point but is a mound, spread out due to geometry, scatter, screens, film, etc. The same applies for a fine line of radiation. These effects are called the point spread function and line spread function shown in figure 5-1. The line spread function having only one dimension is simpler to work with than the point spread function and therefore is the only one considered further. The line spread function, given by A(x) where x is the spatial dimension, may be used as the building block of images. The intensity of an image at a point ξ is given by

$$E(\xi) = \int_{-\infty}^{\infty} A(x)G(\xi-x)dx \tag{5-2}$$

where $G(\xi-x)$ is the object function being radiographed. This operation is a convolution. If G(x) in object space is a sinusoidal object function,

$$G(x) = b_o + b_1 \cos 2\pi\omega x \tag{5-3}$$

where ω is spatial frequency, b_o and b_1 are constants, then equation 5-2 becomes

$$E(\xi) = b_o \int_{-\infty}^{\infty} A(x)dx + b_1 \int_{-\infty}^{\infty} A(x)\cos 2\pi\omega(\xi-x)dx \tag{5-4}$$

$$E(\xi) = b_o \int_{-\infty}^{\infty} A(x)dx + b_1 \int_{-\infty}^{\infty} A(x)\cos 2\pi\omega\xi \cos 2\pi\omega x dx +$$

$$b_1 \int_{-\infty}^{\infty} A(x)\sin 2\pi\omega\xi \sin 2\pi\omega x dx \tag{5-5}.$$

Figure 5-1

POINT SPREAD FUNCTION

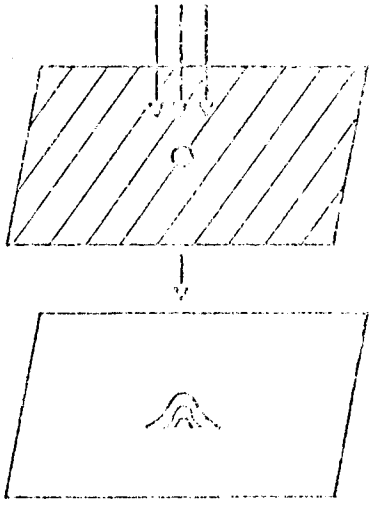

LINE SPREAD FUNCTION

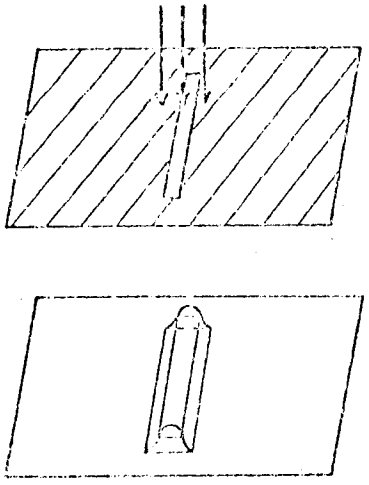

Introducing a normalized integral

$$F_c(\omega) = \frac{\int_{-\infty}^{\infty} A(x)\cos 2\pi\omega x\,dx}{\int_{-\infty}^{\infty} A(x)\,dx} \tag{5-6}$$

and

$$F_s(\omega) = \frac{\int_{-\infty}^{\infty} A(x)\sin 2\pi\omega x\,dx}{\int_{-\infty}^{\infty} A(x)\,dx} \tag{5-7},$$

equation 5-5 in normalized form becomes

$$E(\xi) = b_o + b_1 F_c(\omega)\cos 2\pi\omega\xi + b_1 F_s(\omega)\sin 2\pi\omega\xi \tag{5-8}$$

where $F_c(\omega)$ and $F_s(\omega)$ are the normalized cosine and sine Fourier transformations. Defining

$$|F(\omega)| = \{[F_c(\omega)]^2 + [F_s(\omega)]^2\}^{\frac{1}{2}} \tag{5-9}$$

equation 5-8 becomes

$$E(\xi) = b_o + b_1 |F(\omega)| \cos(2\pi\omega x - \phi) \tag{5-10}$$

where $\phi = \tan^{-1}\frac{F_s}{F_c}$.

The image function of equation 5-10 may be compared with the object function of equation 5-3. It is seen that the modulation in the image is $|F(\omega)|$ times as great as the modulation in the object. Thus the modulation transfer function is given by $M(\omega) = |F(\omega)|$ which is the magnitude of the normalized Fourier transformation of the line spread function. There is also a phase shift, ϕ, between the object and image because the two may not have exact geometric similarity. This is particularly true in optical lenses where the line spread function is not necessarily symmetrical off axis. The optical transfer function (OTF) is then given by $O(\omega) = M(\omega)e^{i\phi(\omega)}$. For radiography

the phase change need not be considered as emulsion grains are disposed at random so there is no preferred direction (87).

In equation 5-2 the image intensity was found to be related to the object function by a convolution. In a system composed of several components the final image would be series of convolutions. Using the modulation transfer function however the modulation in the final image is simply the multiplication of the modulation of each component;

$$M(\omega) = M_1(\omega) \times M_2(\omega) \times M_3(\omega) \times \ldots\ldots \qquad (5\text{-}11)$$

where M_1, M_2, M_3, etc. are the component modulation transfer function terms.

5.3 Measuring the MTF

The MTF is now capable of being measured, without the construction of a sinusoidal test object, by use of the Fourier transformation of the line spread function. This has been done in x radiography (92-94). A thin slit on the order of 10 microns is radiographed and scanned by a microdensitometer. The resulting film density trace is the line spread function and numerical Fourier transformation will generate the MTF. Of course, theoretically, the microdensitometer must also have an infinitely narrow scanning slit. Provided the system being studied is relatively poor the finite value of the slit does not affect the results seriously. It is possible though to correct the results by obtaining a MTF for the slit and densitometer and dividing these components out of the system.

Another approach is to consider the radiograph of a knife edge. In this case the object function is a step function having a value of

0 at $x \leq 0$ and a value of 1 at $x \geq 0$. The image function, called the edge spread function or unsharpness curve, S(x), is simply an integration of the line spread function, A(x), times the step function. From figure 5-2 it is seen that

$$S(x) = \int_0^{\infty} A(x)dx \qquad (5\text{-}12).$$

Then the line spread function is simply

$$A(x) = \frac{dS(x)}{dx} \qquad (5\text{-}13).$$

The MTF is found by a microdensitometer scan of the radiograph to obtain the edge spread function which is numerically differentiated and Fourier transformed. This technique has been employed for MTF analysis in neutron radiography (97,98,100). The advantage is that the object, a sharp edge of gadolinium or cadmium, is easy to obtain. A very fine line object consisting of finely spaced gadolinium edges would be more difficult. The disadvantage is that this technique involves the differentiation of numerical data which can be a source for error.

The edge technique is also used in film and optical system analysis (88,102,103) and has been found to have as good or better precision for MTF analysis than that obtained with sinusoidal objects (104). Edge scans though are rarely perfectly shaped but contain grain noise and other film nonuniformities such as adjacency effects due to development. Edge spread data often requires smoothing to eliminate the problems of differentiating and transforming an edge containing noise. Hand smoothing can be performed and is often used when a limited number of scans are to be done. For more automated operations, sophisticated

Figure 5-2

EDGE SPREAD FUNCTION

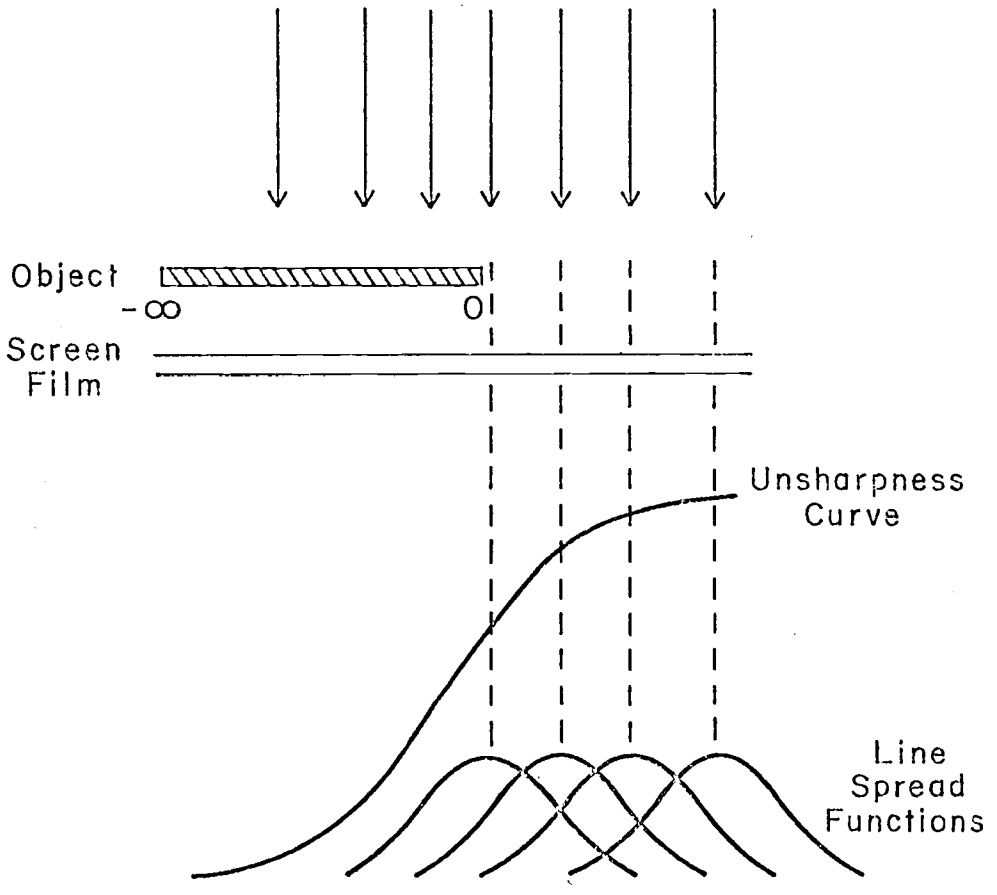

mathematical fitting routines can be developed to aid in accounting for these difficulties (105-107). In systems with relatively poor transfer functions, such as radiography, the high frequency distortion due to noise may not significantly influence the lower frequency of the edge scan such that the MTF may be reasonably measured with the direct application of the edge spread technique to the data.

Modulation transfer function analysis requires that the systems be linear. This is not normally the case for films whose response to exposure as shown by their characteristic curves may be nonlinear. Film density corrections in the data must be made to convert the data points to exposure values or the film may be exposed over a region of relatively linear response, particularly if a low contrast object is used. X-ray films typically have a linear response while photographic films exhibit a logarithmic response to exposure over the medium range of film density.

5.4 Numerical Technique for MTF Measurement

Experimental determination of the MTF using the edge spread function technique may be performed by scanning the sharp edge radiograph with a microdensitometer, numerically differentiating the data and numerically taking the Fourier transform. Theoretically, any mathematically sound method of numerical differentiation and Fourier transformation should work successfully. A conventional technique consists of smoothing the microdensitometer scan and differentiating the data to get the line spread function. This may or may not be symmetric depending on the original edge scan. Although it is

expected that the line spread function should be symmetric, in practice the data from the edge scan often is not. The line spread function peak then is found and any asymmetry removed by averaging. By using the line spread peak as the origin a cosine Fourier transformation need only be used to generate the MTF; the sine transform goes to zero due to symmetry.

A somewhat different routine has been written to generate MTF's for the high speed motion neutron radiography study. A cubic spline interpolation of the smoothed edge scan data is used from which a continuous point to point first derivative in the form of an interpolating polynomial is obtained (108,109). The Fourier transform is then taken directly from the interpolating polynomial. The cubic spline interpolation of the data is fundamentally based on having continuous second derivatives, making cubic spline interpolation the smoothest curve. Alger (100) advocated the cubic spline in his MTF work. From the digital edge data the computer first calculates second derivative values at the data points. These are generated by a tridiagonal matrix solution based on the equation

$$y''_{i-1} + 4y''_i + y''_{i+1} = 6\left(\frac{y_{i+1} - 2y_i + y_{i-1}}{h^2}\right) \qquad (5\text{-}14)$$

where y_i are the values of the data points, y''_i are the second derivatives and h is the point spacing. The first derivative of the edge (the line spread function) may be obtained in the form of an interpolating polynomial based on these initial and second derivative values:

$$f'(x) = \frac{y''_i}{6h}(-3x^2 + 6x_{i+1}x - 3x_{i+1}^2) +$$

$$\frac{y''_{i+1}}{h}(3x^2 - 6x_i x + 3x_i^2) +$$

$$\frac{y_{i+1}}{h} - \frac{hy''_{i+1}}{6} - \frac{y_i}{h} + \frac{hy''_i}{6} \qquad (5\text{-}15)$$

where $f'(x)$ is the first derivative of the edge spread function and again y_i is the value of the data point i, y''_i is the second derivative of the data point i (solved for from the tridiagonal matrix formula), x_i is the position of the point i, x_{i+1} is the position of the point i+1 and h is the spacing between x_{i+1} and x_i. This entire polynomial which represents the line spread function may be used in the Fourier transformation for the MTF:

$$F_c(\omega) = \sum_{1}^{n} \int_{x_i}^{x_{i+1}} f'(x)\cos 2\pi\omega x\,dx \qquad (5\text{-}16)$$

$$F_s(\omega) = \sum_{1}^{n} \int_{x_i}^{x_{i+1}} f'(x)\sin 2\pi\omega x\,dx \qquad (5\text{-}17).$$

Evaluation of these integrals results in the algorithm to be used in the MTF computer routine:

$$F_c(\omega) = \sum_{1}^{n} \{ \frac{y''_{i+1}}{\omega^2}\cos 2\pi\omega x_{i+1} - \frac{y''_i}{\omega^2}\cos 2\pi\omega x_i +$$

$$[\frac{y''_{i+1}h}{2\omega} + \frac{y_{i+1}-y_i}{h\omega} + (\frac{1}{h\omega^3} + \frac{h}{6\omega})(y''_i - y''_{i+1})]\sin 2\pi\omega x_{i+1} +$$

$$[\frac{y''_i h}{2\omega} + \frac{y_i - y_{i+1}}{h\omega} + (\frac{1}{h\omega^3} + \frac{h}{6\omega})(y''_{i+1} - y''_i)]\sin 2\pi\omega x_i \} \qquad (5\text{-}18)$$

$$F_s(\omega) = \sum_{1}^{n} \{ \frac{y''_{i+1}}{\omega^2} \sin 2\pi\omega x_{i+1} - \frac{y''_i}{\omega^2} \sin 2\pi\omega x_i +$$

$$[\frac{-y''_{i+1} h}{2\omega} + \frac{y_i - y_{i+1}}{h\omega} + (\frac{1}{h\omega^3} + \frac{h}{6\omega})(y''_{i+1} - y''_i)] \cos 2\pi\omega x_{i+1} +$$

$$[\frac{-y''_i h}{2\omega} + \frac{y_{i+1} - y_i}{h\omega} + (\frac{1}{h\omega^3} + \frac{h}{6\omega})(y''_i - y''_{i+1})] \cos 2\pi\omega x_i \; \}$$

(5-19).

The MTF of course is the square root of the sum of the squares of F_c and F_s.

The listing of the complete computer routine is given in Appendix C. Input consists of the number of data points, the spacing and their values. The output contains the initial values, line spread function values calculated as a check from equation 5-15 and modulation transfer function factors at various frequency values from 0.1 to 50. lines/mm. The advantage of this technique is that once the edge data is input to the computer routine no manipulation of the line spread function is required. The origin also need not be specified. Asymmetry of the edge is of course carried through the MTF analysis.

This MTF analysis routine, using the Fourier transformation algorithms of equations 5-18 and 5-19, has been tested using functions with known transforms yielding excellent results. Table 5-1 shows the results for the function $-e^{-x}$ and the error function (erf(x)). The transformation of e^{-x} calculated by first taking the derivative of $-e^{-x}$ numerically is correct to within < 1%. The error function has the same shape as the edge spread function with a derivative equal to e^{-x^2}. The computer routine calculated the derivatives to

Table 5-1

TEST CASES FOR THE MODULATION TRANSFER FUNCTION PROGRAM

Function: $-e^{-x}$

Input 51 data points with h = 0.2, derivative = e^{-x}

Frequency (ω)	F_c			F_s		
	program	exact	% error	program	exact	% error
.1	.716958	.716957	0.000	.450578	.450477	0.022
.2	.387788	.387727	0.016	.487454	.487232	0.046
.3	.219683	.219633	0.023	.414396	.413998	-0.009
.6	.065879	.065737	0.217	.248592	.247821	0.311
1.0	.024477	.024705	-0.921	.156149	.155223	0.596

Function: erf(x)

Input 30 data points with h = 0.1, derivative = e^{-x^2}

Position	Derivative			Frequency	F_c		
(x)	program	exact	% error	(ω)	program	exact	% error
0	1.1289	1.12838	0.046	.1	.906022	.906018	0.000
.5	.8790	.87878	0.025	.2	.673813	.673825	-0.002
1.0	.4152	.41511	0.022	.3	.411356	.411369	-0.003
1.5	.1184	.11893	-0.446	.4	.205192	.206153	0.019
2.0	.0205	.02067	-0.808	.6	.028616	.028637	-0.073

within 0.8% and the cosine transform to within 0.08% using only 30 data points. Results for points other than in the tail region are nearly exact.

5.5 Experimental Results of MTF Measurements

The MTF calculations using the edge spread function data have been applied to the high speed motion neutron radiography system by radiographing a sharp edge, scanning the radiographic edge with a microdensitometer and performing numerical data manipulation in the computer routine developed. A thin piece of gadolinium, 0.03 mm thick, having a sharp edge was radiographed with a LiF-ZnS scintillator, the image intensifier, high speed camera at 5000 frames/second and RAR 2498 film. The 16 mm film was scanned on a Grant Measuring Engine microdensitometer yielding the edge spread function data of figure 5-3. A smooth curve (drawn by hand) through the data points alleviates the significant grain noise of the scintillator in the data.

Similarly, the scintillator, image intensifier, high speed camera and the RAR 2498 film were evaluated for their edge spread functions. The scintillator was placed on RAR 2498 film and a radiograph taken of the Gd edge. The image intensifier, high speed camera and film were evaluated by the edge of a razor blade photographed by each. The razor blade edge was placed in contact with the image intensifier input faceplate. The output of the image intensifier was recorded by a 35 mm Pentax camera using RAR 2498 film. A photograph of the razor blade edge, painted black for contrast, was taken

Figure 5-3

EDGE SPREAD FUNCTION FOR A HIGH SPEED MOTION NEUTRON RADIOGRAPH

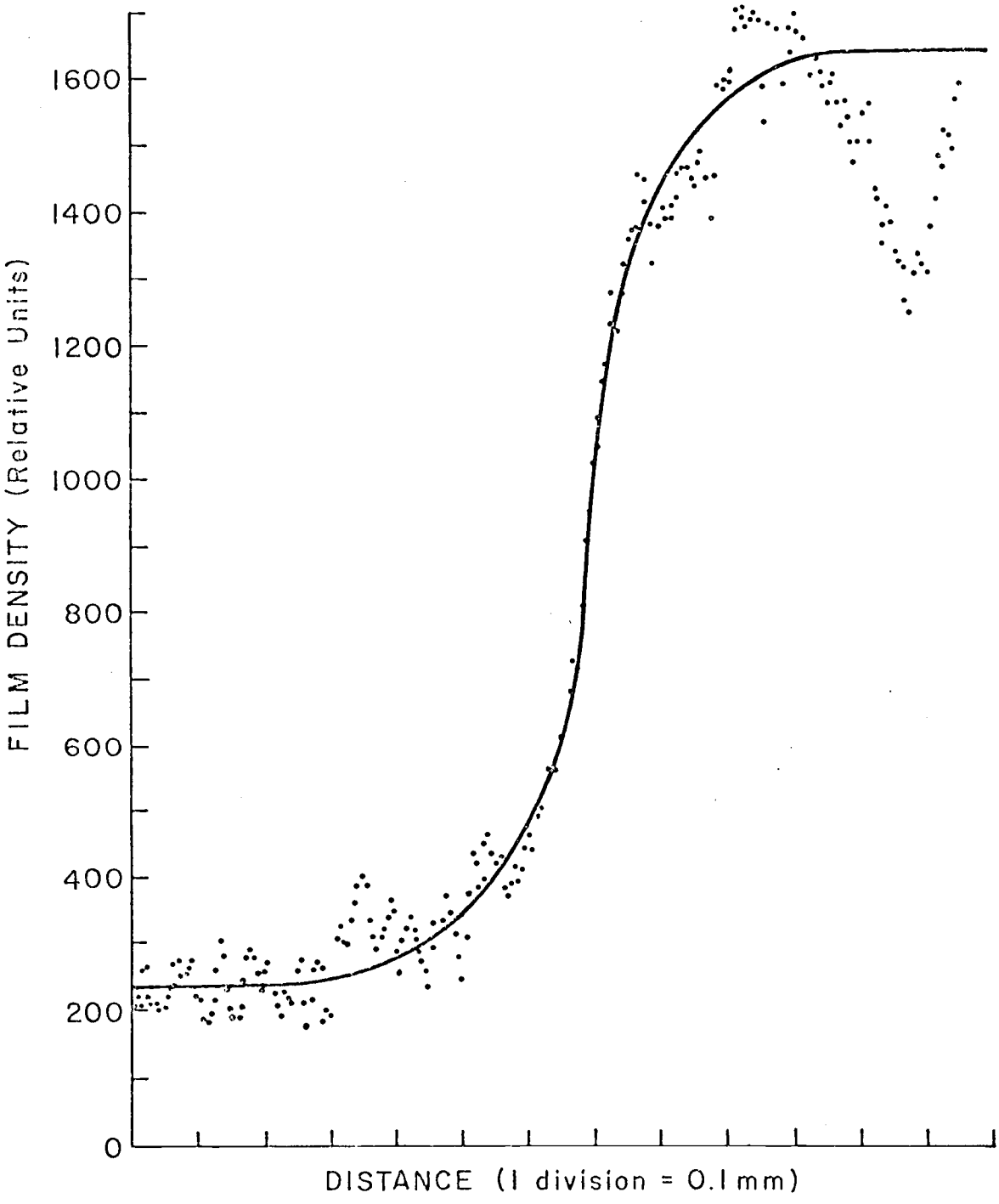

by the high speed camera and also by the 35 mm Pentax camera to determine the edge spread functions for each. Finally, a strip of RAR 2498 film was exposed directly in contact with the razor blade to obtain an edge spread function. Each exposure was scanned with the microdensitometer using a slit width that was very small compared to the edge spread to avoid densitometer broadening of the true edge. This slit determination was easily made by the densitometer's slit measuring system on an oscilloscope screen. Slit widths of 10 microns or less were employed. The results of the MTF analysis of the edge scans are given in figure 5-4.

Some interesting information is provided by the MTF analysis. Surprizingly, the quality of the scintillator screen in contact with film is indicated to be inferior to the high speed motion system. This is in violation of the expected MTF response that each subsystem multiplicatively contributes to the final total system MTF curve and points out a nonlinearity in the high speed imaging system. Apparently, the use of the scintillator with the image intensifier improves the resolution capability. This is born out by a comparison of VISQI radiographs taken with the scintillator and film and by the scintillator, image intensifier and 35 mm Pentax camera. The image intensifier method results in distinctly superior image detail visibility. With the VISQI radiographed using the scintillator, image intensifier and high speed camera, the detail visibility improvement is not obvious as in the MTF curves. The fine fiber optics input of the intensifier accepts only parallel light rays such that light emitted at severe angles from the scintillator surface will not degrade the

Figure 5-4

MODULATION TRANSFER FUNCTIONS FOR THE HIGH SPEED MOTION NEUTRON RADIOGRAPHY COMPONENTS

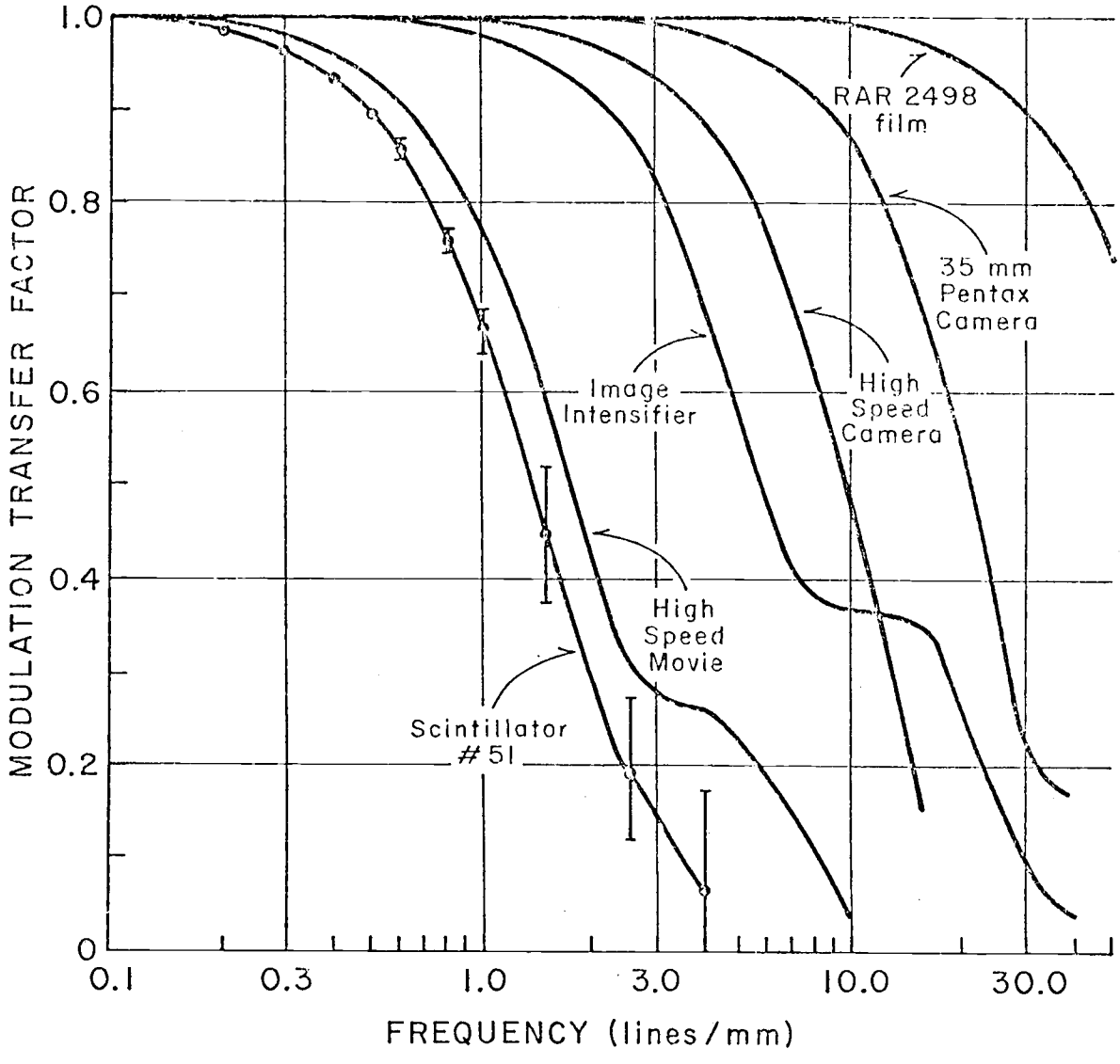

quality as it could in the case of direct contact with film. This suggests that standard scintillator screen radiography could be improved with a fiber optics light pipe between the scintillator and film. The use of the camera focused on the image intensifier output may also be helpful. The focusing directs the light to specific locations on the film for recording and can be superior to a direct contact situation. There may be some advantage to focusing a camera on the scintillator screen itself rather than direct film contact although exposure times will suffer considerably.

The other curves of figure 5-4 show the relative ability of the intensifier, camera and film. The image intensifier is markedly superior to the scintillator and inferior to the high speed camera. At higher frequencies however the intensifier shows some improvement over the high speed camera. The 35 mm Pentax camera with RAR 2498 film is included. This camera has a better MTF curve than the high speed camera. The loss of quality in the high speed camera is due to the rotating prism and optical system which is necessary for the high speed capability. As with most systems, as speed is increased, the quality suffers to some degree. The film MTF for RAR 2498 developed at 20°C (68°F) is quite good and is slightly better than the Kodak MTF curve for 35°C (95°F) processing.

The precision of the measurements is indicated in the MTF curve for scintillator #51. One sigma error bars for 3 independent readings are given. The degree of deviation is disappointing but appears irreconcilable due to the scintillator grain noise in the edge spread data. Deviations though of $\pm$ 0.05 in MTF factors are not uncommon

in other efforts (105) and thus the results are not too inaccurate considering only three runs are used. Certainly where it is possible, a much larger number of scans should be made across the edge in order to reduce the error bands. If the entire edge spread data set containing noise is input to the computer program, a MTF will be generated that has a response value less than 1.0 at low frequency and then with higher frequency begins to fall in along the curves shown. The effect of never reaching a value of 1.0 in modulation transfer factor at low frequency is due to the scintillator grain noise. For the higher quality image intensifier, high speed camera, 35 mm camera and film the noise of the scintillator is not present and the MTF obtained directly from the data without hand smoothing and redigitizing but with appropriate normalization of the tail regions is not too far different from the results shown.

The MTF may also be applied to general neutron radiography techniques. Figure 5-5 contains the MTF curves for gadolinium, dysprosium and indium foils recorded on Kodak Single Emulsion Type R (SR) x-ray film. The gadolinium foil is 0.033 mm thick. Three independent measurements were taken to establish the precision as shown by the one sigma error bars. The dysprosium foil is 0.127 mm thick and does not show as great a resolution capability as the Gd. The indium foil (0.254 mm thick) is the poorest of the three. Three scintillator screens are shown in figure 5-6. The curves are nearly identical at low frequency but at higher frequency the Apex Research gadolinium oxysulphide screen demonstrates a resolving capability out past 10 lines/mm. Scintillator #51 shows a slightly superior response to the

Figure 5-5

MODULATION TRANSFER FUNCTIONS
FOR NEUTRON RADIOGRAPHY FOILS

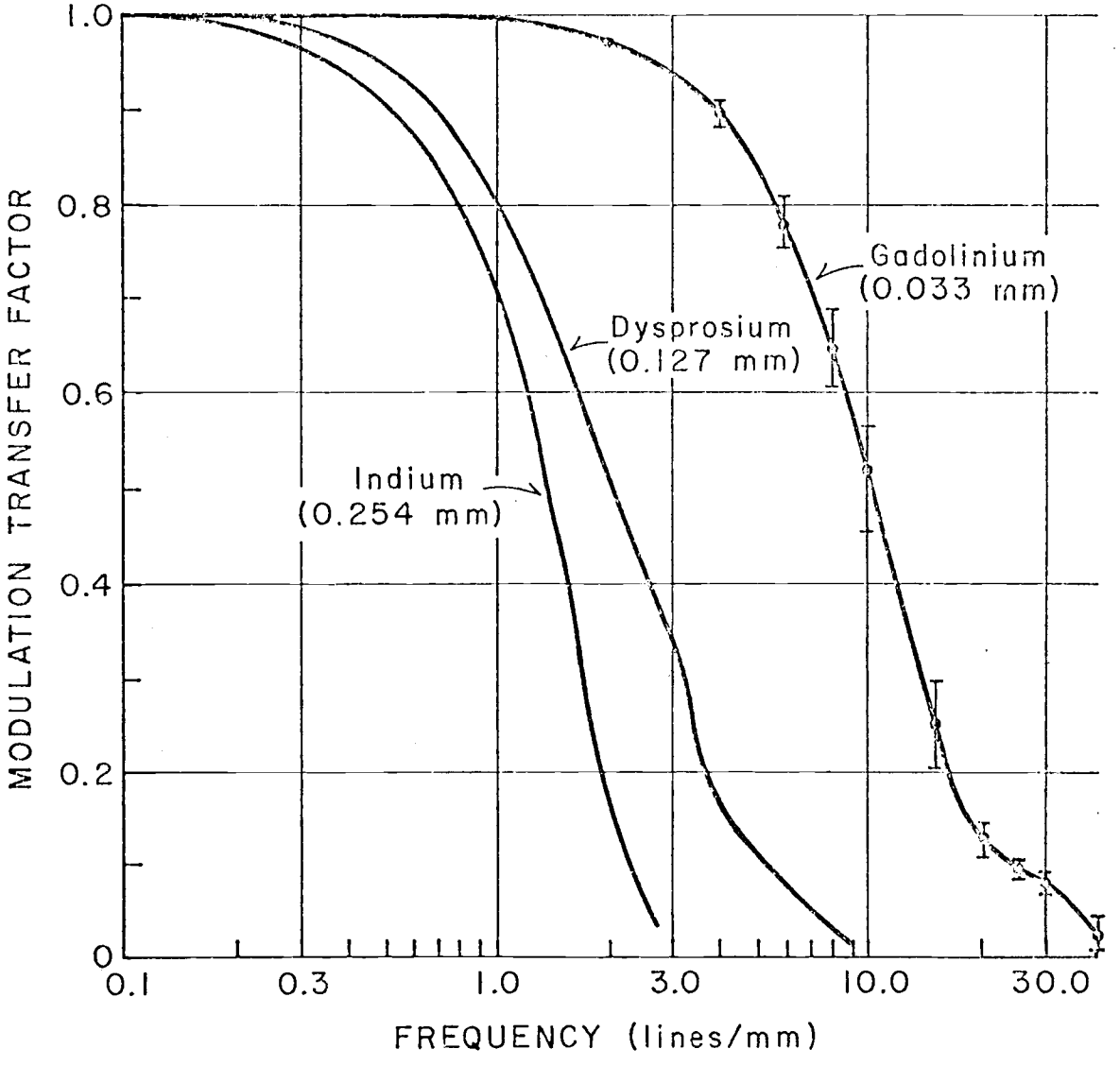

Figure 5-6

MODULATION TRANSFER FUNCTIONS
FOR SCINTILLATOR SCREENS

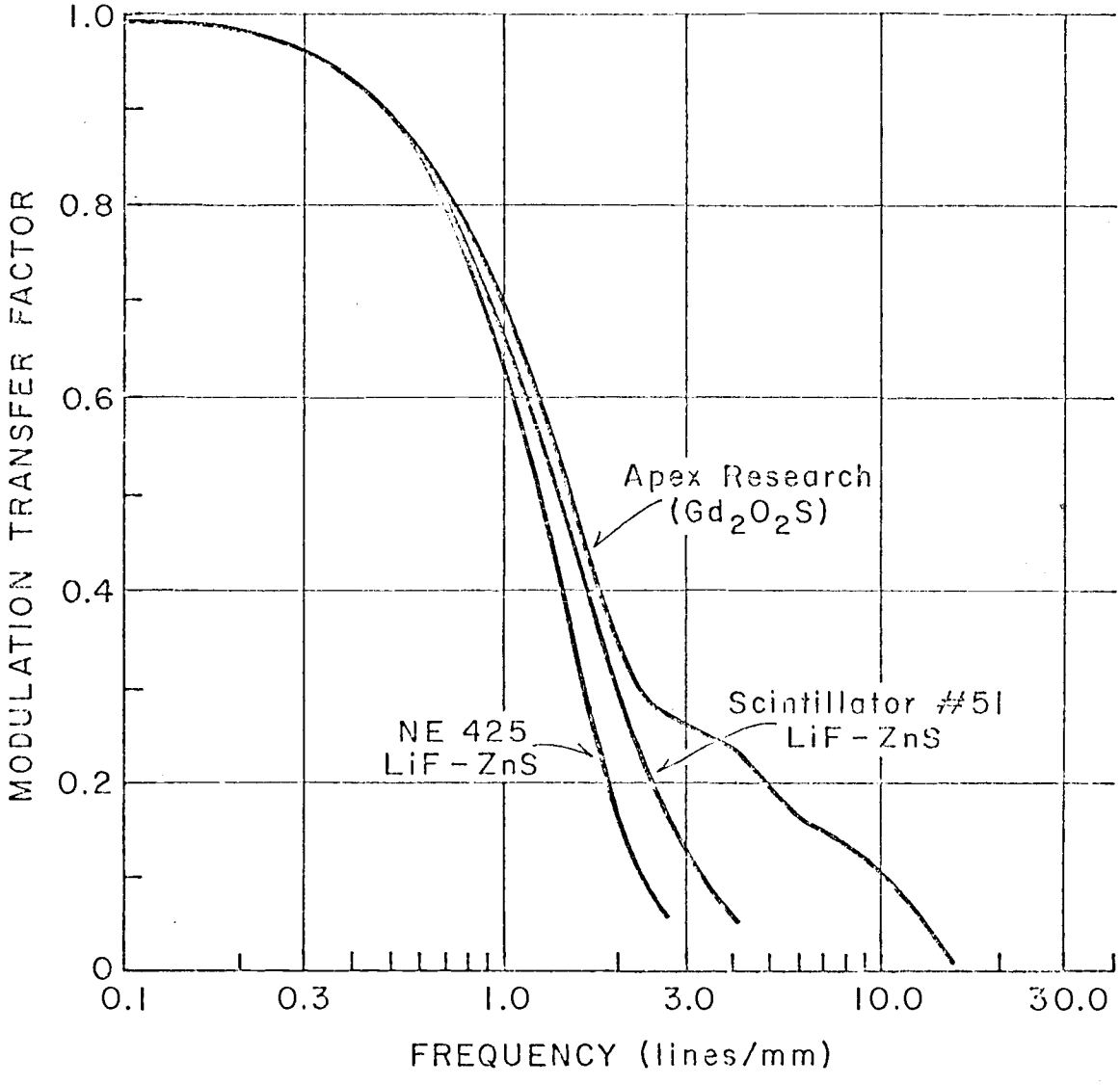

commercial NE 425 scintillator. The effect of the collimator on the geometric unsharpness of a radiograph is shown in figure 5-7. Two gadolinium foil radiographs of the sharp edge are compared; one with the edge in contact with the cassette and the other with a 2 cm separation. The separation represents about the distance between the center of an object and the scintillator screen in the high speed motion neutron radiography facility. The effect of the unsharpness is considerable. In fact it is about the same as the total high speed motion system MTF. There may be some advantage to be made in using a higher collimator ratio when this separation exists although the neutron flux at the object will suffer.

5.6 Conclusions

The modulation transfer function has been used successfully for the high speed motion system to characterize the relative response of the individual components for resolution characteristics. The results brought out the phenomena that the image intensifier-camera system is superior in image quality to a simple scintillator film system. Improvements in the scintillator should of course be the predominant focus of attention for improving overall quality in high speed motion radiographs. The rotating prism high speed camera and the image intensifier may also be considered for improvements but they are definitely superior to the scintillator. The beam port collimator does exhibit significant unsharpness problems that parallel the high speed system at a 2 cm object to screen separation. Depending on the position in the object where the resolution is desired, it may be of

Figure 5-7

MODULATION TRANSFER FUNCTION
FOR GEOMETRIC UNSHARPNESS

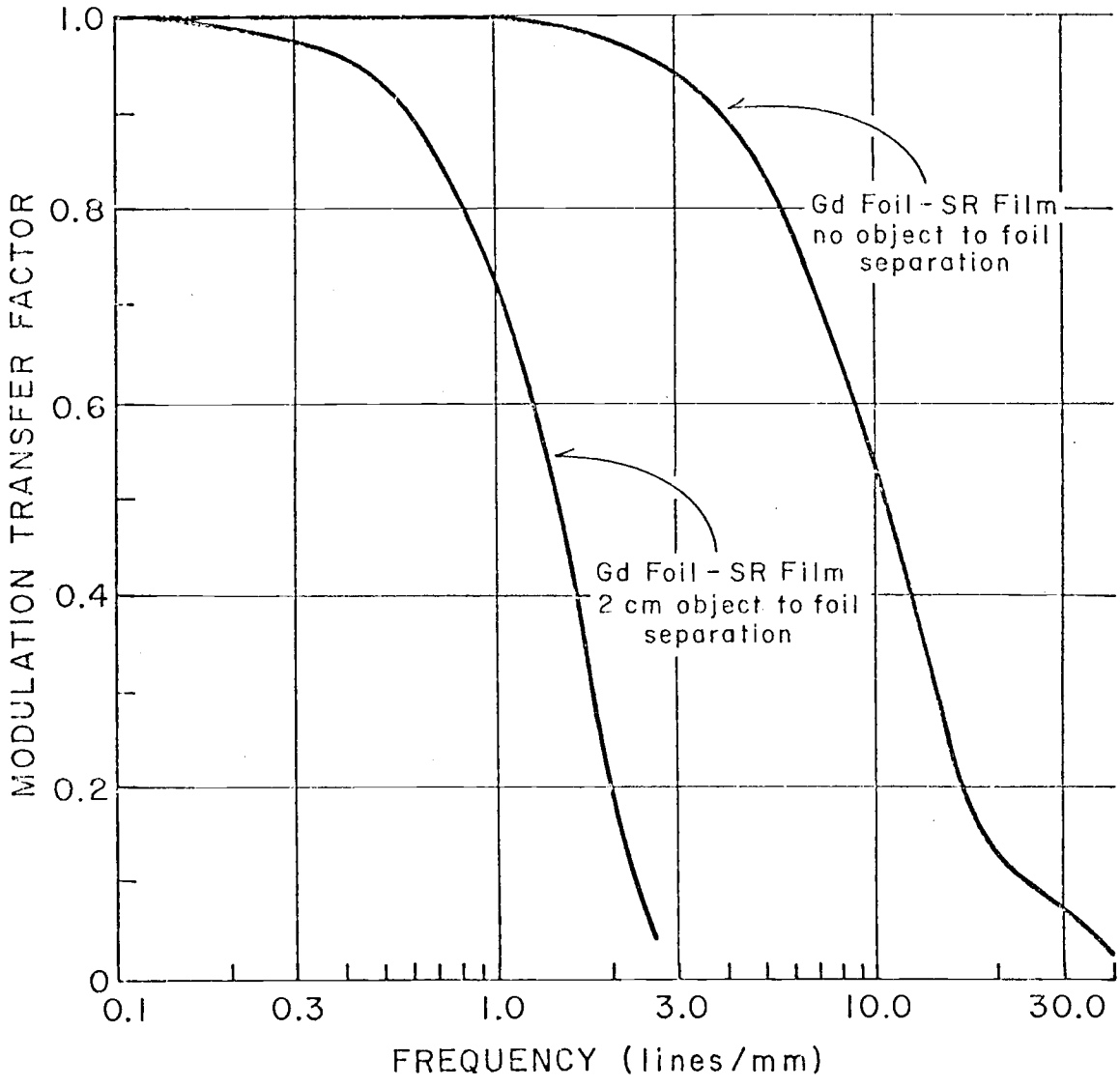

value to increase the collimator L/D. However in doing so the beam intensity will be reduced and may cause other limitations in image quality.

The modulation transfer function itself was found to be measurable using the edge scan technique and a computer algorithm based on a cubic spline interpolation of the edge. The accuracy of the techique was very good for the test cases run but the precision for the experimental work was disappointing. Certainly whenever feasible, a large number of scans should be used to establish the correct value by averaging and reduce the error bands. Ten or more independent scans of the edge radiograph would be preferred. The MTF curves presented are helpful in determining the system limitations although they are not found to be an ultimate image evaluation as noise was removed for the analysis. Similar evaluation may have been made by a resolution test object. Unfortunately due to the nonlinearity of the scintillator-image intensifier combination the commutative properties of the MTF could not be applied to the high speed system.

VI. NEUTRON STATISTICS

6.1 Introduction

In a high speed motion neutron radiography system the use of high efficiency scintillators and light amplification allows the formation of the radiographic image with a minimum neutron signal. However, the number of neutrons which go into each imaged frame is very important. The final image is composed of the recording of numerous individual events. Since the neutron itself behaves according to statistical laws, the radiographic detail may be limited by the statistical nature of the number of events which take place. The problem of statistical limitation in imaging is not unique to high speed neutron radiography but exists in vision, photography and x radiography (110-113).

6.2 Image Detail Visibility

The ability to discern detail in a radiograph is based on recognizing a change in density as being due to a true indication and not noise. The term visibility has thus been given to the signal to noise ratio in radiographs,

$$\text{visibility} = \frac{\Delta D}{\sigma(D)} \qquad (6\text{-}1)$$

where ΔD is the change in density due to a change in the object and $\sigma(D)$ is the standard deviation of the film density due to statistical fluctuations. For just visible images this threshold signal to noise ratio has a value of about 5 (114). The noise in the film density, measured as $\sigma(D)$, is called radiographic mottle which involves quantum

mottle, structural mottle and film graininess. The quantum mottle is caused by the spatial distribution of neutron events and also photon events generated in the scintillator screen. The structural mottle is due to the scintillator screen statistical variation in light yield as was found in Chapter IV or any inhomogeneous distribution of grains. The image intensifier may add to the structural mottle through any statistical deviations in the processes of photoemission and cathodoluminescence. The film graininess of course is due to the individual grains which compose the film image. Thus

$$\sigma^2(D) = \sigma_N^2 + \sigma_S^2 + \sigma_I^2 + \sigma_G^2 \qquad (6\text{-}2)$$

where σ_N, σ_S, σ_I and σ_G are standard deviations due to the number of neutrons making up the image, the scintillator screen, the image intensifier and the film graininess on the final radiograph. The last three components are fixed by the specific system employed. It is only possible to change these values by changing the type of scintillator, image intensifier or film. The first term however is a function of neutron exposure which at low enough levels can become the predominant effect.

A neutron beam impinging on the object has an intensity N_o neutrons per unit area. The spatial distribution of the beam is considered Poisson and so has a standard deviation equal to the square root of N_o. This beam is partially transmitted through the object to yield a new intensity N neutrons/unit area such that

$$N = N_o e^{-\Sigma t} \qquad (6\text{-}3)$$

where Σ is the macroscopic cross section for the object and t is the

object thickness. The term $e^{-\Sigma t}$ is a constant over a uniform area of the object. Since the distribution of a Poisson distribution multiplied by a constant probability is also Poisson, the transmitted beam will have a standard distribution $\sqrt{N}$. Similarly the number of neutrons per unit area absorbed in the scintillator screen will be

$$n = \varepsilon N \tag{6-4}$$

where ε is the scintillator neutron absorption efficiency, and will have a standard deviation $\sqrt{n}$. The film density that results from n neutron events per unit area in the scintillator may be approximated by

$$D = \gamma \log_e (\beta n) \tag{6-5}$$

where βn is the light exposure to the film, β is the light amplification of the scintillator-image intensifier system and γ is the characteristic response of the film. The change in density for a change in n is given by

$$\frac{dD}{dn} = \frac{\gamma}{n} \tag{6-6}.$$

When the statistical fluctuation in the film density is due primarily to the statistical fluctuation in the neutron beam, the case of statistical limitation, then the standard deviation of the film density follows from equation 6-6,

$$\sigma(D) = \frac{\gamma}{n} \sigma_n = \frac{\gamma}{\sqrt{n}} \tag{6-7}.$$

Substituting equation 6-4

$$\sigma(D) = \frac{\gamma}{\sqrt{\varepsilon N}} \tag{6-8}.$$

The signal in the final image is found from equation 6-3 and 6-6 where

$$\frac{dn}{dt} = -\Sigma\varepsilon N_o e^{-\Sigma t} = -\Sigma n \qquad (6\text{-}9)$$

and

$$\frac{dD}{dt} = \frac{dD}{dn} \cdot \frac{dn}{dt} = -\Sigma\gamma \qquad (6\text{-}10)$$

then

$$\Delta D = -\Sigma\gamma\Delta t \qquad (6\text{-}11).$$

The final visibility of equation 6-1 will be

$$\text{visibility} = -\Sigma\sqrt{\varepsilon N}\,\Delta t \qquad (6\text{-}12).$$

Equation 6-12 indicates that in the range of statistical limitation detail visibility is dependent on the object absorption cross section and thickness change. When the visibility limit of 5 is reached

$$N = \frac{25}{\varepsilon(\Sigma\Delta t)^2} \qquad (6\text{-}13)$$

neutrons are required to observe the indication. The essential nature of equation 6-13 for neutron radiography has been described previously by Hawkesworth (115) including the effects of unsharpness. Others have demonstrated experimentally the validity of limitations in visibility at low quantum levels for objects with varying Σ and Δt values to support equation 6-12 (111,112).

6.3 Experimental Determination of the Statistical Limitation

The high speed motion neutron radiography system operates during a TRIGA pulse of nearly 3000 MW. This yields a neutron intensity at

the object position of 4.2×10^{11} neutrons/cm^2-second. If the object transmits 10% of the neutrons and the scintillator absorbs 10% of the transmitted beam then 4.2×10^9 n/cm^2-sec contribute to the imaging process. At 5000 frames/second the high speed camera allows 80 μsec of exposure per frame. This means each frame is imaged with about $N_o = 3.4 \times 10^7$, $N = 3.4 \times 10^6$ and $n = 3.4 \times 10^5$ n/cm^2. It is of interest to know whether or not images formed with this exposure are limited in quality by the neutron statistics or by the imaging characteristics of the scintillator, intensifier and camera system.

To test this the high speed motion facility is arranged as shown in figure 6-1. The neutron beam passes through the object, strikes the scintillator screen and light from the scintillator is amplified by the image intensifier as is performed in the high speed work. A 35 mm Pentax camera is focused on the output of the image intensifier instead of the high speed camera however. The operation of the system involves steady state operation of the TRIGA reactor at low power and remote opening of the camera shutter for extended periods to integrate the exposure. Table 6-1 correlates the exposure necessary in KW-minutes of reactor power and time to correspond to the reactor pulse exposure at different frame rates. Because the image intensifier provides light amplification the film will receive suitable exposure in a reasonable time. The film exposure is adjustable by the integrated neutron exposure and the f-stop setting on the 35 mm camera. The f-stop settings provide a variation of light intensity by a factor of over 100. This allows a constant film density to be maintained while the neutron exposure for individual radiographs is varied by a factor of

Figure 6-1

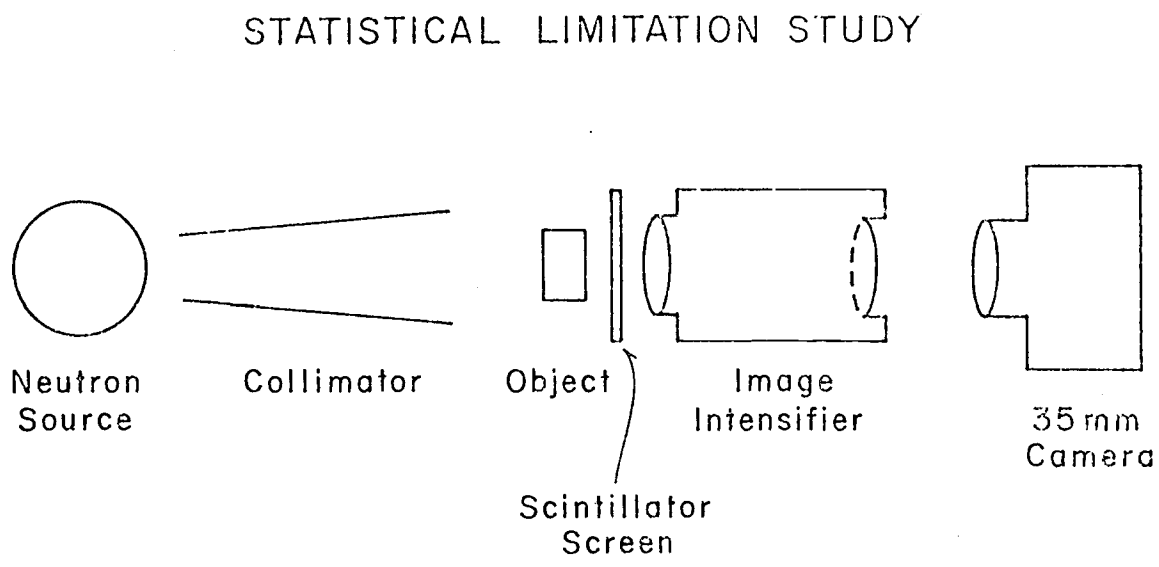
STATISTICAL LIMITATION STUDY
Neutron Source
Collimator
Object
Image Intensifier
35 mm Camera
Scintillator Screen

Table 6-1

RADIOGRAPHIC EXPOSURE AT DIFFERENT FRAME RATES

FOR A 3000 MW PULSE

Frame Rate (frames/sec)	Exposure (KW-min)	N_o (n/cm^2)
1000	20	1.7×10^8
2000	10	8.4×10^7
4000	5	4.2×10^7
5000	4	3.4×10^7
8000	2.5	2.1×10^7
10,000	2	1.7×10^7
20,000	1	8.4×10^6

100. The effect of changing the f-stop of the lens on the camera resolution is minimal having a resolution capability far beyond the scintillator screen at the worst settings.

6.4 Results

Figure 6-2 shows the results of the VISQI (79) test object radiographed at exposures of 10 KW-min down to 0.1 KW-min with three LiF-ZnS scintillators. The film densities are consistent within each scintillator screen set of exposures within 10%. This is important in comparing quality as the visibility of VISQI faults is dependent on film exposure. Five exposures are shown in the figure. Since printing and reproduction of the original negatives causes some loss of detail, table 6-2 contains the tabulated sensitivity analysis, as was performed in Chapter IV, for the first two steps of the VISQI. It is clear that as the neutron exposure is decreased the ability to discern detail is diminished. This apparently occurs around 1 KW-min or $N_o \simeq 10^7$ n/cm^2 for scintillators #51 and #54. Radiographs taken by these scintillators with less than 10^7 n/cm^2 will be limited in VISQI detail visibility by the statistical limitation of the system whereas images with more than 10^7 n/cm^2 will depend on the quality of the scintillator for image quality. In the case of scintillator #56, statistical limitation does not appear to be demonstrated until about 0.3 to 0.1 KW-min. This scintillator is thicker than the other two and has a greater neutron absorption efficiency. Although VISQI readings are not absolute it does appear that this greater absorption efficiency has a recognizable effect. The lower reading at 10 KW-min

Figure 6-2

STATISTICAL LIMITATIONS IN VISQI RADIOGRAPHS

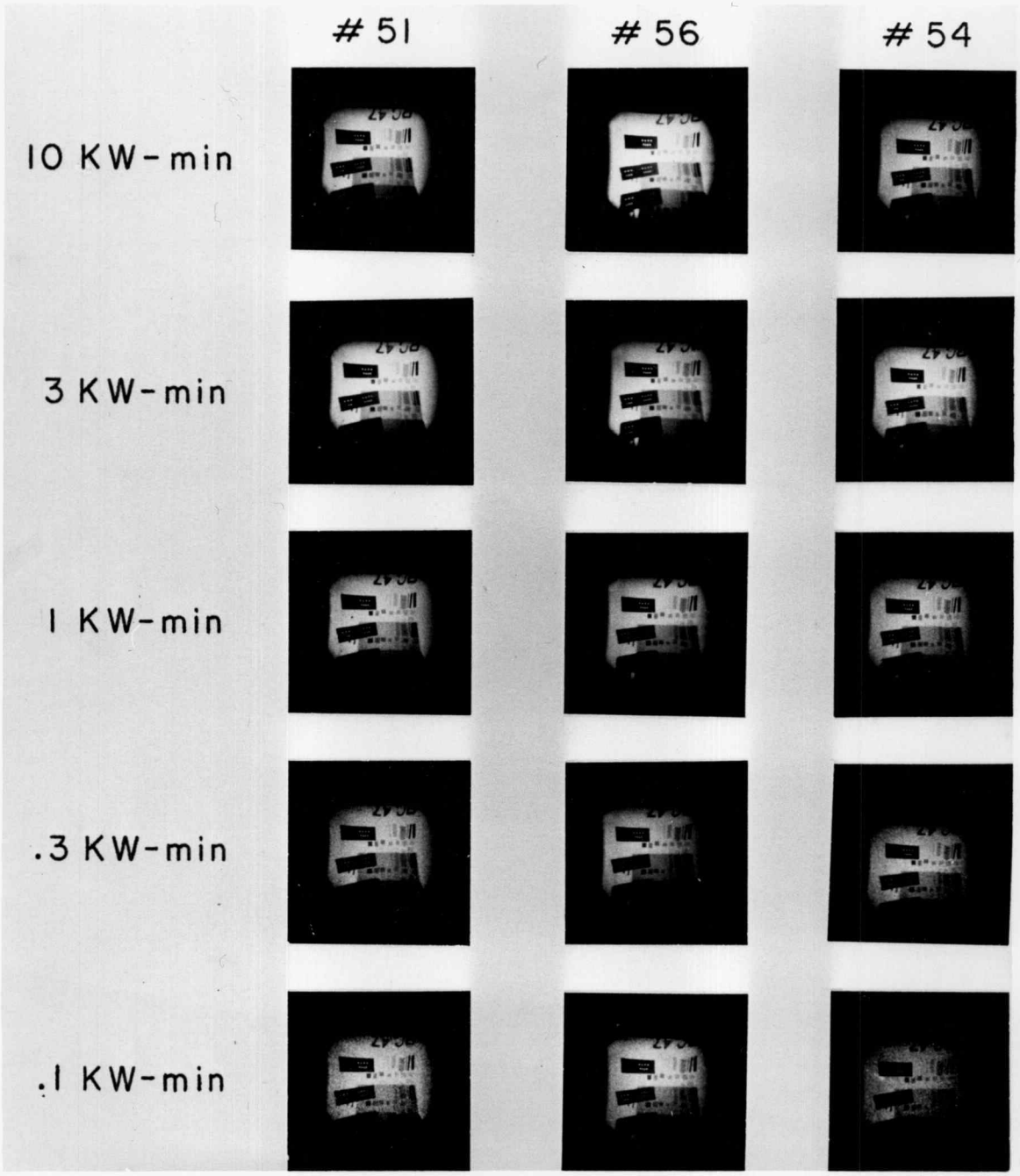

Table 6-2

VISQI SENSITIVITY READINGS FOR NEUTRON STATISTICS

COMPARISON

	Scintillator #51 (2/1 ZnS/LiF 0.127 mm)		Scintillator #56 (2/1 ZnS/LiF 0.239 mm)		Scintillator #54 (4/1 ZnS/LiF 0.127 mm)	
Exposure	density	sensitivity	density	sensitivity	density	sensitivity
10 KW-min	1.58	34½	1.69	35½	1.54	35½
3 KW-min	1.66	34½	1.61	37	1.64	35
1 KW-min	1.59	33	1.54	36	1.56	33½
.3 KW-min	1.53	32	1.56	35	1.56	30½
.1 KW-min	1.57	23½	1.57	31½	1.45	21

for #56 appears to be due to the slightly higher density burning out some of the fine detail. At the other exposures the density is more uniform and the readings should be a valid representation of the statistical effect.

Figure 6-3 shows another set of radiographs of a blank cartridge in a steel barrel. The blank is only half filled with gun powder as indicated by the lighter area in the cartridge. The numbers below each print are the exposure given in KW-min. The image quality is seen to be fine down to the range of 1 KW-min when it begins to deteriorate slightly due to statistical limitations. Referring to table 6-1, with frame rates of 10,000 frames per second and a 3000 MW pulse the images should not be statistically limited as the exposure is on the order of 2 KW-min with an incident beam strength of 1.7×10^7 n/cm^2.

6.5 Conclusions

The significance of the statistical problem lies in the choice of the neutron source and the object. In the case where the pulsing capability is not so great the statistics can be a problem at high frame rates. Also if objects of very high neutron attenuation are radiographed the transmitted signal may be quite small. In this instance the detail visibility is determined by equation 6-13. Consider a beam intensity and object transmission such that, $N = 10^6$ n/cm^2 $= 10^4$ n/mm^2. If the scintillator has 10% efficiency then

$$\Sigma\Delta t = \left[\frac{25}{(.1)(10^4)} \right]^{\frac{1}{2}} = 0.16 \qquad (6\text{-}14)$$

Figure 6-3

STATISTICAL EFFECTS IN ORDNANCE NEUTRON RADIOGRAPHS

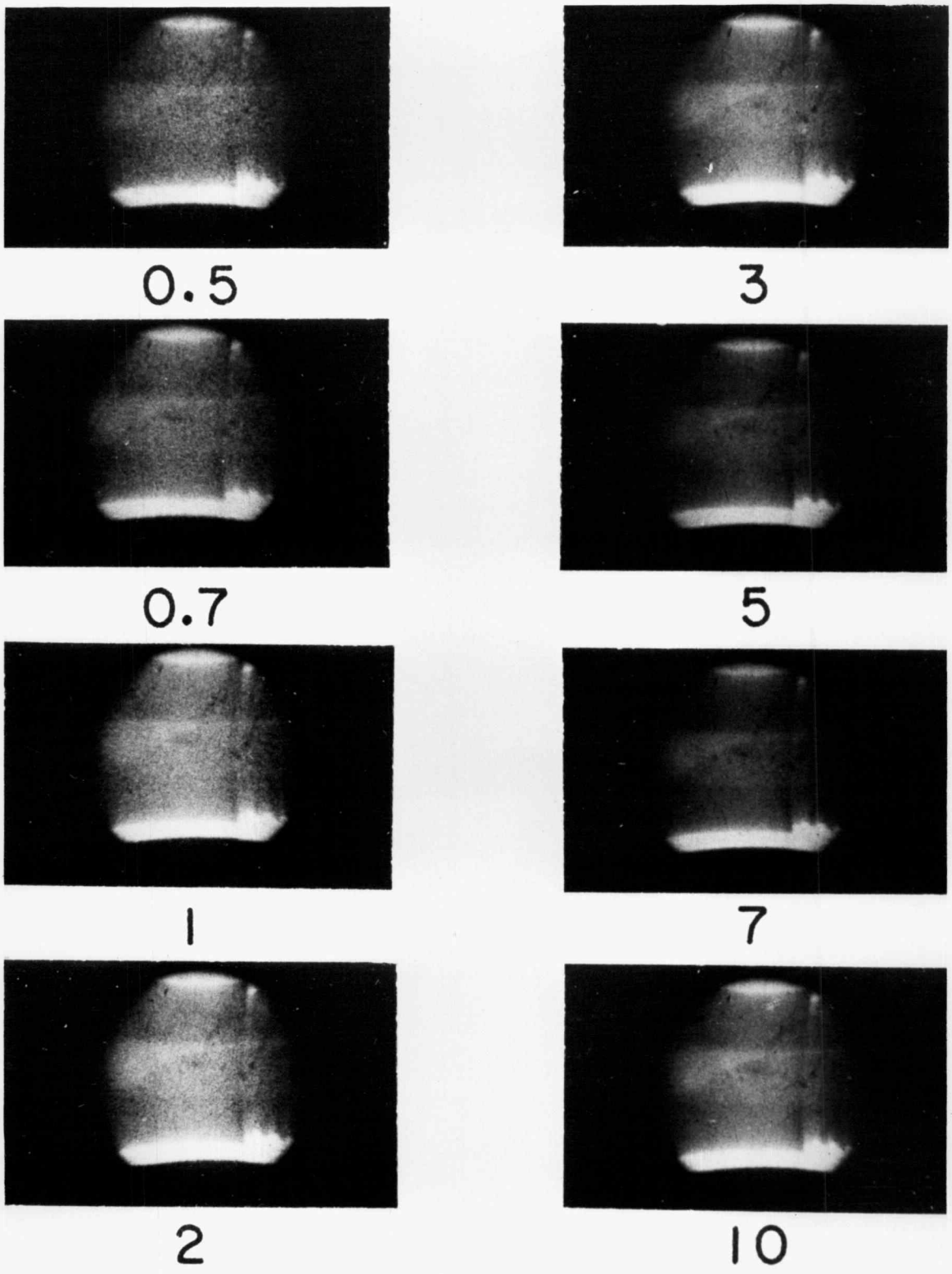

for a 1 mm square detail to be visible. Often, if Δt is small, the neutron absorption coefficient Σ must be increased by doping the object with a higher contrast material to make the desired image visible.

When statistical limitations become a limitation in imaging three possibilities exist. The neutron source may be upgraded. This should be the first approach. In the event that this cannot be satisfactorily accomplished a more efficient scintillator screen can be used. For the LiF-ZnS screen, a screen more highly concentrated with Li-6 or a thicker screen could be made. The loss in light yield that may occur in such a change may be compensated for by the image intensifier or film used. Since the image quality is limited by statistics a degradation due to the higher efficiency scintillator or other component should not be harmful. Finally the collimator L/D ratio may be reduced. This will also degrade the image quality somewhat; however it will certainly improve the neutron statistics. To achieve the best imaging system compromises must be made in the selection of the high speed components.

VII. RESULTS AND CONCLUSIONS

7.1 High Speed Motion Neutron Radiography of Ordnance Devices

The work performed on the development of a high speed motion neutron radiography system clearly demonstrates the feasibility of such an operation. The system described has been applied to the ballistic cycle of a 7.62 mm ordnance device. The device studied is shown in the photograph of figure 7-1, where a blank cartridge (half filled with powder), a live cartridge (filled with powder), the firing breech and gun barrel are displayed. Figure 7-2 is a photograph of the ordnance assembly in front of the neutron radiography beam port. A bullet trap is located on the right into which the barrel is clamped. Shielding is located in the foreground and background and the entire facility is surrounded by a concrete blockhouse. The high speed system components are shown in figure 7-3 in their appropriate order outside the high speed radiography facility. The masonite collimator has a restricted opening which limits the imaging area only to the region of interest which is the powder bed of the cartridge. A 5 x 5 cm scintillator screen, constructed at OSU, is the white object leaning on a support. Figure 7-4 shows these components as they are installed in the high speed radiography facility except for the scintillator. The neutron beam port opening is visible at the left and the bullet trap on the right. The breech is connected to the firing circuit wire which extends outside the facility blockhouse. The rifle barrel, image intensifier and high speed camera are each mounted separately

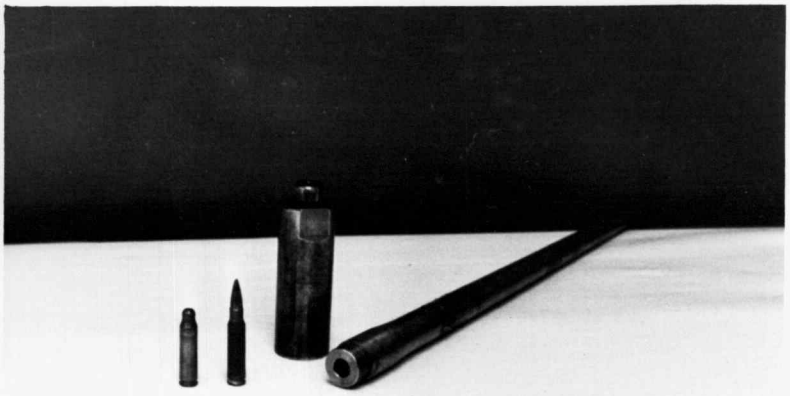

Figure 7-1
CARTRIDGES AND
RIFLE BARREL

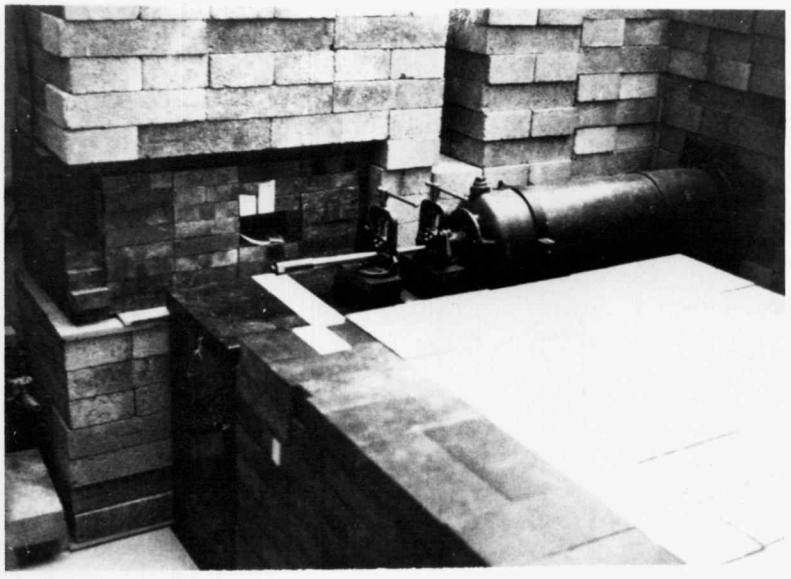

Figure 7-2
BEAM PORT FACILITY

Figure 7-3
HIGH SPEED
IMAGING COMPONENTS

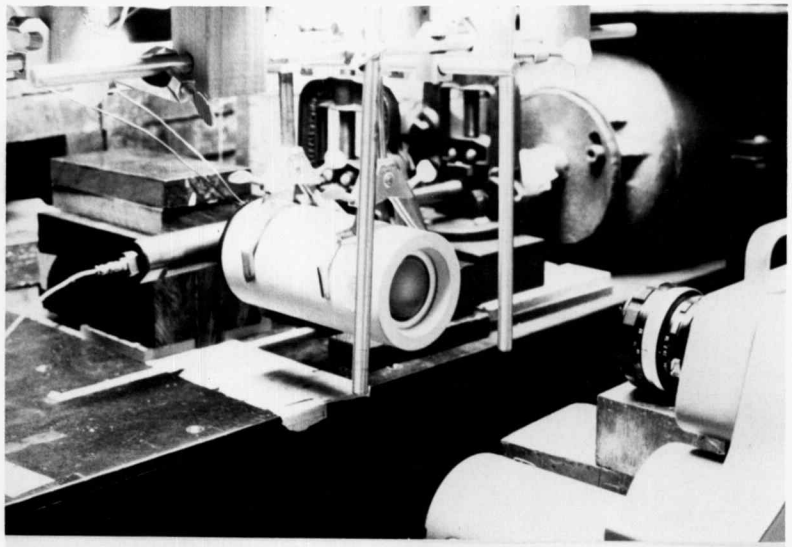

Figure 7-4
ASSEMBLED HIGH
SPEED FACILITY

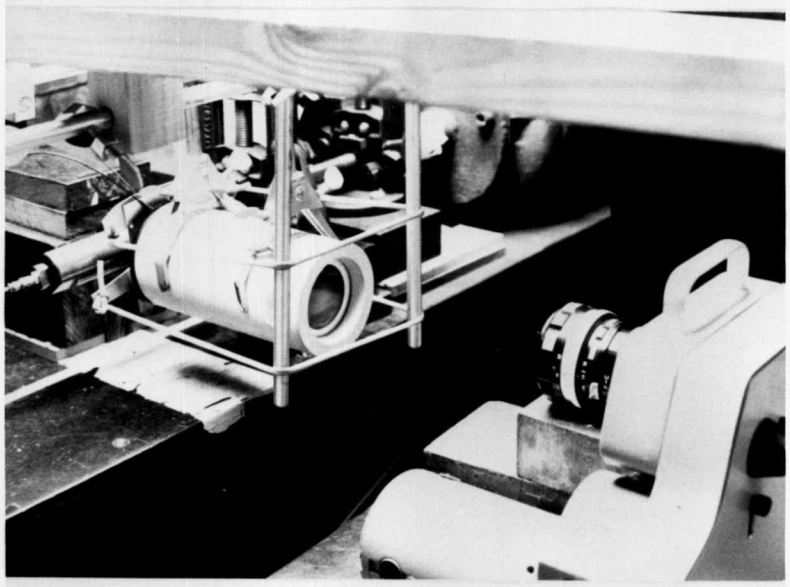

Figure 7-5
ASSEMBLED HIGH
SPEED FACILITY

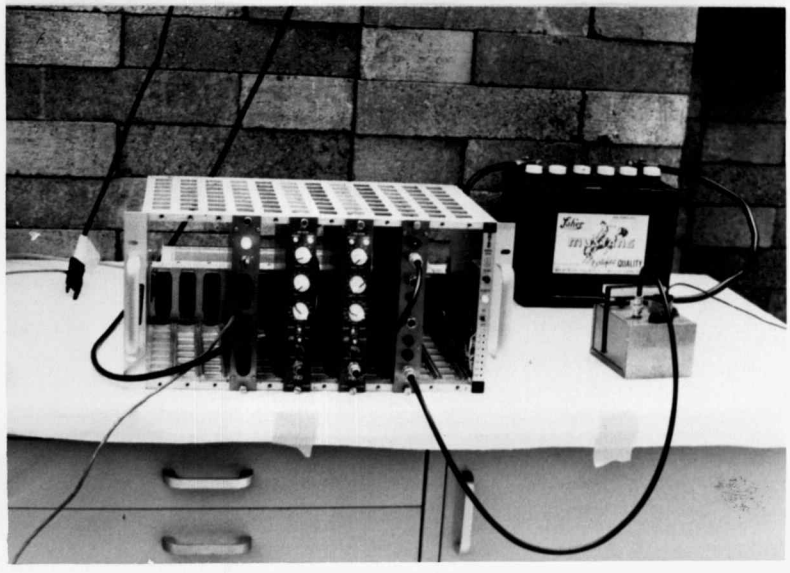

Figure 7-6
SYNCHRONIZATION
COMPONENTS

so that any vibration due to the firing event or camera motor will not influence the other imaging components. Figure 7-5 is again taken in the facility and shows the elastic bands and aluminum plate which hold the scintillator screen firmly against the image intensifier. In this manner, neutrons from the beam port pass through the restricting collimator of masonite, through the breech and barrel, striking the scintillator screen. The scintillator light is amplified by the image intensifier in contact with it and the image displayed on the intensifier output faceplate is recorded by the high speed camera. During actual radiography, the facility is kept dark with a black cloth over the scintillator and intensifier area and also a black paper tube is run between the intensifier output faceplate and the high speed camera lens in order to prevent any stray light from entering the final radiographs.

The electronics for controlling the timing of the camera, reactor pulse and firing of the event are shown in figure 7-6. This photograph is taken outside of the shielded blockhouse of the radiography facility. The camera signals the relay switch located in the left instrument of the nuclear instrument module (NIM) bin. The relay signals the reactor to initiate the pulse and also starts the Nuclear Data Clock/Time Base sequence. The first Clock/Time Base (second from left in the NIM bin) counts for 170 milliseconds, then signals the second Clock/Time Base (second from right in the NIM bin) to count for 16 milliseconds. This Clock/Time Base then signals the differential comparator box on the right in the NIM bin which triggers the silicon control rectifier (SCR) in the smaller gray box. The SCR

along with a dead man's switch complete the circuit for the 12 volt battery charge to fire a gas ignitor in the breech, firing the cartridge. Circuit diagrams of the electronics are given in Appendix D.

Two high quality neutron radiographs of both a blank and live cartridge in the rifle barrel with the breech in place are shown in figure 7-7. The difference in visibility is readily seen as the blank contains a void due to the partial fill of powder which provides good contrast to the propellant. The live round on the other hand does not have as good a visibility of the powder. In fact, the powder bed is slightly darker than the surrounding barrel in this radiograph but will become lighter as it is consumed during firing until a void is formed. On the right, in the radiograph, the breech is shown with a central cavity. The firing pin can be seen just slightly back from the breech faceplate. The gas ignitor system fills this cavity generating a pressure which forces the firing pin into the primer on the cartridge. The region of interest which is masked for the high speed radiographs by the masonite collimator is a rectangular area of the powder bed alone. Figures 7-8 to 7-11 show some results of the high speed motion neutron radiography experiments. Reproduction has reduced the detail visibility and density latitude of the original negative, but major features remain.

Figure 7-8 contains the sequential frames of a blank being fired with the camera at 2000 frames/second. The powder lies flat across the imaged area. As the firing is initiated the bed humps up in several locations and is then consumed relatively evenly. The burning sequence covers about 2 to 2.5 milliseconds. Figure 7-9 is also

Figure 7-7

HIGH QUALITY NEUTRON RADIOGRAPHS OF 7.62 mm RIFLE BARREL

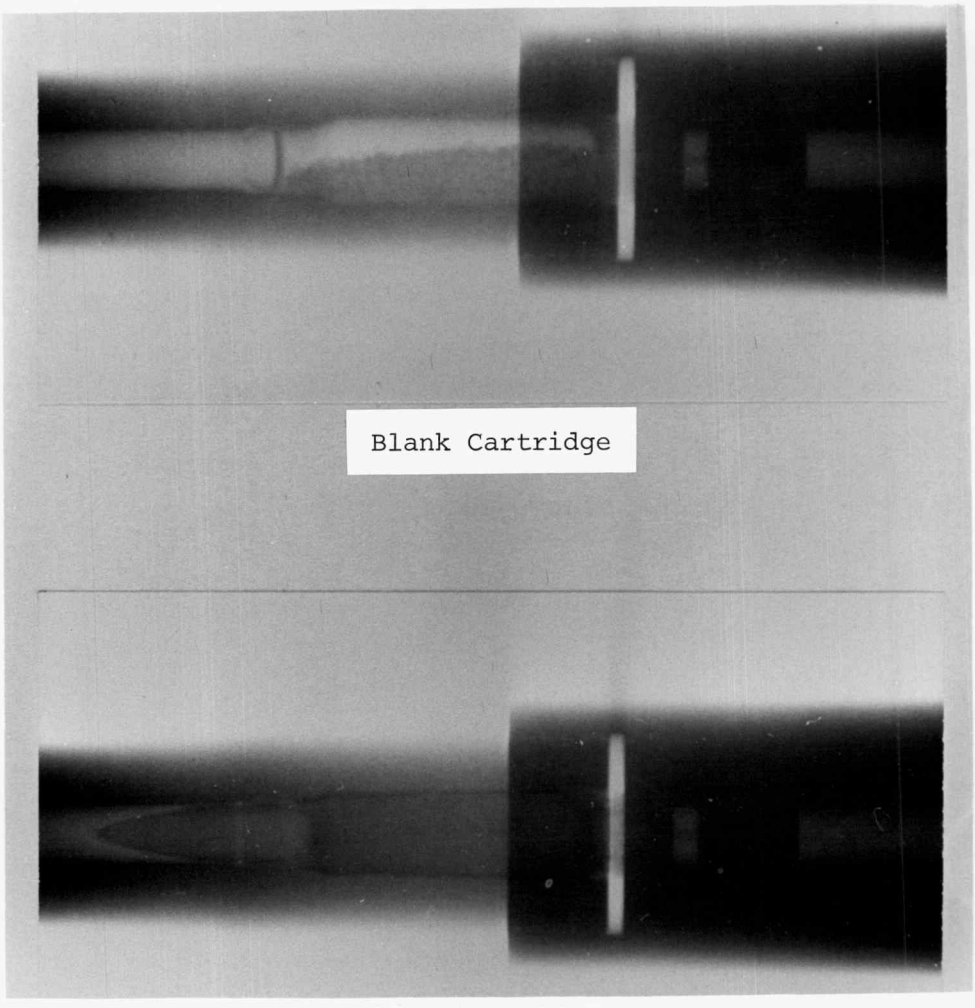

Live Cartridge

HIGH SPEED MOTION NEUTRON RADIOGRAPHS OF BLANK CARTRIDGES

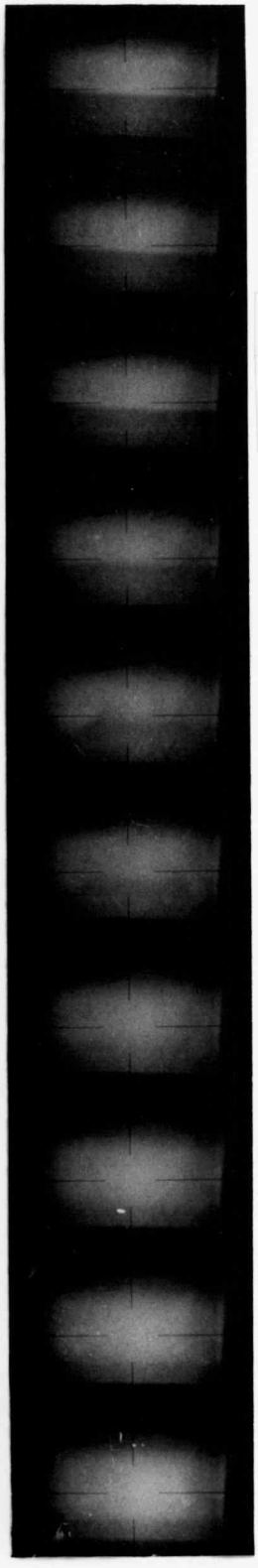

Figure 7-8

2000 frames/sec

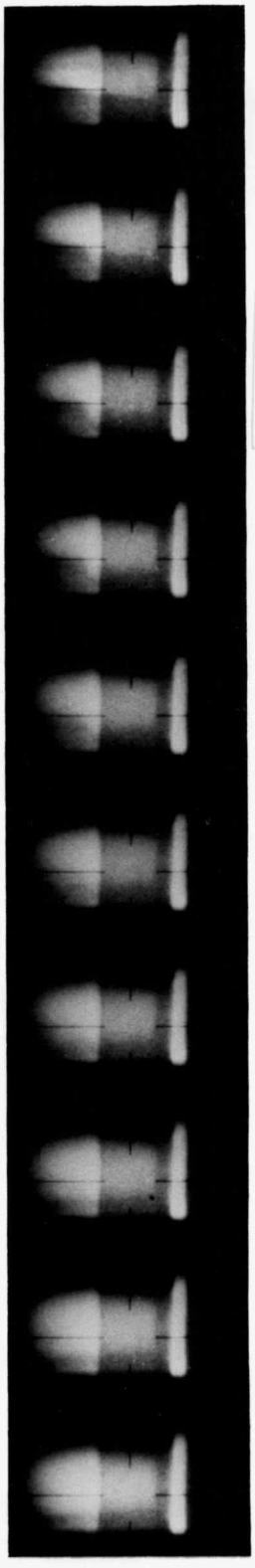

Figure 7-9

5000 frames/sec

HIGH SPEED MOTION NEUTRON RADIOGRAPHS OF LIVE CARTRIDGES

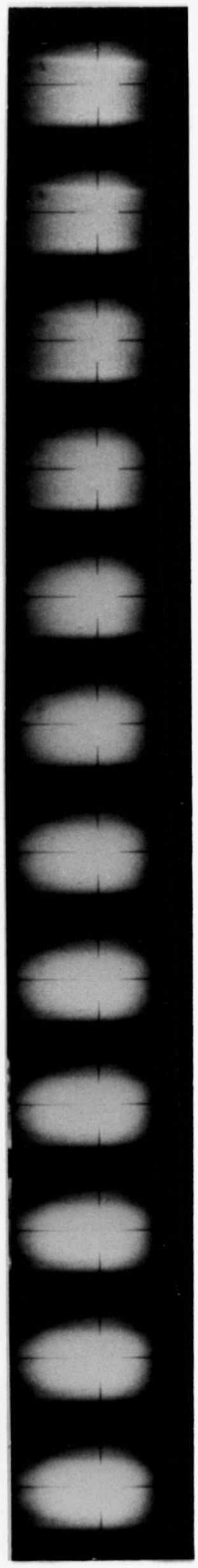

Figure 7-10

5000 frames/sec

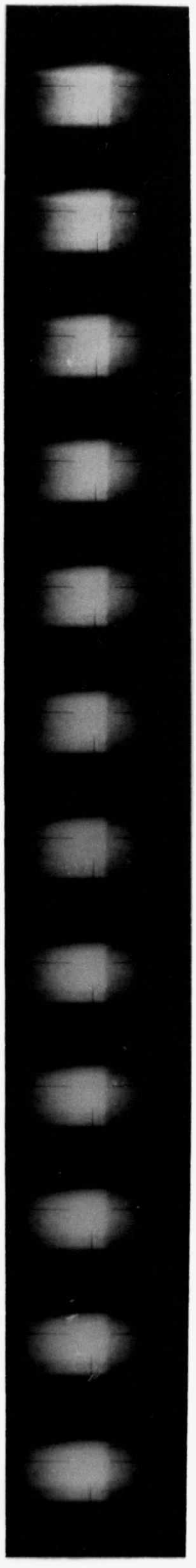

Figure 7-11

8000 frames/sec

a blank cartridge viewed near the primer end, The overlap of the breech threaded onto the barrel is distinctly visible as the change in beam attenuation due to the additional steel thickness reduces the exposure in that region. The frame rate of the camera is 5000 frames/second. Ten consecutive frames are reproduced in the figure. Following the initiation of the event a depression of the powder bed occurs at about the interface at the end of the breech. Powder located toward the primer burns down evenly. Powder located to the nose is apparently pushed up some and burns while simultaneously being propelled down the barrel. After 8 or 9 frames, or about 1.6 to 1.8 milliseconds, the powder has apparently cleared this portion of the cartridge.

Figure 7-10 is a full cartridge radiographed during firing at 5000 frames/second, The view is taken in the mid section of the cartridge near the bullet end. Two Gd_2O_3 tagged grains are present near the top left corner of the propellant. The Gd_2O_3 inserted in the live round improves the contrast for the tagged grains making them easily detectable as dark spots on the print. The very high thermal neutron cross section of gadolinium causes this effect. In doping the powder bed in this manner the charge has been reduced slightly for safety resulting in an air gap at the top of the cartridge that may be seen in the undisturbed shell as a white line, This is not present in the live round of figure 7-7. At the instant of firing, the gap and the tagged grains show movement. The gap fills with neutron opaque propellant at first, but as burning procedes the chamber clears, The Gd_2O_3 tagged grains move to the left and disappear in two

frames. The black dots in the sixth frame are artifacts on the film. The burning cycle covers about 4 or 5 frames which is approximately 0.8 to 1 milliseconds. Although the barrel is firmly clamped in place for firing, the recoil force is strong enough to cause movement. This is detectable in the last frames shown as the shoulder of the barrel becomes visible due to the shifting to the right. This movement continues for about 2 milliseconds after the firing.

Figure 7-11 is also a live cartridge radiographed at a nominal 11,000 frames/second which corresponds to about 8000 frames/second at the time of firing. The mid section of the cartridge is in view with the end of the breech visible on the right side. The firing occurs over about 8 frames. The top of the propellant can be seen as a slightly sloping line through the barrel on the left and the breech and barrel on the right. As the propellant burns and moves from the field of view, the bottom of the barrel cavity appears as a horizontal line near the lower edge of the frame. There is the impression in the original negative that some powder is forced back against the ignitor on the right while burning proceeds in the mid section. This appears to generate a moon-shaped form against the ignitor end before finally being consumed and disappearing from view. Recoil action can be noted as the breech moves to the right.

7.2 High Speed Motion Neutron Radiography of Two Phase Flow

The high speed motion system has also been tested for observing two phase flow. For experimental purposes, air bubbles were pumped through water in a container and high speed motion neutron radiographs

taken. This type of object offers some advantage over the ordnance device in that no timing systems are required. The two phase flow is initiated and runs continuously. The reactor is taken to a low power level and prepared for a pulse. The camera is then started; once it reaches speed, the reactor is signaled to pulse and the motion radiographs are taken. The difficulty of this type of radiography is in the very high neutron scattering cross section of water (Σ_s = 3.45 cm^{-1}). This significantly influences the thickness of water that may be penetrated and also generates a large number of scattered neutrons which may obscure the visibility of detail in the final image. For these reasons, only a one centimeter thickness of water was penetrated and also a linear antiscatter grid (L/D = 18) obtained from W.L. Parker (48) was placed between the object and scintillator screen.

Radiographs from the two phase flow experiment are shown in figures 7-12 and 7-13. Figure 7-12 is taken at 1000 frames/second with every fifth frame reproduced. Figure 7-13 is taken at 2000 frames/second with every tenth frame reproduced. Over the width of the pulse, about 12 milliseconds for these approximately 1250 MW pulses, not a great deal of change has taken place. This has hindered reproduction as frames from the far extremes of the film strip must be viewed where the background film density has changed considerably over the pulse duration. The prints shown have been adjusted to similar print film density but in doing so the area of the field of view has not remained consistent. Nevertheless, movement is clearly discernable.

In figure 7-12 the main bubble pops off the air input tube and begins to rise. As the bubble rises it is compressed from a round

HIGH SPEED MOTION NEUTRON RADIOGRAPHS OF TWO PHASE FLOW

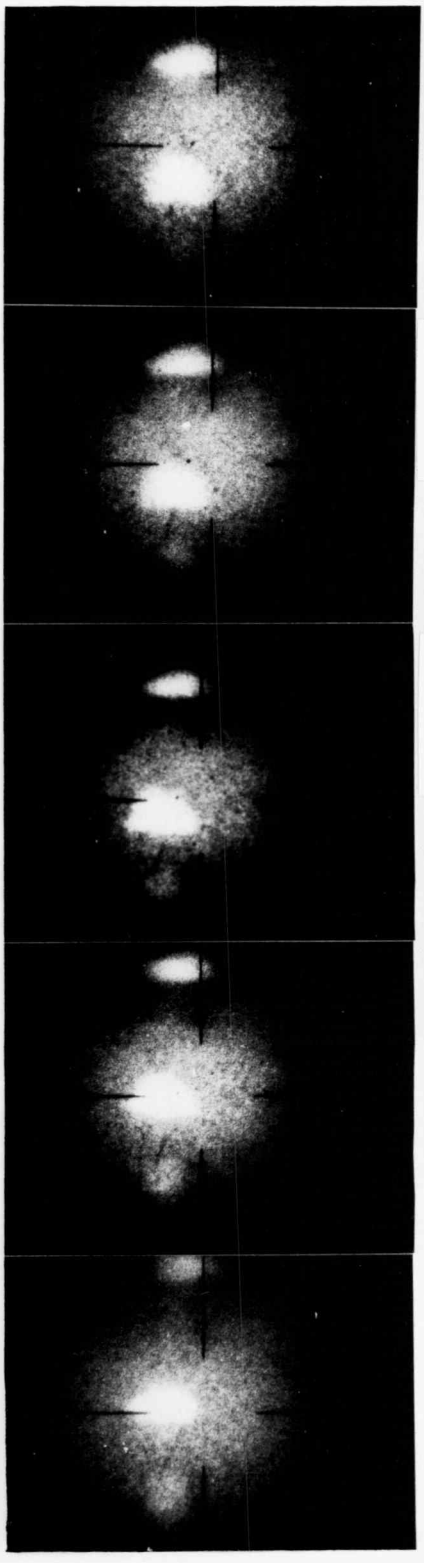

← Figure 7-12

1000 frames/sec
every fifth frame

Figure 7-13 →

2000 frames/sec
every tenth frame

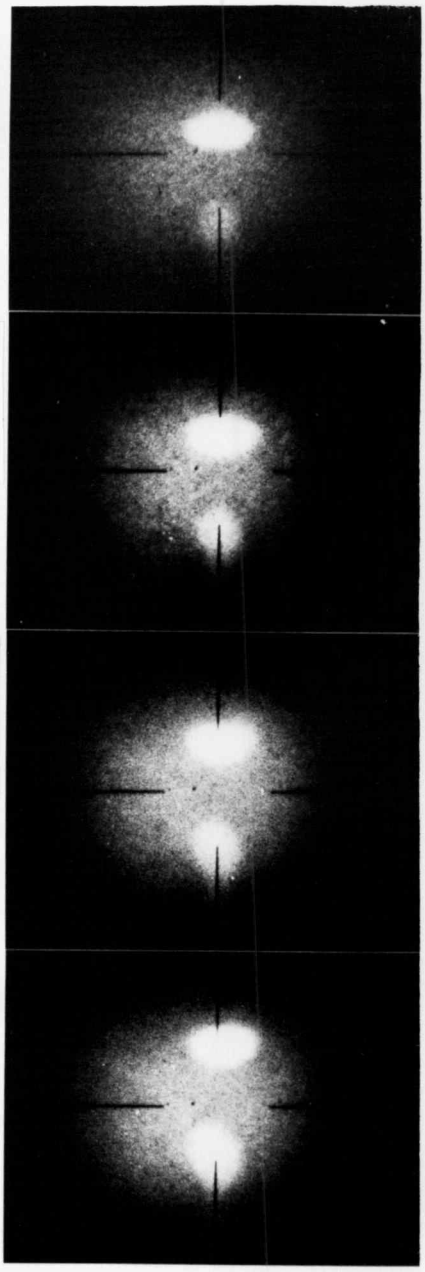

shape to oblong. Over the time of the exposures, the top bubble is seen to move out of the picture and a new bubble begins to form on the input tube. Figure 7-13 shows the growth of a bubble on the input tube while the previous bubble rises.

Although better radiographs of two phase flow could be obtained with slower frame rates and a very much broader reactor pulse, the feasibility of the work has been demonstrated. The use of an anti-scatter grid has also been shown to be valuable. In films taken without the antiscatter grid present the air input tube could not be seen. Reproduction in figures 7-12 and 7-13 unfortunately does not allow a clear view of the tube however the original films show the presence of the tube as do other films in which the antiscatter grid was used.

7.3 Conclusions

The work on the high speed motion neutron radiography system has resulted in successful achievement of the initial goal of radiographing the ballistic cycle of an ordnance device. The final quality of the individual frames did not allow the detail visibility of individual powder grains but the use of contrast enhancement with gadolinium doping provided some compensation. The comprehensive study of the system and the individual components has also brought to light some interesting aspects of benefit not only to the high speed work but also to general neutron radiography.

- The pulsing capability of reactors can be employed for radiography under certain conditions to overcome insufficient steady state power,
- Scintillator screens of the LiF-ZnS variety are the best suited

for high speed motion radiography in the range of 2000 to 10,000 frames/second due to their rapid decay characteristics for light emission and high light yield. Gadolinium oxysulphide screens exhibit superior image quality but unfortunately have a decay time too long for very rapid dynamic radiography.

• While high light yield is desirable in LiF-ZnS scintillators, consideration must be given to resolution and statistical variability of the light per neutron event. The weight ratio of the ZnS to LiF constituents of these scintillators shows subtle differences in yield, resolution and statistical variation. Two to one, ZnS to LiF, scintillators constructed with sodium silicate binder were found to be very successful.

• The image quality of a neutron radiography system can be described by the modulation transfer function (MTF). For imaging systems consisting of a series of components the MTF allows both independent and combined effects of the components on image quality to be evaluated.

• The radiographic image formed with a LiF-ZnS scintillator screen through an image intensifier was found to be superior to that formed by direct exposure to film. The fiber optics coupling and optically focused exposure by a camera offer some image quality improvement by reducing scatter and large angle light exposure to the film which can occur in the case of direct film and scintillator contact.

• MTF analysis, while useful for quantifying response within a system suffers from problems with accuracy using the edge spread technique. Averaging of many independent edge scans is necessary but even so variations of $\pm$ 0.05 in MTF factor can exist. As an absolute measure

of radiographic quality the MTF does not appear to be significantly superior to test object techniques to warrant the sophisticated machinery necessary. In applications such as the high speed system it certainly is valuable as an academic analysis but would not be as valuable for more routine types of neutron radiography.

• The statistical limitation of image quality is of concern for high speed motion or low level neutron radiography reaching a critical value in the range of 10^7 n/cm^2 depending on the object attenuation and neutron converter efficiency. Overall, the components of the high speed motion neutron radiography system must be matched to achieve the best image quality in the presence of restrictions on the neutron source strength available.

VIII. BIBLIOGRAPHY

1. H. Kallman, E. Kuhn, Die Naturwissenschaften, Vol. 25, 1937, p. 231.

2. H. Kallman, Research, Vol. 1, 1948, p. 254.

3. H. Thewlis, "Neutron Radiography", British Journal of Applied Physics, Vol. 7, 1956, p. 345.

4. H. Berger, Neutron Radiography, Elsevier, N.Y., 1965.

5. M.R. Hawkesworth, J. Walker, "Radiography with Neutrons", Journal of Material Science, Vol. 4, 1969, p. 817.

6. H. Berger, "The Present State of Neutron Radiography and Its Potential", Materials Evaluation, Vol. 30, 1972, No. 3, p. 55.

7. A.R. Spowart, "Neutron Radiography", Journal of Physics E, Vol. 5, 1972, p. 497.

8. M.R. Hawkesworth, Ed., Radiography with Neutrons, Conference at the University of Birmingham, September 1973, British Nuclear Energy Society, London, 1975.

9. H. Berger, Ed., Practicle Applications of Neutron Radiography and Gaging, ASTM STP 586, American Society for Testing and Materials, 1976.

10. K.G. Galliher, L.W. Hanna, "Neutron Radiography of Apollo Ordnance", Materials Evaluation, Vol. 29, 1971, No. 8, p. 165.

11. J.J. Haskins, J.F. Jaklevick, C.D. Wilkinson, "Applications of Neutron Radiography in Fast Reactor Fuel Development", Proceedings of 16th Conference on Remote Systems Technology, Remote Systems Division of the American Nuclear Society, Idaho Falls, Idaho, March 1969, p. 218.

12. G. Farny, "Neutron Radiography of Irradiated Fuel Elements Using Cellulose Nitrate", Radiography with Neutrons, M.R. Hawkesworth, Ed., Conference at the University of Birmingham, September 1973.

13. K.D. Kok, "Neutron Radiography of Nuclear Fuels at the Battelle Research Reactor", Practicle Applications of Neutron Radiography and Gaging, ASTM STP 586, American Society for Testing and Materials, 1976, p. 183.

14. A.M. Ross, "Detecting Cladding Leaks in Irradiated Fuel Elements by Neutron Radiography", Practicle Applications of Neutron Radiography and Gaging, ASTM STP 586, American Society for Testing and Materials, 1976, p. 195.

15. C.N. Jackson, Jr., H.G. Powers, C.A. Burgess, "Neutron Radiography of Fuel Pins", Practicle Applications of Neutron Radiography and Gaging, ASTM STP 586, American Society for Testing and Materials, 1976, p. 210.

16. D.J. Hagenmaier, J. Halchak, G. Basl, "Detection of Titanium Hydride by Neutron Radiography", Materials Evaluation, Vol. 27, 1969, No. 9, p. 193.

17. J.P. Barton, "Some Possibilities of Neutron Radiography", Physics of Medicine and Biology, Vol. 9, 1964, No. 1, p. 33.

18. H.L. Atkins, "Biological Application of Neutron Radiography", Materials Evaluation, Vol. 23, 1965, No. 9, p. 453.

19. M. Brown, P.B. Parks, "Neutron Radiography in Biological Media: Techniques, Observations and Implications", American Journal of Roentgenology, Radium Therapy, and Nuclear Medicine, Vol. 106, July 1969, p. 472.

20. P.J. Boyne, W.L. Whittemore, "Neutron Radiography of Osseous Tumors", Oral Surgery, Oral Medicine and Oral Pathology, Vol. 31, February 1971, p. 152.

21. J.P. Barton, "Radiography Examination through Steel Using Cold Neutrons", British Journal of Applied Physics, Vol. 16, 1965, p. 1833.

22. M.R. Hawkesworth, J. Walker, "Cold Neutron Beams for Radiography through Steel", Radiography with Neutrons, M.R. Hawkesworth, Ed., Conference at the University of Birmingham, September 1973.

23. J.P. Barton, "Radiography with Resonance Energy Neutrons", Physics of Medicine and Biology, Vol. 10, 1965, p. 209.

24. A.R. Spowart, "The Advantages of Epicadmium Neutron Beams in Neutron Radiography", Non-destruktive testing, February 1968.

25. H. Berger, "Some Experiments in Fast Neutron Radiography", Materials Evaluation, Vol. 27, 1969, No. 12, p. 368.

26. H. Rapp, E. Rachle, D. Ruffner, "Radiography with Fast Neutrons from a Plasma Focus", Materials Evaluation, Vol. 33, 1975, No. 11, p. 269.

27. C.B. Shaw, J.L. Cason, "Portable Neutron Radiographic Camera Using Californium-252", Materials Evaluation, Vol. 29, 1971, No. 2, p. 40.

28. D.G. Vasilik, R.L. Murri, G.P. Fisher, "Thermal-Neutron Radiography with a Sealed Tube Neutron Generator and Water Moderator", Nuclear Technology, Vol. 14, 1972, p. 279.

29. J.P. Barton, "Developments in the Use of Californium-252 for Neutron Radiography", Nuclear Technology, Vol. 15, 1972, p. 56.

30. Californium-252 Progress, USAEC, Aiken, S.C.

31. H. Berger, "Recent Progress in Neutron Imaging", British Journal of Nondestructive Testing, Vol. 10, 1968, No. 2, p. 26.

32. K. Valentine, S. Kaplan, B. Perez-Menden, L. Kautman, "A Multiwire Proportional Chamber for Imaging Thermal, Epithermal and Fast Neutrons", IEEE Transactions on Nuclear Science, February 1974, p. 178.

33. H. Berger, "Track-Etch Radiography: Alpha, Proton and Neutron", Nuclear Technology, Vol. 19, 1973, p. 188.

34. H. Berger, "Characteristics of a Thermal Neutron Television Imaging System", Materials Evaluation, Vol. 24, 1966, No. 9, p. 475.

35. A.H. Robinson, C.R. Porter, Oregon State University, unpublished.

36. M.L. Mullender, J. Hart, "Transient Neutron Radiography on the VIPER Pulsed Reactor", Radiography with Neutrons, M.R. Hawkesworth, Ed., Conference at the University of Birmingham, September 1973.

37. C.L. Aseltine, R.A. Strich, "Time Resolved Neutron Radiography Using a Fast Pulse Reactor", Nuclear Technology, Vol. 26, 1975, p. 107.

38. A.H. Robinson, J.P. Barton, "High-Speed Motion Neutron Radiography", Transactions American Nuclear Society, Vol. 15, 1972, p. 140.

39. J.P. Barton, R.H. Bossi, A.H. Robinson, "In Motion Neutron Radiography at 10,000 Frames/Second", Spring Conference, American Society for Nondestructive Testing, Los Angeles, 1973.

40. R.S. Stone, H.P. Sleeper, R.H. Stahl, G.B. West, "Transient Behavior of TRIGA, A Zirconium-Hydride, Water Moderated Reactor", Nuclear Science and Engineering, Vol. 6, 1959, p. 255.

41. J. MacPhee, J.R. Wett, "Pulstar-The AMF Pulsing Reactor", Research Reactor Journal, 4,2,12 (Winter 1963-64).

42. G.A. Freund, H.P. Iskinderian, D. Okrent, "TREAT", A pulsed Graphite-Moderated Reactor for Kinetic Experiments", Proceedings of the Second United Nations International Conference on the Peaceful Uses of Atomic Energy, Vol. 10, 1958, p. 461.

43. B.L. Blanks, R.A. Morris, "Experiments with Foil-Film Combinations and Collimators for Neutron Radiography", Materials Evaluation, Vol. 24, 1966, No. 2, p. 76.

44. J.P. Barton, "Divergent Beam Collimator for Neutron Radiography", Materials Evaluation, Vol. 25, 1967, p. 45A.

45. A. Choudry, P.K. Bandopadhyay, "Thermal Neutron Focusing by Tapered Rectangular Collimators ", Nuclear Instruments and Methods, Vol. 92, 1971, p. 339.

46. M.J. Dunn, R.W. Englehart, N.J. Diaz, "Neutron Beam Enhancement in the University of Florida Training Reactor", Transactions American Nuclear Society, Vol. 15, 1972, p. 445.

47. ASTM-E-545-75, American Society for Testing and Materials, Standard.

48. J.A. Rau, W.L. Parker, "Measurement of Antiscatter Grid Effectiveness in Thermal Neutron Radiography of Hydrogenous Material", Nuclear Technology, Vol. 16, 1972, p. 458.

49. Proceedings of the Image Intensifier Sysmposium, National Aeronautics and Space Administration, October 1961, Fort Belvier, Virginia, NASA SP-2.

50. H.V. Soule, Elecro-Optical Photography at Low Illumination Levels, John Wiley and Sons Inc., New York, 1968.

51. American Institute of Physics Handbook, McGraw Hill, New York, 1963.

52. G.A. Jones, High Speed Photography, John Wiley and Sons Inc., New York, 1952.

53. W.G. Hyzer, Engineering and Scientific High-Speed Photography, Macmillan, New York, 1962.

54. "TRIGA Mark II Reactor General Specifications and Description", General Atomic, GA-2627(Rev.), March 1964.

55. J.C. Ringle, T.V. Anderson, A.G. Johnson, Safety Analysis Report for the Oregon State University TRIGA Reactor, August 1968.

56. T.V. Anderson, Oregon State TRIGA Reactor Training Manual.

57. A.W. McReynolds, M.S. Halkin, M.N. Rosenbluth, W.L. Whittemore, "Neutron Thermalization by Chemically-Bound Hydrogen and Carbon", Proceedings of the Second United Nations International Conference on the Peaceful Uses of Atomic Energy, Vol. 16, 1958, p. 1540.

58. M.T. Simnad, F.C. Foushee, G.B. West, "Fuel Elements for Pulsed TRIGA Research Reactors", Nuclear Technology, Vol. 28, 1976, p. 31.

59. D.L. Hetrick, Dynamics of Nuclear Reactors, University of Chicago Press, Chicago, 1971, pp. 164-169.

60. R. Scaletter, "The Fuchs-Nordheim Model with Variable Heat Capacity", Nuclear Science and Engineering, Vol. 16, 1963, p. 459.

61. A.H. Robinson, G.L. Upham, "Applications of Time-Sharing Computers to Reactor Problems and Simulation of TRIGA Reactor Pulses", Simulation, Vol. 11, 1968, No. 4, p. 203.

62. T.B. Pearson, G.B. West, J.B. Dee, A.T. McMain, Jr., "High Pulsing in a TRIGA Annular Core Reactor Design and Development", Transactions American Nuclear Society, Vol. 11, 1968, p. 283.

63. G.B. West, J.R. Shoptaugh, Jr., "Experimental Results from Tests 18 TRIGA FLIP Fuel Elements in the Torrey Pines Mark F Reactor", GA 9350, September 1969.

64. R. Stedman, "Scintillation Counters for Thermal Neutrons Using ^{6}LiF and ZnS(Ag)", CRRP-931, Atomic Energy of Canada Limited, Chalk River Project, May 1960.

65. S.P. Wang, C.G. Shull, W.C. Philips, "Photography of Neutron Diffraction Patterns", Review of Scientific Instruments, Vol. 33, 1962, p. 126.

66. T. Tojo, T. Nakajima, "Preparation of Thermal Neutron Scintillators Based on a Mixture of ZnS(Ag), ^{6}LiF and Polyethylene", Nuclear Instruments and Methods, Vol. 53, 1967, p. 163.

67. A.R. Spowart, "Optimizing Neutron Scintillators for Neutron Radiography", British Journal of Nondestructive Testing, March 1962, p. 2.

68. R.S. Udyavar, N.C. Jain, Y. DeDande, "Slow Neutron Scintillators for Neutron Radiography", Government of India, B.A.R.C. 649, 1972.

69. L. Vu Hong, L. de Nadaillac, G. Jallifier-Talmat, "Scintillateurs Pour Neutrography", C.E.A.-C.E.N.G., AR-G/72-10/LVH/MC. May 1972.

70. R.H. Bossi, A.H. Robinson, "A Monte Carlo Computer Model to Optimize Light Yield from LiF-ZnS Scintillators", Transactions American Nuclear Society, Vol. 22, 1975, p. 153.

71. K.H. Sun, P.R. Malmber, F.A. Pecjak, "High Efficiency Slow Neutron Scintillation Counters", Nucleonics, Vol. 14, 1956, No. 7, p. 46.

72. H.V. Watts, "Research Study on Neutron Interactions in Matter as Related to Image Formation", ARF-1164-21, 1962.

73. H.V. Watts, "Research Study on Neutron Interactions in Matter as Related to Image Formation", ARF-1164-24, 1962.

74. R. Stedman, "Scintillator for Thermal Neutrons Using ^{6}LiF and ZnS(Ag)", Review of Scientific Instruments, Vol. 32, 1960, p. 1156.

75. K.A. Wickersham, R.V. Alvers, R.A. Buchanon, "Rare Earth Oxysulfide X-Ray Phosphors", IEEE Transactions on Nuclear Science, February 1970, p. 57.

76. J.G. Rabatin, General Electric Co., Patent No. U.S. 3,546,128.

77. A.M. Bishay, "Glass Scintillator for Neutron Detection", Journal of the American Ceramics Society, Vol. 44, 1961, No. 5, p. 231.

78. L.M. Bollinger, G.E. Thomas, "Neutron Detection with Glass Scintillators", Nuclear Instruments and Methods, Vol. 17, 1962, p. 97.

79. J.P. Barton, "A Visual Image Quality Indicator (VISQI) for Neutron Radiography", Journal of Materials, Vol. 7, 1972, No. 1, p. 18.

80. W.J. Price, Nuclear Radiation Detection, 2nd Ed., McGraw Hill, 1964, p. 162.

81. P.G. Koontz, G.R. Keepin, J.E. Ashley, "ZnS(Ag) Phosphor Mixtures for Neutron Scintillation Counting", Review of Scientific Instruments, Vol. 26, 1955, No. 4, p. 352.

82. A.R. Spowart, private communication.

83. G.I. Bell, S. Glasstone, Nuclear Reactor Theory, Van Nostrand Reinhold, New York, 1970, pp. 115-119.

84. G. Friedlander, J.W. Kennedy, T.M. Miller, Nuclear and Radiochemistry, 2nd Ed., John Wiley and Sons, 1964, pp. 84-100.

85. F.H. Perrin, "Methods of Appraising Photographic Systems", Journal of the Society of Motion Picture and Television Engineers, Vol. 69, 1960, No. 3, p. 151.

86. F.D. Smith, "Optical Image Evaluation and the Transfer Function", Applied Optics, Vol. 2, 1963, No. 4, p. 335.

87. C.E. Mees, T.H. James, Eds., The Theory of the Photographic Process, The McMillan Co., New York, 1967, pp. 501-521.

88. E. Klingman, "Theory and Application of an Edge Gradient System for Generating Optical Transfer Functions", NASA TN d-6424, July 1971.

89. R.L. Lamberts, C.M. Straub, "Equipment for Routine Evaluation of the Modulation Transfer Function of Photographic Emulsions. I. The Camera", Photographic Science and Engineering, Vol. 9, 1965, p. 331.

90. R.L. Lamberts, C.M. Straub, "Equipment for Routine Evaluation of the Modulation Transfer Function of Photographic Emulsions. II. The Microdensitometer", Photographic Science and Engineering, Vol. 9, 1965, p. 335.

91. R.L. Lamberts, W.F. Garbe, "Equipment for Routine Evaluation of the Modulation Transfer Function of Photographic Emulsions. III. Evaluating and Plotting Instrument", Photographic Science and Engineering, Vol. 9, 1965, p. 340.

92. R.H. Morgan, "The Frequency Response Function", American Journal of Roentgenology and Radium Therapy, Vol. 88, 1962, No. 1, p. 175.

93. R.H. Morgan, L.M. Bates, U.V. Gopalarao, A. Marinaro, "The Frequency Response Characteristics of X-ray Films and Screens", The American Journal of Roentgenology, Radium Therapy and Nuclear Medicine, Vol. 92, 1964, No. 2, p. 426.

94. K. Rossman, G. Lubberts, H.M. Cleare, "Measurement of the Line Spread Function of Radiographic Systems Containing Fluorescent Screens", Journal of the Optical Society of America, Vol. 54, 1964, No. 2, p. 187.

95. K. Rossman, "Measurement of the Modulation Transfer of Radiographic Systems Containing Fluorescent Screens", Physics in Medicine and Biology, Vol. 9, 1964, No. 4, p. 551.

96. C.H. Dyer, E.L. Criscoulo, "Measurement of Spatial Frequency Response of Certain Film Screen Combinations to 10 MeV X Rays", Materials Evaluation, Vol. 24, 1966, No. 11, p. 631.

97. T. Inouye, K. Ogawa, M. Iwanaga, "Image Analysis of Thermal Neutron Radiographs", Oyo Butsuri, Vol. 34, November 1965 (translated by R.A. Scutt, NP TR 1716).

98. M.R. Hawkesworth, M.A. Raoof, Some Measurements of the Resolving Power of the Intensifying Screens Used for Radiography with Beams of Thermal Neutrons", Journal of Physics E, Vol. 3, 1970, p. 851.

99. R.H. Bossi, J.L. Cason, C.N. Jackson, Jr., "The Modulation Transfer Function and Effective Focal Spot as Related to Neutron Radiography", Materials Evaluation, Vol. 30, 1972, No. 5, p. 103.

100. D.M. Alger, S.R. Bull, "Measurement of Modulation Transfer Functions of Radiographic Systems", Transactions American Nuclear Society, Vol. 22, 1975, p. 145.

101. J.W. Coltman, "The Specification of Imaging Properties by Response to a Sine Wave Input", Journal of the Optical Society of America, Vol. 44, 1954, No. 6, p. 468.

102. R. Barakeat, "Determination of the Optical Transfer Function Directly from the Edge Spread Function", Journal of the Optical Society of America, Vol. 55, 1965, p. 1217.

103. R.A. Jones, "An Automated Technique for Deriving MTF's from Edge Traces", Photographic Science and Engineering, Vol. 11, 1967, p. 102.

104. R.A. Jones, J.T. Kelley, "Reliability of Image Evaluation Techniques", Applied Optics, Vol. 8, 1965, p. 941.

105. R.A. Jones, E.C. Yeadon, "Determination of the Spread Function from Noisy Edge Scans", Photographic Science and Engineering, Vol. 13, 1969, p. 200.

106. B. Tatian, "Asymptotic Expansions for Correcting Truncation Error in Transfer Function Calculations", Journal of the Optical Society of America, Vol. 61, 1971, p. 1214.

107. M. Takeda, T. Ose, "Influence of Noise on the Measurement of Optical Transfer Functions by Digital Fourier Transform Methods", Journal of the Optical Society of America, Vol. 65, 1975, p. 502.

108. R.W. Hamming, Numerical Methods for Scientists and Engineers, 2nd Ed., McGraw Hill, New York, 1962, pp. 349-355.

109. B. Carnahan, H.A. Luther, J.O. Wilkes, Applied Numerical Methods, John Wiley, New York, 1969, p. 63.

110. A. Rose, Vision: Human and Electronic, Plenum Press, New York, 1973.

111. R.E. Sturn, R.H. Morgan, "Screen Intensification Systems and Their Limitations", American Journal of Roentgenology and Radium Therapy, Vol. 62, 1949, p. 617.

112. E.T. Larson, H.E. Nitka, "The Meaning of Characteristic Curves", ANL 6515, 1965.

113. K. Rossman, "Image Quality", Physics of Diagnostic Radiology, D.J. Wright, Ed., USDHEW No. (FDA) 74-8006, November 1973, p. 220.

114. A.J. Rose, "Sensitivity Performance of the Human Eye on an Absolute Scale", Journal of the Optical Society of America, Vol. 38, 1948, No. 2, p. 200.

115. M.R. Hawkesworth, "The Exposure Necessary to Discern Detail in Unsharp Neutron Radiographs", Transactions American Nuclear Society, Vol. 17, p. 90.

APPENDICES

APPENDIX A

```
      PROGRAM SCNTLTR
C THIS PROGRAM MODELS A SCINTILLATOR AS SPHERES OF ZNS IN LIF
C INPUTS ARE:  ZNS GRAIN SIZE IN MICRONS
C              ZNS TO LIF WEIGHT RATIO
C              FRACTION OF BINDER CONTENT
C              PACKING DENSITY FRACTION
C              TOTAL THICKNESS OF SCINTILLATOR IN CENTIMETERS
C              NUMBER OF HISTORIES TO BE RUN
      DIMENSION P(2),ENPL(2),PF(2),ENF(2),ENLIF(2),ENZNS(2)
      DIMENSION R(2,1000),S(2,1000),E(2,1000)
      DIMENSION N(20)
C
C......INITIATION OF PROBLEM......
    1 CONTINUE
      RATIO = TTYIN(4H WEI,4HGHT ,4HRATI,4HO = )
      SIZE = TTYIN(4H ZNS,4H GRA,4HIN S,4HIZE=)
      BINDER = TTYIN(4H BIN,4HDER ,4H =  )
      DENS = TTYIN(4H PAC,$HKING,4H DEN,4HSITY,4H =  )
      BFRAC = 1.0-BINDER
      A = SIZE/6.0
      B = (A(RATIO*2.56/4.10) + A)/BFRAC
      T = TTYIN(4H TOT,4HAL T,4HHICK,4HNESS,4H =  )
      IHIST = TTYIN(4H # O,4HF HI,4HSTOR,4HIES=)
      P(1) = 23.46
      P(2) = 4.20
      PF(1) = 4.14
      PF(2) = 0.74
      ENPL(1) = 0.0803
      ENPL(2) = 0.337
      ENF(1) = 0.204
      ENF(2) = 0.859
      DO 20 K=1,2
      DO 20 L=1,IHIST
      R(K,L) = 0.0
      S(K,L) = 0.0
      E(K,L) = 0.0
   20 CONTINUE
C
C......START SOLUTION OF PROBLEM......
      DO 700 I=1,2
C FOR I=1, TRITON CASE AND I=2, ALPHA CASE
C PATH LENGTH IN UNITS OF MICRONS
      TLLIF = 0.0
      TLZNS = 0.0
      TLFINL = 0.0
      TLFINZ = 0.0
      ABSZNS = 0.0
```

```
      ABSLIF = 0.0
      ISEED  = 1949
C START OF HISTORY
      DO 500 J=1,IHIST
      X = (B-A) * RANDOM(ISEED) + A
      PATH = P(I)
   50 U = 2.0 * RANDOM(ISEED) - 1.0
      IF (I-2) 100,80,100
   80 U = -U
C......FIRST PHASE OF BRAGG CURVE......
C PATH IN LIF
  100 CONTINUE
C SEE IF U GTR 0
      IF (U-0.0) 110,50,120
C POSITIVE U ROUTINE FOR LIF
C DISTANCE TO BOUNDARY
  120 DB = (B-X)/U
C COMPARE PATH AND DB
      IF (PATH-DB) 130,130,140
C ROUTINE FOR PATH GTR DB
  140 TLLIF = DB + TLLIF
      U = -U
      PATH = PATH - DB
      X = B
      GO TO 100
C ROUTINE FOR PATH LSS DB
  130 TLLIF = PATH + TLLIF
      X = X + PATH*U
      GO TO 300
C NEGATIVE U ROUTINE FOR LIF
  110 DB = (X-A)/(-U)
C COMPARE PATH AND DB
      IF (PATH-DB) 170,170,180
C ROUTINE FOR PATH GTR DB
  180 TLLIF = DB + TLLIF
      PATH = PATH - DB
      X = A
      GO TO 200
C STATEMENT 200 IS THE BEGINNING OF ZNS ROUTINE
C ROUTINE FOR PATH LSS DB
  170 GO TO 130
C PATH IN ZNS
  200 CONTINUE
C SEE IF U GTR 0
      IF (U-0.0) 210,210,220
  220 DB = (A-X)/U
      IF (PATH-DB) 230,230,240
C ROUTINE FOR PATH GTR DB
  240 TLZNS = DB + TLZNS
      R(I,J) = DB + R(I,J)
      PATH = PATH - DB
```

```
      X = A
      GO TO 100
C ROUTINE FOR PATH LSS DB
  230 TLZNS = PATH + TLZNS
      R(I,J) = PATH + R(I,J)
      X = X + PATH*U
      GO TO 300
C NEGATIVE U ROUTINE FOR ZNS
  210 DB = X/(-U)
C COMPARE PATH AND DB
      IF (PATH-DB) 270,270,280
C ROUTINE FOR PATH GTR DB
  280 TLZNS = TLZNS + DB
      R(I,J) = DB + R(I,J)
      U = -U
      PATH = PATH - DB
      X = 0
      GO TO 200
C ROUTINE FOR PATH LSS DB
  270 GO TO 230
C......SECOND PHASE OF BRAGG CURVE......
C PATH IN LIF
  300 PATH = PF(I)
      IF (X-A) 400,400,305
  305 CONTINUE
      IF (U-0.0) 310,310,320
  320 DB = (B-X)/U
      IF (PATH - DB) 330,330,340
  340 TLFINL = DB + TLFINL
      U = -U
      PATH = PATH - DB
      X = B
      GO TO 305
  330 TLFINL = PATH + TLFINL
      ABSLIF = ABSLIF + 1
      GO TO 500
  310 DB = (X-A)/(-U)
      IF (PATH - DB) 370,370,380
  380 TLFINL = DB + TLFINL
      PATH = PATH - DB
      X = A
      GO TO 400
  370 GO TO 330
C PATH IN ZNS
  400 IF (U-0.0) 410,410,420
  420 DB = (A-X)/U
      IF (PATH - DB) 430,430,440
  440 TLFINZ = DB + TLFINZ
      S(I,J) = DB + S(I,J)
      PATH = PATH - DB
      X = A
```

```
      GO TO 305
  430 TLFINZ = PATH + TLFINZ
      S(I,J) = PATH + S(I,J)
      ABZNS = ABSNZ + 1
      GO TO 500
  410 DB = X/(-U)
      IF (PATH - DB) 470,470,480
  480 TLFINZ = TLFINZ + DB
      S(I,J) = DB + S(I,J)
      U = -U
      PATH = PATH - DB
      X = 0.0
      GO TO 400
  470 GO TO 430
  500 E(I,J) = R(I,J)*ENPL(I) + S(I,J)*ENF(I)
      CONTINUE
C OUTPUT OF PATHS IN LIF AND ZNS
      IF (I-1) 510,510,520
  510 WRITE (61,515)
  515 FORMAT (/,' OUTPUT OF TRITON CASE')
      GO TO 530
  520 WRITE (61,525)
  525 FORMAT (/,' OUTPUT OF ALPHA CASE')
  530 ENLIF(I) = ENPL(I)*TLLIF + ENF(I)*TLFINL
      ENZNS(I) = ENPL(I)*TLZNS + ENF(I)*TLFINZ
      WRITE (61,540) ENLIF(I)
  540 FORMAT (/,' ENERGY IN LIF = ',F7.2,' MEV')
      WRITE (61,545) ENZNS(I)
  545 FORMAT (' ENERGY IN ZNS = ',F7.2,' MEV')
      WRITE (61,550) ABSLIF
  550 FORMAT (' # ABSORP. LIF = ',F6.0)
      WRITE (61,555) ABSZNS
  555 FORMAT (' # ABSORP. ZNS = ',F6.0)
  700 CONTINUE
C
C......RESULTS......
C TOTAL ENERGY DEPOSITED BY BOTH TRITON AND ALPHA
      TOTENLIF = ENLIF(1) + ENLIF(2)
      TOTENZNS = ENZNS(1) + ENZNS(2)
      WRITE (61,710) TOTENLIF
  710 FORMAT (/,' TOTAL ENERGY IN LIF = ',F8.2,' MEV')
      WRITE (61,720) TOTENZNS
  720 FORMAT (' TOTAL ENERGY IN ZNS = ',F8.2,' MEV')
      EFF = 1.0-EXP(-50.25*T*DENS*(B*BFRAC-A)/B)
      WRITE (61,730)EFF
  730 FORMAT (/,' SCINTILLATOR EFFICIENCY = ',F7.4)
      RESULT = EFF * TOTENZNS/IHIST
      WRITE (61,740) RESULT
  740 FORMAT(' ENERGY IN ZNS PER NEUTRON = ',F7.4,' MEV',/)
      WRITE (61,750)
  750 FORMAT (' DISTRIBUTION OF ENERGY IN ZNS PER NEUTRON')
```

```
      WRITE (61,760)
  760 FORMAT ('  ENERGY RANGE  -  NO. HISTORIES'/)
      DO 780 I=1,10
  780 N(I) = 0
      DO 820 J=1,IHIST
      PERCEN = ((E(1,J)+E(2,J))/4.78)*100.
      M = PERCEN/10.0 + 0.5
      N(M) = N(M) + 1
  820 CONTINUE
      DO 840 K=1,10
      KK = K*10
      KKK = KK-10
      WRITE (61,850) KKK,KK,N(K)
  840 CONTINUE
  850 FORMAT (3X,I4,' -',I3,'%',4X,I7)
      WRITE (61,880)
  880 FORMAT (1H1,'                    NEW CASE',/)
      GO TO 1
      END
```

APPENDIX B

```
      PROGRAM LIGHT
C THIS PROGRAM DETERMINES THE DISTRIBUTION OF LIGHT FROM A
C SCINTILLATOR AS A MEASURE OF RESOLUTION CAPABILITY.
      DIMENSION Q(20), QN(20)
    1 CONTINUE
C
C......INITIALIZE......
      T = TTYIN (4H THI,4HCKNE,4HSS= )
      W = TTYIN (4H WEI,4HGHT ,4HRATI,4HO = )
      B = TTYIN (4H BIN,4HDER=)
      D = TTYIN (4H PAC,4HKING,4H DEN,4HSITY,4H = )
      C = TTYIN (4H LIG,4HHT C,4HOEF.,4H =  )
      BFRAC = 1.0-B
      SIGMA = 50.25*D*BFRAC/(1.+W*2.56/4.1)
        DO 50 I=1,20
   50   Q(I) = 0
      N = 0
      M = 0
      L = 0
      ISEED = 1949
C
C......START HISTORIES......
  100 N = N+1
      IF (N.GT.10000) GO TO 200
      X = -ALOG(RANDOM(ISEED))/SIGMA
      IF (X.GE.T) GO TO 150
      L = L+1
      P = T-X
        DO 120 J=1,20
        Y = J*0.001-0.001
        R = SQRT(P*P+Y*Y)
        Q(J) = EXP(-C*R)+Q(J)
  120   CONTINUE
      IF (L.EQ.500) GO TO 200
      GO TO 100
  150 M = M+1
      GO TO 100
C
C......RESULTS......
  200 WRITE(61,500)
      WRITE(61,502) M
      WRITE(61,504) L
      VALUE = M+L
      EFF = L/VALUE
      WRITE(61,506) EFF
      WRITE(61,508)
      WRITE(61,510)
```

```
      WRITE(61,512)
      TEST = 0
        DO 240 J=1,20
  240   IF(Q(J).GT.TEST) TEST = Q(J)
        DO 260 J=1,20
  260   QN(J) = Q(J)/TEST
        DO 280 J=1,20
        Y = J*10.-10.
        WRITE(61,514) Y,Q(J),QN(J)
  280   CONTINUE
      WRITE(61,516)
      GO TO 1
C
C......FORMAT STATEMENTS......
  500 FORMAT(/' ***RESULTS***')
  502 FORMAT(//,' # OF TRANSMITTED NEUTRON =',I6)
  504 FORMAT(' # OF ABSORBED NEUTRONS =',I6)
  506 FORMAT(' SCREEN EFFICIENCY = ',F5.3)
  508 FORMAT(/,' DISTRIBUTION OF LIGHT AT SCINTILLATOR SURFACE')
  510 FORMAT('      Y          RELATIVE')
  512 FORMAT('   (MICRONS)    LIGHT YIELD    NORMALIZED'/)
  514 FORMAT(2X,F5.1,4X,F12.6,3X,F7.4)
  514 FORMAT(///,' NEW CASE'/)
      END
```

APPENDIX C

```
      PROGRAM TRANS
C THIS PROGRAM CALCULATES THE FOURIER TRANSFORM OF THE
C DERIVATIVE OF A DATA SET.  CUBIC SPLINES INTERPOLATION
C IS USED ON THE DATA POINTS.  IN PARTICULAR THE INPUT
C DATA APPEAR AS THE EDGE SPREAD FUNCTION.  THE SECOND
C DERIVATIVE OF THE DATA IS OBTAINED FROM A TRI-
C DIAGONAL MATRIX SOLUTION.  THOSE VALUES ARE USED
C IN THE FOURIER TRANSFORM OF A CUBIC SPLINE
C INTERPOLATING POLYNOMIAL FOR THE FIRST DERIVATIVE
C OF THE DATA.
C
C......INPUT......
      DIMENSION U(500),ZL(500),D(500),B(500),YPP(500),Y(500),
     1 YP(500)
      READ(1,902) N,H
      NM = N-1
      NMM = N-2
      PI = 355./113.
      READ (1,904) (Y(I),I=1,N)
      YPP(1) = 0
      YPP(N) = 0
      WRITE(5,900)
      WRITE(5,902) N,H
      WRITE (5,904) (Y(I),I=1,N)
C
C......SET UP TRI-DIAGONAL MATRIX......
      DO 30 I=2,NM
      D(I) = 4.
      U(I) = 1.
      ZL(I) = 1.
      B(I) = 6.*(Y(I+1)-2.*Y(I)+Y(I-1))/(H*H)
   30 CONTINUE
C......SOLVE MATRIX......
      DO 50 K=2,NM
      U(K) = U(K)/D(K)
      B(K) = B(K)/D(K)
      IF (K.EQ.N) GO TO 50
      D(K+1) = D(K+1)-U(K)*ZL(K+1)
      B(K+1) = B(K+1)-B(K)*ZL(K+1)
   50 CONTINUE
C......RUN BACK SOLUTION......
      YPP(NM) = B(NM)
      DO 60 I=2,NMM
      J = NM+1-I
      YPP(J) = B(J)-U(J)*YPP(J+1)
   60 CONTINUE
C CALCULATION OF FIRST DERIVATIVE VALUES
```

```
      WRITE(5,906)
      DO 70 I=1,NM
   70 YP(I)=(Y(I+1)-Y(I))/H-H*(2.*YPP(I)+YPP(I+1))/6.
      YP(N) = (Y(N)-Y(NM))/H+H*(YPP(NM)+2.*YPP(N))/6.
      WRITE(5,905) (YP(I),I=1,N)
      WRITE(5,910)
C
C.....PROGRAM FOR FOURIER TRANSFORM OF DERIVATIVE POLY.....
      FREQ = 0.1
   80 W = 2.*PI*FREQ
      RP = 0
      RN = 0
      XIP = 0
      XIN = 0
      DO 110 I=1,NM
      J = I+1
      K = I-1
      V1 = (H/(6.*W)+1./(H*W**3))
      V2=(YPP(J)*H/(2.*W)+(Y(J)-Y(I))/(H*W)+(YPP(I)-YPP(J))*V1)
      V3=(YPP(I)*H/(2.*W)+(Y(I)-Y(J))/(H*W)+(YPP(J)-YPP(I))*V1)
      A1 = (YPP(J)*COS(W*I*H)-YPP(I)*COS(W*K*H))/(W*W)
      A2 = V2*SIN(W*I*H)+V3*SIN(W*K*H)
      A3 = A1+A2
      IF (A3) 120,125,125
  120 RN = RN+A3
      GO TO 130
  125 RP = RP+A3
  130 A4 = (YPP(J)*SIN(W*I*H)-YPP(I)*SIN(W*K*H))/(W*W)
      A5 = -V2*COS(W*I*H)-V3*COS(W*K*H)
      A6 = A4+A5
      IF (A6)  140,145,145
  140 XIN = XIN+A6
      GO TO 110
  145 XIP = XIP+A6
  110 CONTINUE
C
C.....OUTPUT OF RESULT.....
      REAL = RN+RP
      XIMAG = XIN+XIP
      Q = SQRT(REAL**2+XIMAG**2)
      WRITE(5,912) FREQ,REAL,XIMAG,Q
      IF(Q.LT.0.008) GO TO 200
      FREQ = FREQ + 0.05
      IF(FREQ.GE.0.35) FREQ = FREQ+0.05
      IF(FREQ.GE.0.7) FREQ = FREQ+0.1
      IF(FREQ.GE.1.2) FREQ = FREQ+0.3
      IF(FREQ.GT.3.1) FREQ = FREQ+0.5
      IF(FREQ.GE.7.0) FREQ = FREQ+1.0
      IF(FREQ.GE.12.0) FREQ = FREQ+3.0
      IF(FREQ.GT.31.0) FREQ = FREQ+5.0
      IF(FREQ.GT.51.0) GO TO 200
```

```
      GO TO 80
C
C......FORMAT STATEMENTS......
  900 FORMAT (//'   INITIAL DENSITY DATA'/)
  902 FORMAT (I3,F7.4)
  904 FORMAT (5F7.4)
  905 FORMAT (5F10.4)
  906 FORMAT (/'  DERIVATIVE OF DENSITIES'/)
  910 FORMAT(/6X'FREQ'7X'REAL'6X'IMAGINARY'3X'MAGNITUDE'/)
  912 FORMAT(1X,F10.5,3(F12.6))
  200 END
```

APPENDIX D

ELECTRONICS FOR FIRING SYNCHRONIZATION

The need for event synchronization with the reactor pulse and high speed camera system has been discussed in the text. The timing system to achieve the synchronization consists of a DPDT microrelay, two Nuclear Data Clock/Time Bases, a differential comparator box, and a trigger box. Figure 7-6 displays these instruments.

Figure D-1 is a layout of the microrelay box. The camera closes the relay when the proper frame rate is reached. This initiates a signal to the first Clock/Time Base to begin counting and also signals the reactor pulse mechanism.

Figure D-2 shows the circuit diagram for the differential comparator box. This box recieves a signal from the second Clock/Time Base and relays it to the silicon control rectifier (SCR) in the trigger box. The differential comparator circuity assures that a proper current is supplied to the SCR when the voltage change from the timer is sensed.

The trigger mechanism is shown in figure D-3. The trigger box contains an SCR and dead man's switch which complete the total circuit consisting of the SCR, dead man's switch, 12 volt battery and gas ignitor (mechanism in rifle barrel for remote munition firing). The SCR upon a signal from the differential comparator closes this circuit. If during this period the dead man's switch is also held closed, the event firing proceeds.

Figure D-1

MICRORELAY BOX

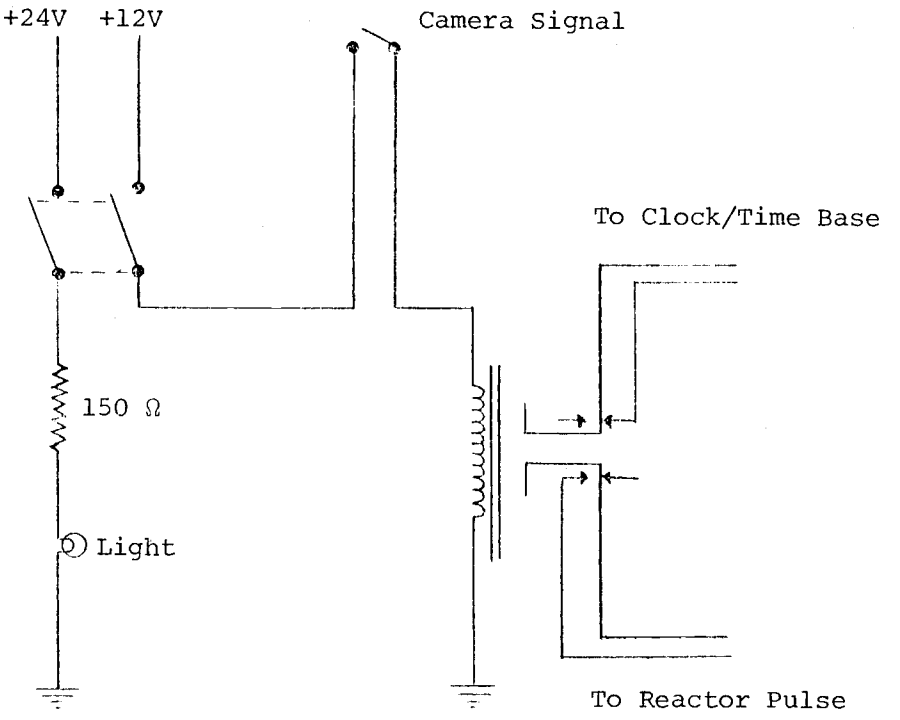

Figure D-2

DIFFERENTIAL COMPARATOR BOX

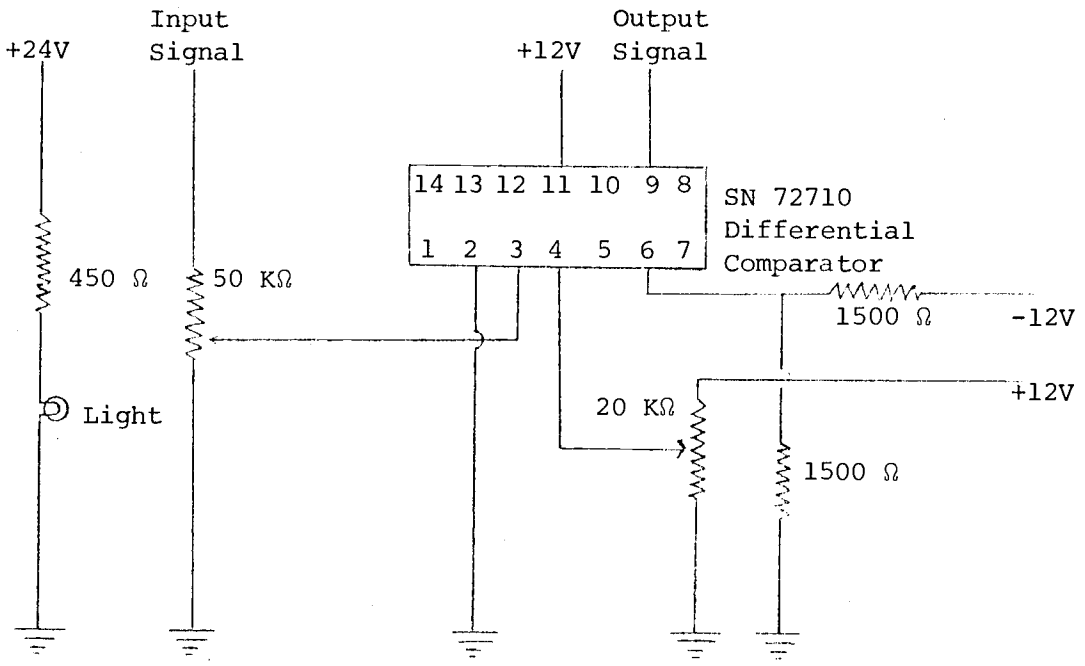

Figure D-3

TRIGGER MECHANISM